

Fabrication of Long Range Surface Plasmon Polariton
Biosensors Incorporating a Channel Etch Stop Layer and
Wafer Bonded Cover

by

Pengshuai Ren

A thesis submitted to the Faculty of Graduate and Postdoctoral
Affairs in partial fulfillment of the requirements for the degree of

Master of Applied Science

in

Electrical and Computer Engineering

Carleton University
Ottawa, Ontario

© copyright, 2017, Pengshuai Ren, Carleton University

Abstract

This thesis presents the micro-fabrication process of a Long Range Surface Plasmon Polariton (LRSPP) biosensor device. The fabrication process was modified in two aspects which include adding a channel etch stop layer to improve the accuracy and uniformity of channels in the device and replacing the photoresist etching mask by an Al etching mask to avoid the thermal cracking. The optical performance of the fabricated chips shows that the biosensor has a 5.03dB/mm attenuation loss and has a 0.10dB response for a monolayer of BSA on Au waveguides. CYTOP bonding process was introduced in the fabrication of the device that incorporates a glass cover. A glass wafer was successfully bonded to a silicon wafer by CYTOP bonding process to seal the channels, which ensured an isolated testing environment for the biochemical fluid.

Acknowledgements

Foremost I would like to thank my mother, Xia Zhou, and my father Luyong Ren, for their constant encouragement and financial support that has driven me to complete this research. I would also like to thank my supervisors Dr. R. Niall Tait and Dr. Pierre Berini for giving me the opportunity to work in the field of micro-fabrication and for directing me through my entire research by providing their extensive knowledge and expertise. I would like to acknowledge the Carleton University Microfabrication staff of Rob Vandusen, Angela McCormick, and Rick Adams. In addition, I thank the staff from the Microfabrication lab at University of Ottawa, Ewa Lisicka-Skrzek and Anthony Olivieri, for their continuous patience and assistance on the techniques of micro-fabrication and equipment operation. Finally, I would also like to acknowledge Howard Northfield, Muhammad Asif and Oleksiy Krupin for their countless help and consultation that motivated me to conquer each obstacle during this research period.

Table of Contents

Abstract.....	ii
Acknowledgements	iii
Table of Contents.....	iv
List of Tables	vi
List of Figures	vii
1 Chapter: Introduction	1
1.1 Motivation and Contribution	1
1.2 Thesis Overview	2
2 Chapter: Background and Literature Review.....	4
2.1 Optical Biosensors	4
2.2 Surface Plasmon Resonance Biosensors	11
2.3 Long Range Surface Plasmon Polaritons Biosensor	16
2.3.1 Long range surface plasmon polaritons.....	16
2.3.2 LRSPP biosensor	21
3 Chapter: Fabrication of Surface Plasmon Biosensor in CYTOP	28
3.1 Wafer Selection and Preparation.....	28
3.2 Lower CYTOP Cladding	30
3.3 Au Waveguide Patterning.....	36
3.3.1 Bi-layer Lithography.....	36
3.3.2 Au Waveguide Metallization.....	40
3.3.3 Issues and Discussions on the Process	46
3.4 Etch Stop Layer Patterning.....	49
3.4.1 Purpose of Introducing Etch Stop Layer	49

3.4.2	Process of Etch Stop Layer Patterning	51
3.4.3	Issues and Solutions in the Process	55
3.5	Top CYTOP Cladding	60
3.5.1	Top Cladding Process	60
3.5.2	Issues in the Previous Work	63
3.5.3	CYTOP Stress Measurement	64
3.6	Fluidic Channel Patterning	68
3.6.1	Issues in the Previous Work	68
3.6.2	Purpose of Al Etching Mask Lithography	69
3.6.3	Process of Al Etching Mask Lithography	69
3.6.4	Channel Etching Process and Results Evaluation	73
3.7	Optical measurements and discussion	82
4	Chapter: Glass Lid Seal by CYTOP Bonding	89
4.1	Bonding trial 1	89
4.2	Bonding trial 2	95
4.3	Bonding trial 3	97
4.4	Bonding trial 4	100
5	Chapter: Conclusions and Future Work	104
References		106

List of Tables

Table I	Lower CYTOP Cladding Fabrication Process	31
Table II	Au Waveguides Bi-layer Lithography Fabrication Process	38
Table III	Au Waveguides Metallization Fabrication Process	42
Table IV	Etch Stop Layer Fabrication Process	54
Table V	Upper CYTOP Cladding Fabrication Process	61
Table VI	CYTOP Stress Measurement Results	64
Table VII	Al Etching Mask Lithography Process	71
Table VIII	Channel Etching Depth Measurement.....	73
Table IX	The Process Qualification Comparison.....	81
Table X	The Bonding Process of the First Trial	91
Table XI	The Bonding Process of the Second Trial.....	96
Table XII	The Bonding Process of the Third Trail	98
Table XIII	The Bonding Process of the Forth Trial	101

List of Figures

Figure 2.1	Conceptual illustration of a biosensor.....	5
Figure 2.2	Evanescence field sensing by an adsorbed layer on a waveguide [16].....	8
Figure 2.3	Comparison of different waveguide structures [15].	10
Figure 2.4	Distribution of the magnetic field intensity for a SPP [25].....	13
Figure 2.5	Excitation of surface plasmon polaritons [27].....	14
Figure 2.6	A waveguide integrated SPR biosensor [28].....	15
Figure 2.7	Metal slab bounded by semi-infinite dielectrics [33]	17
Figure 2.8	The dispersion characteristics with thickness of the first eight modes [35].	19
Figure 2.9	The waveguide architectures used for coupling LRSPPs [37].	20
Figure 2.10	The theoretical and experimental attenuation of all Au waveguides in different width and separated space [37].	21
Figure 2.11	Adhesion mechanism for three types of CYTOP [copyright by AGC., Ltd]	23
Figure 2.12	Cross-sectional profile of device structure.....	25
Figure 2.13	Process flow for fabricating the LRSPP device.....	27
Figure 3.1	Thickness measurement of lower CYTOP cladding.....	34
Figure 3.2	AFM surface scanning results of lower CYTOP cladding.....	35
Figure 3.3	Microscope images of Bi-layer lithography	39
Figure 3.4	AFM measurement of roughness and thickness.	43
Figure 3.5	Microscope images of Au waveguide after lift-off process.	45
Figure 3.6	Undesirable lithography results	48
Figure 3.7	Illustrations of channel etching by O ₂ plasma	50

Figure 3.8	The profile of the etched channel after removal of etch stop layer	50
Figure 3.9	Microscope images captured after etch stop layer process	53
Figure 3.10	Profilometer measurement of an Au waveguide and an Au pad	57
Figure 3.11	Microscope image of SiO ₂ being twisted at sudden thermal change.....	57
Figure 3.12	Results obtained by modified baking step.....	58
Figure 3.13	Microscope image of shattered SiO ₂ pattern.....	59
Figure 3.14	Microscope image of Al etch stop layer after heating above 100°C	59
Figure 3.15	Microscope images captured after upper CYTOP cladding process	62
Figure 3.16	Microscope image of CYTOP combination surface.....	67
Figure 3.17	Microscope image of Al mask deformation	72
Figure 3.18	Microscope image after Al mask developing	72
Figure 3.19	Microscope images after channel etching and etch stop layer removal.....	75
Figure 3.20	The AFM scanning results of one Au waveguide.	78
Figure 3.21	The thickness measurement of one Au waveguide by AFM.....	78
Figure 3.22	The AFM scanning results of CYTOP in a channel	79
Figure 3.23	The depth of a channel measured from the right edge by profilometer Dektak.....	79
Figure 3.24	The SEM image of the cleaved channel.....	80
Figure 3.25	The Microscope image of the chip facet showing a waveguide cross-section	80
Figure 3.26	Assembled testing fluidic settlement	83
Figure 3.27	Biosensing test system setup	83
Figure 3.28	Mode image of the LRSPPs excited from the device.	84

Figure 3.29 Cutback curve obtained from the device	85
Figure 3.30 BSA detection results obtained from the device	87
Figure 3.31 Bulk sensing test results from the device	88
Figure 4.1 Microscope images of top view of bonded wafer.....	93
Figure 4.2 Microscope image of IPA flowing inside the channel without leakage	94
Figure 4.3 SEM image of the cross section of a channel opening	94
Figure 4.4 Microscope image of IPA flowing inside the channel without leakage	96
Figure 4.5 Microscope images of top view of the third bonded wafer.....	99
Figure 4.6 Misalignment indication by microscope of the third wafer pair	99
Figure 4.7 Microscope images of top view of the forth wafer pair	103
Figure 4.8 Microscope image of IPA flowing inside the channel without leakage	103

1 Chapter: Introduction

1.1 Motivation and Contribution

With the advent of the optical biosensor, fields involved in monitoring chemical molecule or biomolecule interaction, such as drug testing, have been revolutionized as a fast and accurate bio-measurement can now be realized. Current optical biosensors are dominated by surface plasmon resonance (SPR) technology due to its real-time, label-free analytical observation of biomolecule interaction in a small volume of reagent or recognition biochemical [1]. Some commercial SPR devices have been successfully applied in the pharmaceutical field where the chemical interaction kinetics are a priority. Those devices commonly utilize the Kretschmann-Raether configuration, where a prism with a deposited Au film is interrogated with a transverse magnetic polarized beam to excite SPR mode [1]. However the bulky and high-cost implementations and optical limitations of transmission losses hinder their popularity in other markets, such as medical diagnosis. Alternative optical approaches involving waveguides that consist of metal and dielectrics have been exploited in order to alleviate these drawbacks [2]. Long range surface plasmon polaritons (LRSPP) is one method that succeeds in extending propagation length to millimeters in the infrared, further than that of a conventional SPR, which is less than $100\mu\text{m}$. This creates a larger sensing area, and thus increases the sensitivity of the device based on LRSPPs [3]. In the work of Nenninger [4], the magnitude of sensitivity can be achieved on the order of $1 \times 10^5 \text{ nm RIU}^{-1}$ (Refractive Units Index) in the case of the Teflon-based LRSPP sensor. This compares with a sensitivity of $1.4 \times 10^4 \text{ nm RIU}^{-1}$ for a conventional prism-coupled SPR sensor operating at 850nm. Finally, LRSPP biosensors can be fabricated with micron

sized features, which renders them compact and portable.

This thesis presents a detailed fabrication process for a LRSPP biosensor that is based on Au waveguides embedded in CYTOP (trademark by AGC., Ltd) with incorporated microfluidic channels. The key factors in developing the process successfully are: thermal compatibility between polymer (CYTOP A-grade) and metal such as Au and Al, and residual film stress control of CYTOP, particularly when combining layers of different types of CYTOP. The contribution of the thesis is to modify the process in certain steps to make it more robust and to enhance yield. Two process techniques which were not previously used in this research are introduced. One is adding an etch stop layer in the process to ensure the accurate and uniform thickness of fluidic channels across the wafer. The other is replacing thick photoresist SPR-220 (trademark by DOW) with Al as the fluidic channel etch mask in order to avoid CYTOP cracking which is believed to result from the soft bake step in patterning SPR-220. The goal of this research is to realize the complete fabrication process for the LRSPP biosensor with an attenuation loss less than 7dB/mm. My contribution to this thesis is the micro-fabrication of the LRSPP biosensor designed by the Berini group from University of Ottawa. The biosensing test on the final chips was performed by Alex Krupin from University of Ottawa.

1.2 Thesis Overview

This thesis is comprised of 5 chapters. Chapter 1 describes the motivation and contribution of this research work. In Chapter 2, a background review of the field in optical biosensors, SPR and LRSPPs, and biosensors based on these phenomena will be presented. Some

previous work is also illustrated to give a better understanding of theoretical basis and realistic meaning of the current work. The fundamental parts of the thesis are included in Chapter 3 and Chapter 4. Chapter 3 and Chapter 4 describe the fabrication process of the LRSPP biosensor with the process steps required to fabricate a complete device introduced in Chapter 3 and the CYTOP bonding work shown in Chapter 4. The thesis contribution to process innovation will be particularly highlighted in these chapters, and some issues and corresponding solutions will be presented and discussed. At the end of these chapters, fabrication results and optical performance of the single chips will be illustrated and discussed. Chapter 5 will summarize the development of this work and discuss the current issues and direction for improvement in future work.

2 Chapter: Background and Literature Review

2.1 Optical Biosensors

A biosensor is an independently integrated device, incorporating a biological recognition receptor, such as enzyme, antibody, microorganism or an artificially imprinted molecule, combined with a signal transducing component. The principle of bio-detection is the specific binding of an analyte of interest to the biological recognition receptor immobilized on the transducer. The transducer translates biochemical properties resulting from the specific interaction between the analyte and bio-recognition element into a measurable and analytical signal, especially an electronic one [2] [5] [6] as shown in Figure 2.1. Biosensors have imposed a significant impact on monitoring applications in widespread fields such as: biomedical diagnosis by personnel at home or hospital, pathogen and toxin detection in food and water, and hazardous gas or ion detection in industrial processes [2] [5]. The ideal biosensor, especially one used in the biomedical diagnosis area, must aim not only to provide reliable and rapid response to low concentration of analytes, but also have the capability of distinguishing targets among species [5] [7]. The demand for fast and portable biosensors with high sensitivity and selectivity for detecting low concentration of chemical and biochemical material has been increasing. Thanks to recent advances in micro and nano technology, polymer technology, optics technology, electronics technology and computer science, it is possible to construct a compact and functional device for biosensing with high speed and reliability at a reasonable cost [8].

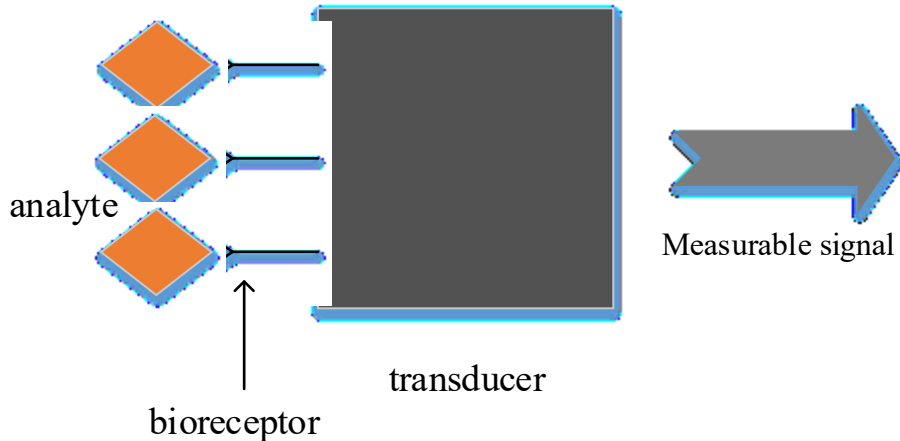


Figure 2.1 Conceptual illustration of a biosensor

Biosensors can be classified into several categories according to the method of signal transduction, such as optical, electrical, electrochemical, piezoelectric, and thermal biosensors [5]. Among these types of biosensors, optical biosensors are attracting great interest due to their fast response, high sensitivity and the ability to perform detections in real time. In addition, optical biosensors provide advantages such as signal immunity to electromagnetic interference and increased spectral information obtained in detection. In recent years, the cost reduction of high-quality fibers and the utilization of photonic integration on a single optical circuit make it possible to mass produce optical biosensors with reliable functionality and high sensitivity at a lower cost [5] [9]. Optical biosensors are biosensors whose transduction process is based on the conversion between a biochemical interaction and an optical signal. Their operation may include direct detection of the bio-samples of interest or indirect detection by the assistance of optically labelled probes. The optical transducer is commonly based on the detection of changes in fluorescence or refractive index (RI). Various methods used for achieving this operation are based on fluorescence spectroscopy, interferometry, spectroscopy of guided modes in optical waveguides and SPR technology [6].

Fluorescence spectroscopy is a widely used optical method for biosensing, especially in the biomedical diagnostics of individual compounds, *in vitro* analyses (cellular and tissue systems) and *in vivo* analyses (animal and human studies) due to its real-time detection and sample preparation requiring minimal physical damage. [10]. Fluorescence-based detection involves the optical detection and spectral analysis of electromagnetic radiation emission related to an energetic transition of a specific substance from an excited state to a lower energy state [10] [11]. There are three types of fluorescence biosensing techniques. The first one is direct detection of a specific molecule before and after a fluorescence related action takes place. The second form is indirect biosensing by applying a fluorophore to the analyte of interest. The fluorophore is a fluorescent compound, commonly called fluorescent dye, which can emit light upon excitation by a specific wavelength. Fluorescence intensity affected by the presence of a specific target molecule can be measured and thus analyzed in the biosensing application. Green fluorescent protein (GFP) is one kind of fluorescent dye capable of indicating the location, structure and dynamics of molecular events with living cells [6]. Other fluorescent dyes such as Rhodamine 6G (Rh6G) and trisodium 8-methoxypyrene-1, 3, 6-trisulfonate (PTS1) are commonly used in biotechnology applications [12]. The drawbacks of this fluorophore-involved method is that binding interactions between an activated fluorescent dye and its target are difficult to detect due to the challenge of distinguishing this localized interaction over background fluorescence. The third type is called fluorescence energy transfer (FRET) [6] [13]. This needs two paired fluorophores to reside within about few Angstroms from each other. In doing so, the light emission wavelength of one overlaps with the excitation wavelength of the other. Thus the excitation of one fluorophore will stimulate fluorescence of the paired

one, generating a unique signal that can be visualize and quantify the position and concentration of interacting fluorescent dyes.

While fluorescence-based detection is highly sensitive and able to detect a single molecule [14], a shortcoming is the laborious labelling processes that may cause cross-sensitivity to a non-target biomolecule. RI detection is a label-free detection mechanism that measures RI change induced by molecular interactions and its detection signal does not scale down with the solution volume, since RI change is related to the sample concentration, not sample mass [15]. In most cases of RI-based biosensors, the characteristics of the sensing light propagation can be influenced and optically monitored when target analytes from the biochemical solution bind to a biorecognition molecule immobilized on the sensor surface due to the change in RI near the binding interface. The sensing light is concentrated near the sensor surface with an evanescent field with exponential decay length of a few tens to hundreds of nanometers [15]. This characteristic leads to two important features. The first feature is that the device can be minimized into micro even nano size since the RI change is only detectable within the range of decay length, which makes ultra-small volume detection feasible. The second feature is that it provides a means of distinguishing actual target molecules from those that do not bind to the sensing surface. However, for a RI-based optical biosensor, temperature fluctuations are an important issue that can generate signal noise during sensing. This is a thermo-optic effect [15] and can be reduced by employing a reference channel built into the same sensor to cancel common-mode temperature related noise.

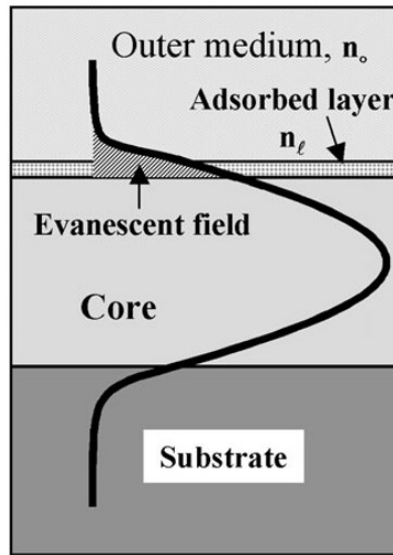


Figure 2.2 Evanescent field sensing by an adsorbed layer on a waveguide [16], copyright permitted by IOP Publishing, LTD.

In recent years RI-based optical biosensors have been developing at a fascinating and fast pace. Various optical structures have been investigated such as photonic crystal based biosensors, optical fiber based biosensors and optical waveguide based biosensors. A photonic crystal (PC) biosensor is based on the defect mode of a PC, a periodic dielectric structure with a periodicity on the order of a wavelength. If a photonic defect structure is introduced into a PC, its transmission spectrum becomes highly sensitive to a change in the environment around the defect. Therefore it can be used as a sensing device when RI changes as a result of the binding of an analyte to the defect. An optical fiber based biosensor uses optical fibers as the transduction medium to detect target biomolecules. Fibers are an inexpensive material and provide efficient signal transmission with minimum loss. If a Bragg grating is written in the fiber core, the fiber can function as a band rejection

filter which reflects a narrow band of light at the specific wavelength [15]. RI changes can be sensed by monitoring the change of wavelength because of the following relationship [17]:

$$\lambda = 2n\Lambda \quad (1)$$

where λ is the reflected wavelength, n is the effective RI of fiber, and Λ is the period of the grating. An optical waveguide is a physical structure that confines and guides light in the optical spectrum. Optical waveguides are commonly used in the optical devices as light transmission and manipulation components. The transduction mechanism for an optical waveguide as a biosensor is utilization of evanescent field sensing (EFS). EFS is sensing the portion of waveguide-confined light that extends into the medium surrounding the waveguide at approximately a hundred nanometers as shown in Figure 2.2. The optical properties of its evanescent field can be altered when a biomolecule interacts with a receptor molecule, leading to a RI change at the waveguide surface [16]. Many kinds of waveguide measurement configurations are applied in the biosensing field such as surface plasmon resonance (SPR), resonant mirror (RM), metal clad waveguide (MCWG), reverse symmetry waveguide and symmetrical metal cladding waveguide as shown in Figure 2.3. RM supports both transverse electric (TE) modes and transverse magnetic (TM) modes and is sensitive to the RI change near the waveguide. MCWG involves a metal layer working as a spacer to separate the low RI waveguide and the high RI substrate, and to guide more light into the solution layer to enhance the light interaction and sensitivity [15]. Reverse symmetry waveguide and symmetrical metal cladding waveguide configurations are similar to MCWG and in all cases increasing light interaction with the functionalized surface is desired in order to achieve higher sensitivity [18] [19]. The biosensor fabricated

in this work is based on SPR and will be elaborated on in the following two subsections.

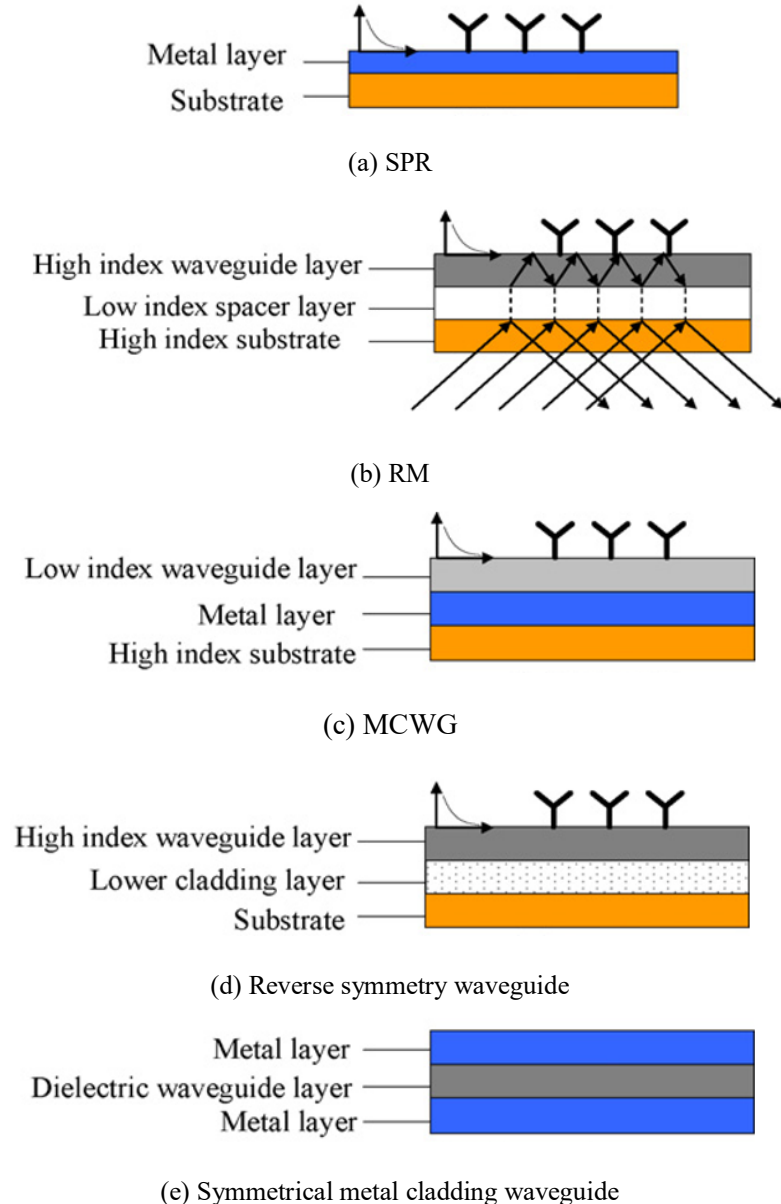


Figure 2.3 Comparison of different waveguide structures [15].

(a) structure of surface plasmon resonance (SPR); (b) structure of resonant mirror (RM); (c) structure of metal clad waveguide (MCWG); (d) structure of reverse symmetry waveguide; (e) structure of symmetrical metal cladding waveguide.

2.2 Surface Plasmon Resonance Biosensors

The phenomenon of anomalous diffraction on diffraction gratings due to the excitation of surface plasmons was first observed by Wood in the early 1900s [20]. In the late 1960s, optical excitation of surface plasmons by the way of attenuated total reflection (ATR) was demonstrated by Kretschmann [21] and Otto [22]. Since then, surface plasmons have gained much interest worldwide and their unique properties have been extensively studied. A surface plasmon polariton (SPP) is an electromagnetic wave, TM wave specifically, excited on the surface of a metal as a result of a resonant interaction between the electromagnetic field of the light and the free electron oscillation on the metal surface [23]. A SPP is characterized by its dispersion and spatial profile. The dispersion relation of a SPP is given by [24]:

$$k_{SPP} = k_0 \sqrt{\frac{\varepsilon_1 \varepsilon_2}{\varepsilon_1 + \varepsilon_2}} \quad (2)$$

where k_{SPP} is the frequency-dependent SPP wave-vector, k_0 is the free-space wave-vector, ε_1 and ε_2 are frequency-dependent permittivity of the metal and the dielectric material respectively. The equation shows a SPP is possible if ε_1 and ε_2 have opposite signs, which is satisfied by the condition of metals and dielectrics [23]. It propagates along the interface between a dielectric and a metal with an evanescent electromagnetic field, confined at the metal-dielectric boundary as shown in Figure 2.4, and will gradually attenuate due to absorption in the metal [23].

A SPR biosensor is an optical biosensor utilizing surface plasmon polaritons (SPPs), a type of unique electromagnetic waves, to monitor interaction between an analyte of interest in solution and a biorecognition element immobilized on the sensing surface [25]. The use of SPR biosensors is increasingly prevalent in the field of biological technology, medical diagnosis, drug testing and environmental and industrial monitoring, as it allows for real-time and quantitative detections without requiring labeling procedures. It generally comprises an optical system containing optical source and propagation structure where SPPs are excited and detected, a bio-functionalized transducing platform which interrelates an identification of the specific analyte into changes in the RI of detecting biomolecule solution, which is determined by optically interrogating the changing spectrum characteristics of the SPPs [26], and an optoelectronic system that allows optic-electronic signal transfer and data processing. The sensing principle of SPR biosensors is based on the fact that SPPs condition is extremely sensitive to the changes in the refractive index of the dielectric caused by interaction between the analyte of interest and a biomolecule receptor on the sensing surface. This changing condition can thus be tracked by measuring either the angle, the wavelength, the intensity or the phase of the light wave modulated by SPPs in a biosensor [25].

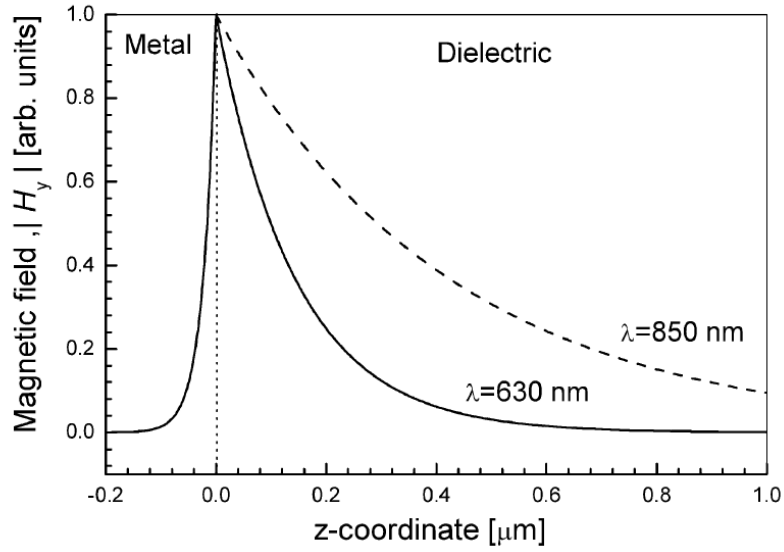


Figure 2.4 Distribution of the magnetic field intensity for a SPP [25].

This is profiled at the interface between gold and dielectric (refractive index of the dielectric 1.32) in the direction perpendicular to the interface calculated for two different wavelengths.

In SPR sensors, the optical system is used to excite SPPs. As followed by Eq. (2), SPPs cannot be directly excited by an incident light at a planar metal-dielectric interface as the propagation constant of a surface plasmon at a metal-dielectric interface is larger than the wavenumber of the light wave in the dielectric. Excitation of a SPP by a light wave can be achieved only if the component of light's wave-vector, that is parallel to the interface, matches the propagation constant of the surface plasmon. Therefore the momentum of the incident light has to be enhanced to match that of the SPPs. This enhancement and subsequent excitation of a SPP are commonly performed by mechanisms of ATR in prism couplers and optical waveguides, and surface diffraction in diffraction gratings [27] as shown in Figure 2.5. As the use of SPR biosensors is increasingly moving beyond the laboratory and into practical applications like clinical service, ease of fabrication, low cost, reliability and reusability are necessarily required.

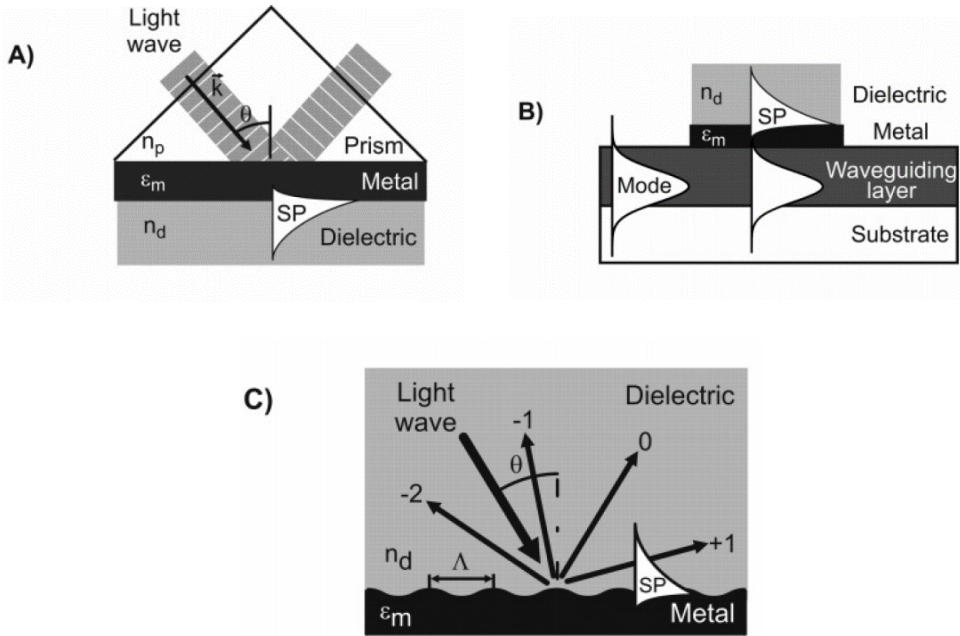


Figure 2.5 Excitation of surface plasmon polaritons [27].

(A) by a light beam via prism coupling, (B) by a guided mode of optical waveguide, (C) by light diffraction on a diffraction grating.

Waveguide-based SPR is critical technology that allows for miniaturization and integration of conventional SPR devices into single and small-sized chips. Complicated optical functions can thus be incorporated into a single device. The use of a planar optical waveguide structure has been investigated by several researchers due to simple control of light wave and the ability to integrate multiple sensing components into a single device fabricated using semiconductor technology [28]. In optical waveguide-based SPR sensors, a light wave is guided by the waveguide and a SPP is excited at the interface of the metal if the SPP and the guided mode are phase-matched [26]. However, the sensitivity of the waveguide-based SPR sensors is actually lower than that of the ATR structures like a conventional prism coupler. Figure 2.6 shows an integrated SPR biosensor based on waveguide structures that consist of a waveguide channel divided into two arms, a sensing

arm and a reference arm by means of Y-splitter [29]. Both arms are rejoined to produce a phase-dependent signal between the two guided modes, which can be measured by an interferometry approach. This device is called Mach-Zehnder Interferometer (MZI). Due to the easy integration and parallelization suitable for waveguides, most SPR biosensors have adopted the waveguide-based SPR structures. Moreover, innovations in the way which SPPs are excited and measured are also required to enhance the biosensor sensitivity.

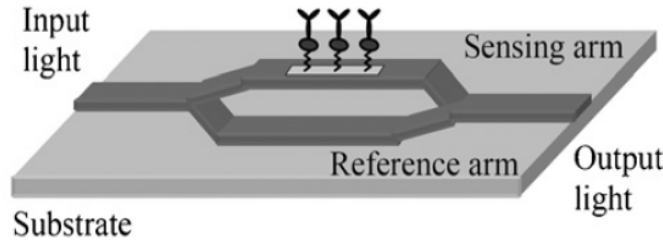


Figure 2.6 A waveguide integrated SPR biosensor [28].

The essential parameters that define the standard quality of SPR biosensors include sensitivity, accuracy, repeatability and lowest detection limit [25]. Sensitivity is defined as the derivative of the monitored SPR parameter output, such as resonant angle or wavelength, with respect to the parameter to be determined, such as refractive index or concentration of analyte. It depends on two factors: the first is the sensitivity of the sensor output to the refractive index, and the second is the efficiency of conversion from the biochemical binding process into the change in the refractive index. Accuracy is described as the degree to which a biosensor output can demonstrate the true values measured from the samples. Repeatability refers to the stability of a biosensor to reproduce same signals under the same measurement setup over a short interval of period. The lowest detection limit describes the lowest concentration of target that can be measured by the sensor. It is

ultimately constrained by the noise which is mainly caused by the intensity fluctuation of the light source, shot noise associated with photon statistics and conversion of the light intensity into electric signal [27]. In order to improve the sensing performance of a SPR biosensor, one possible direction is to increase the sensitivity of the sensor. One viable method is using silver as the metal material. However, the easy oxidation of silver makes it unacceptable for realizing long-term stability of monitoring performance [4]. Another method known as long range surface plasmon resonance (LRSPR) is used to increase the sensitivity of the biosensor, thereby producing a biosensor with better detection performance compared to a conventional SPR biosensor.

2.3 Long Range Surface Plasmon Polaritons Biosensor

2.3.1 Long range surface plasmon polaritons

The studies of long range surface plasmon polaritons (LRSPPs) trace back to the 1980s when the existence of LRSPPs was first predicted by Sarid [30] and then demonstrated by Quail [31]. Following studies on the basis and applications of LRSPPs, such as biosensors, it was determined that LRSPPs contribute to better biosensors due to larger overall sensitivity, lower detection limit and more resistance to interference [32]. LRSPPs are coupled SPPs that are created on a thin metal film embedded between two identical dielectrics. They exhibit longer surface propagation lengths, higher surface electric field strengths and a lower attenuation constant by at least a factor of 2 to 3 [33] [34]. The structure that can couple LRSPPs is referred to as the symmetric metal slab. “Symmetric” means the permittivity of two dielectrics that are bounded on both sides of the metal is the same, as shown in Figure 2.7. In the symmetric metal slab, the bound single interface SPPs

are supported by the individual metal-dielectric interfaces when the thickness of the metal, t is large. When the film is thin enough, the SPPs guided by the interfaces become coupled due to field tunneling through the metal, thus forming supermodes that exhibit dispersion with metal thickness [33] [35]. When the width of the metal film is infinite, there are only two purely bounded TM-polarized bound modes, known as: asymmetric bound (a_b) and symmetric bound (s_b), which represent their transverse electric field components vary asymmetrically and symmetrically respectively. The LRSPP is the s_b mode and has a small attenuation constant. The a_b mode shows a larger attenuation and is often referred as short-range [4]. It is worth noting that the thickness of the metal has to be thin in order for LRSPPs to be coupled, otherwise a_b and s_b degenerate with the single-interface SPPs [33].

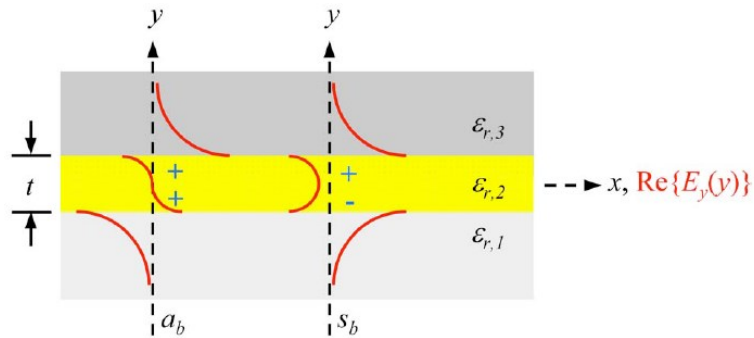


Figure 2.7 Metal slab bounded by semi-infinite dielectrics [33], copyright by OSA Publishing.
where $\varepsilon_{r,2}$ is the permittivity of the metal film, $\varepsilon_{r,1}$ and $\varepsilon_{r,3}$ are the permittivity of the dielectrics. The distribution of the main transverse electric field component is shown as the red curves over the cross section of the structure.

Metal films of finite width provide more practical interest than those of infinite width as they offer 2D confinement in the transverse plane and may be useful for modeling accurate waveguide signal transmission. In the research conducted in [35] [36], it demonstrated that the a_b and s_b mode supported by thin metal films of infinite width embedded in an infinite homogeneous dielectric are divided into four families with numerous higher order ones depending on the symmetry of their fields. In general, the purely bound modes coupled by a metal film of finite width are formed from a coupling of modes supported by each metal-dielectric interface that defines the structure. There are four fundamental modes generated by finite width metal structure: ss_b^0 (symmetric-symmetric bound), sa_b^0 (symmetric-asymmetric bound), as_b^0 (asymmetric-symmetric bound), aa_b^0 (asymmetric-asymmetric bound). Note that a pair of letters identify whether the transverse electric field component is symmetric or asymmetric with respect to the y and x axes; and the superscripts b and l indicate a bound or a leaky mode, respectively. Owing to the innate two-dimensional structure confinement, these modes display EM field variations in both vertical and lateral directions [36]. Figure 2.8 shows the dispersion characteristics with thickness variation by a metal film wave guide with a dimension of $1\mu\text{m}$ in width. As seen from the graphs, it was found that the ss_b^0 mode exhibits the similar characteristics with s_b and its losses diminish with decreasing metal film thickness. Moreover, it has been found its losses can be further reduced by narrowing the width of the metal film and by reducing the background permittivity [35]. Besides the merits above, the LRSPP can be excited using end-fire techniques [36], which makes the ss_b^0 mode of most interest for optical signal transmission in real applications.

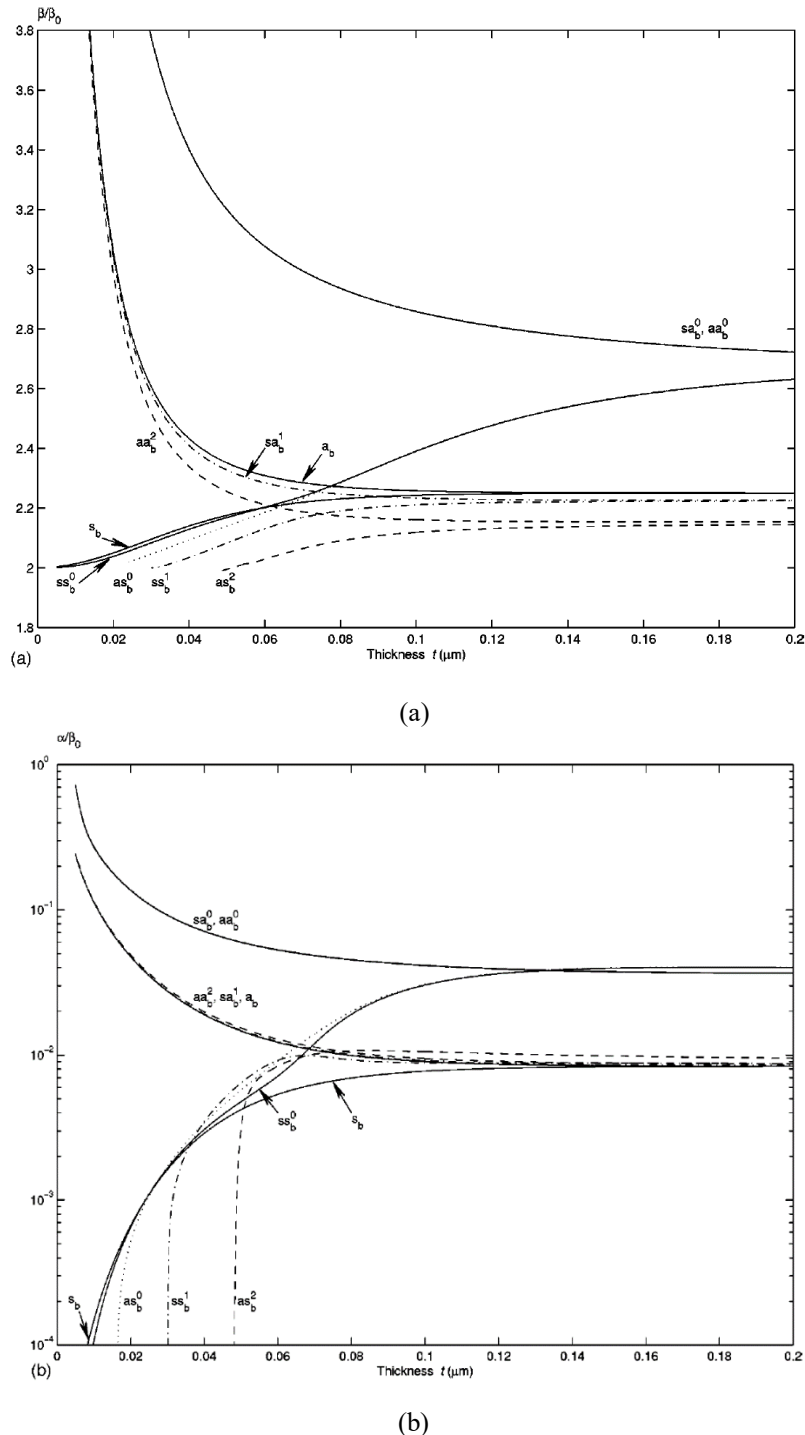


Figure 2.8 The dispersion characteristics with thickness of the first eight modes [35].

The modes are supported by a metal film of width $w = 1\mu\text{m}$. The a_b and s_b modes supported for the case $w = \infty$ are also shown in the pictures for comparison. (a) Normalized phase constant. (b) Normalized attenuation constant.

The waveguide structure comprised of thin metal film of finite width bounded by homogeneous dielectrics can support and propagate LRSPPs. The attenuation and coupling loss of LRSPPs on the waveguides consisting of Au metal film of finite width cladded by an index-matched polymer (Nye Lubricants Inc., OCK-433) are measured by the work [37]. In this work, the waveguide architectures shown in Figure 2.9 are used to couple LRSPPs at the operating free-space wavelength $\lambda_0 = 1550\text{nm}$. The dimension parameters of the waveguide architectures need to be well tuned to make sure only the ss_b^0 mode can be coupled while other modes will be cut off. The attenuation measurements of the Au waveguides are illustrated in Figure 2.10. It is shown that the experimental and theoretical attenuations match very well for the waveguide structures. The capability of coupling the ss_b^0 mode in the symmetric finite-width metal film waveguide renders it useful for integrated optical applications such as LRSPP biosensors.

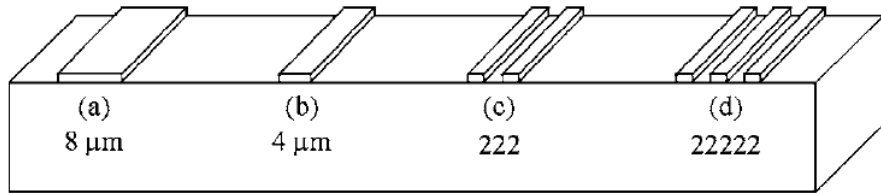


Figure 2.9 The waveguide architectures used for coupling LRSPPs [37].

(a) $8\mu\text{m}$ wide Au film, **(b)** $4\mu\text{m}$ wide Au film, **(c)** two $2\mu\text{m}$ wide Au films with a space of $2\mu\text{m}$ in between, **(d)** three $2\mu\text{m}$ wide Au films with a space of $2\mu\text{m}$ in between.

2.3.2 LRSPP biosensor

In this section, a LRSPP biosensor device, based on waveguides which is relevant to this work, will be presented. In the matter of LRSPP biosensor application, keeping the index of the dielectrics surrounding the metal film symmetric is important to realize the ss_b^0 mode coupling to increase the sensitivity of the biosensor. In most sensing cases, the water-based sample with an approximate index of 1.33 is filled in the chamber of the device, and the dielectric material must be in the same refractive index in order to build a symmetric structure. A symmetric LRSPP device using benzocyclobutene (BCB) was fabricated and studied in [38]. Although the ss_b^0 mode of LRSPPs was excited by end-fire coupling, the device is unsuitable for a biosensing application as the refractive index of BCB is 1.537, much higher than that of water, which makes the device asymmetric.

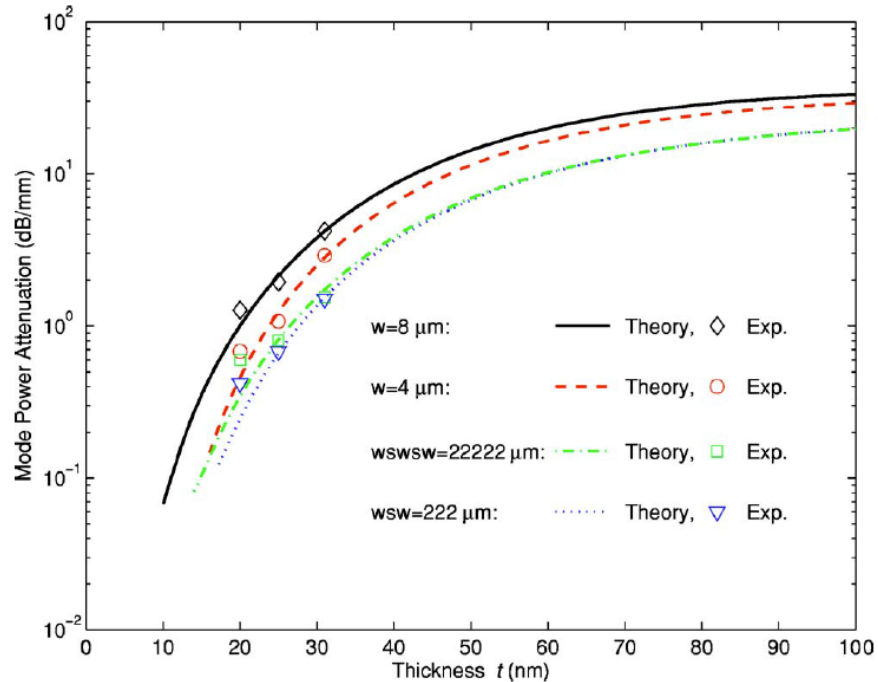


Figure 2.10 The theoretical and experimental attenuation of all Au waveguides in different width and separated space [37].

The biosensor fabricated in this work is using CYTOP as the dielectric material. CYTOP is an amorphous fluoropolymer that shows high transmission in the visible light spectrum and electrical insulation. The most important reason for the selection of CYTOP as the dielectric material is that its refractive index is 1.3348 at wavelength of 1300nm, slightly above that of water (1.33 at 20°C) [39]. Additionally, CYTOP is impervious to water, oil and most chemicals including most acids, alkaline and organic solvents that are commonly used in semiconductor processing. In the previous work [39], LRSPP waveguides consisting of Au film on CYTOP, and covered with an index-matched aqueous solution were characterized at a free-space operating wavelength of $\lambda_0 = 1310\text{nm}$. The ss_b^0 mode was coupled by a broadside modal overlap fiber coupling technique. The measurement of the mode power attenuation (MPA) of LRSPPs were very close to the theoretical value which is 7.1dB/mm. This work provides validation of the LRSPP waveguide sensing application using Au film bounded by CYTOP dielectric to support the excitation and propagation of the ss_b^0 mode of LRSPPs.

According to the manufacturer, three types of CYTOP are available: A-grade, M-grade and S-grade, each classified by the functional polymer end group which determines the adhesion mechanism as shown in Figure 2.11. The S-grade was used as an optical cladding material in the previous work [40] [41] [42] [43]. Since the S-grade was not designed for adhesion to metal, an additional diluted M-grade was applied on the top of the cladding to improve adhesion with Au waveguides [44]. However, severe cracking issues were found when spinning the first thinner layer of CYTOP S-grade on top of the lower cladding CYTOP stack, leading to a zero yield of the whole wafer. Potential reasons and solutions

for this problem are discussed in section 3.5. An additional issue is that M type CYTOP does not exhibit sufficient mechanical stability during wafer dicing [45]. Successful fabrication trials with CYTOP A-grade led to selection of this material for this research as it demonstrated good adhesion to Au waveguides and thickness could be increased through multiple coats without severe cracking issues observed in [44].

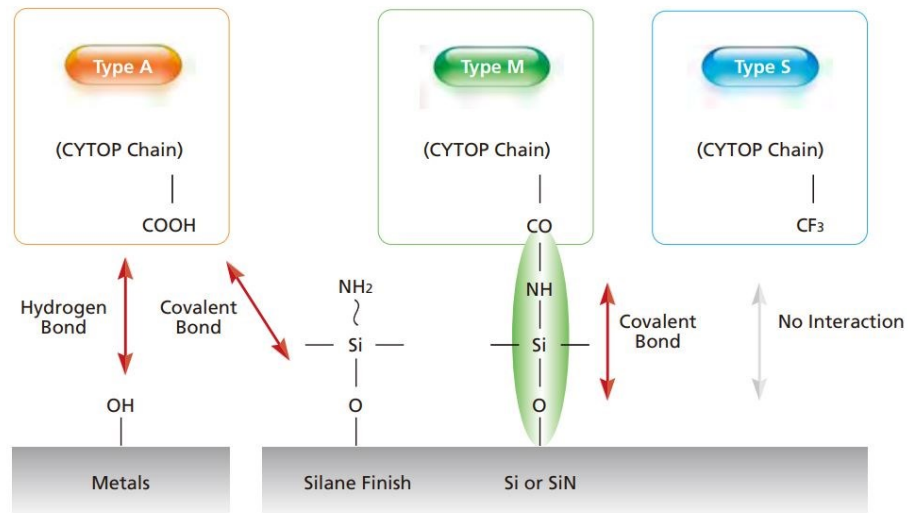


Figure 2.11 Adhesion mechanism for three types of CYTOP [copyright by AGC., Ltd]

A cross-sectional view of the device structure fabricated in the current work is illustrated in Figure 2.12. The sensing element of the device contains thin stripe Au waveguides with dimensions of 35nm in thickness and 5μm in width. The waveguide is supported by a layer of CYTOP with a thickness of at least 8μm, and is covered with a second layer of CYTOP also at least 8μm thick [40]. The sufficient thickness of the lower CYTOP clad makes sure that the Si substrate is optically far enough from the Au film to not seriously impact LRSPP modes. 35nm thick Au waveguides for sensing are located in fluidic channels which are formed by plasma etching. The thickness of Au film is considered to be in a good range

since the LRSPP mode remains bound to the surface of the film with reasonably low attenuation at this condition. Higher thickness leads to fast attenuation of the LRSPP mode and much lower thickness results in weak binding of the LRSPP mode. Reference Au waveguides are fully embedded in CYTOP to isolate them from contacting the test fluid. With the refractive index of CYTOP closely matching that of water, both sensing and reference waveguides support an optically symmetric mode. When a thin layer of biosample is present on the surface of the Au waveguides, a shift in the propagation length of LRSPP mode will be caused by changes in the attenuation constant as well as wave velocity. The former can be detected in a straight waveguide by monitoring the output power, and the latter can be detected in an optical interferometer such as MZI by monitoring the shifts in the phase of the output beam [42]. In the biosensing operation, Au waveguides in fluidic channels will be surrounded by dilute aqueous solution containing a target analyte, and will be excited by a LRSPP signal. Amplitude and phase behavior of the LRSPP mode will be monitored to determine if the target material of interest is present in the test solution. In my research, the testing work only focuses on the straight waveguides. In a straight waveguide, LRSPP is excited from one end of the waveguide and a photodetector is used to measure the signal from the other end through the optical facets. As the surface of the Au waveguide is binding with the bio-target, the output changes from the original signal. The degree where the bio-chemical solution affects the output depends on its refractive index [42]. The device is featured by the length of waveguides which includes 3.2mm, 3.5mm and 4.8mm. The purpose of dicing waveguides at various lengths is to functionalize the relationship between LRSPP power loss and waveguide length which will determine the LRSPP attenuation.

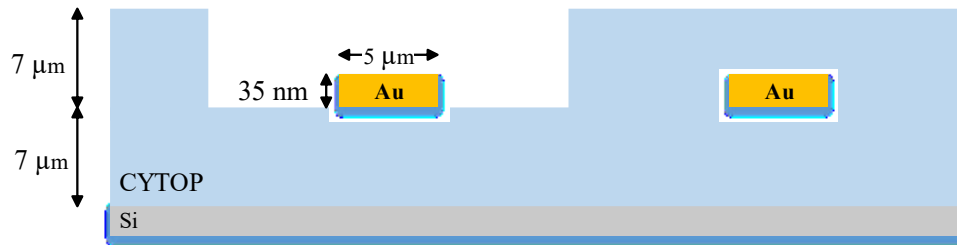


Figure 2.12 Cross-sectional profile of device structure

A generalized fabrication process for the device is illustrated in Figure 2.13, showing key steps and all materials used in the procedure. The process begins with cleaning and surface silanization of the wafer to ensure strong adhesion between CYTOP and the substrate. Next a thick cladding of CYTOP A-grade was spin-coated on the substrate and fully cured to prepare a uniformly even and electrically insulating polymer substrate with good transparency. Next, the 35nm thick Au waveguides were patterned on top of the cured CYTOP cladding by conducting a bi-layer lithography procedure, Au deposition and lift-off process in a sequence shown from Figure 2.13 (c) to Figure 2.13 (e). The quality of the Au waveguides including surface roughness and thickness accuracy is critical to achieving good optical performance of final devices. This indicates that all the fabrication parameters involved in waveguides patterning must be precisely controlled in order to obtain a good quality of Au and the waveguides need to be preserved intact from the Au patterning to the end of fabrication. In the following procedures shown in Figure 2.13 (f) to Figure 2.13 (h), a 70nm thick layer of SiO₂ was patterned to cover the area where fluidics channels were defined. It acts as an etch stop to prevent the O₂ plasma from etching CYTOP below the waveguide level, and also protects the covered Au waveguides from being affected by materials used at the upcoming steps. After these steps, a second thick cladding of CYTOP

was applied on the wafer to embed the waveguides inside so that a structure of CYTOP-Au-CYTOP stack could be realized to support a symmetric LRSPP mode. At the steps shown from Figure 2.13 (j) to Figure 2.13 (l), fluidics channels were defined by lithography and etched by O₂ plasma with Al mask until they stopped at the layer of SiO₂ without any over-etching. Waveguides in the channels were exposed after the SiO₂ stop layer was removed by buffered oxide etch (BOE) as shown in Figure 2.13 (m). The final step was dicing the wafer into small chips for testing purpose. In the next chapters, the fabrication steps are described in detail. Fabrication issues resulting in device failure are specifically discussed with robust process improvements being also explored by repeatable and successful trials.

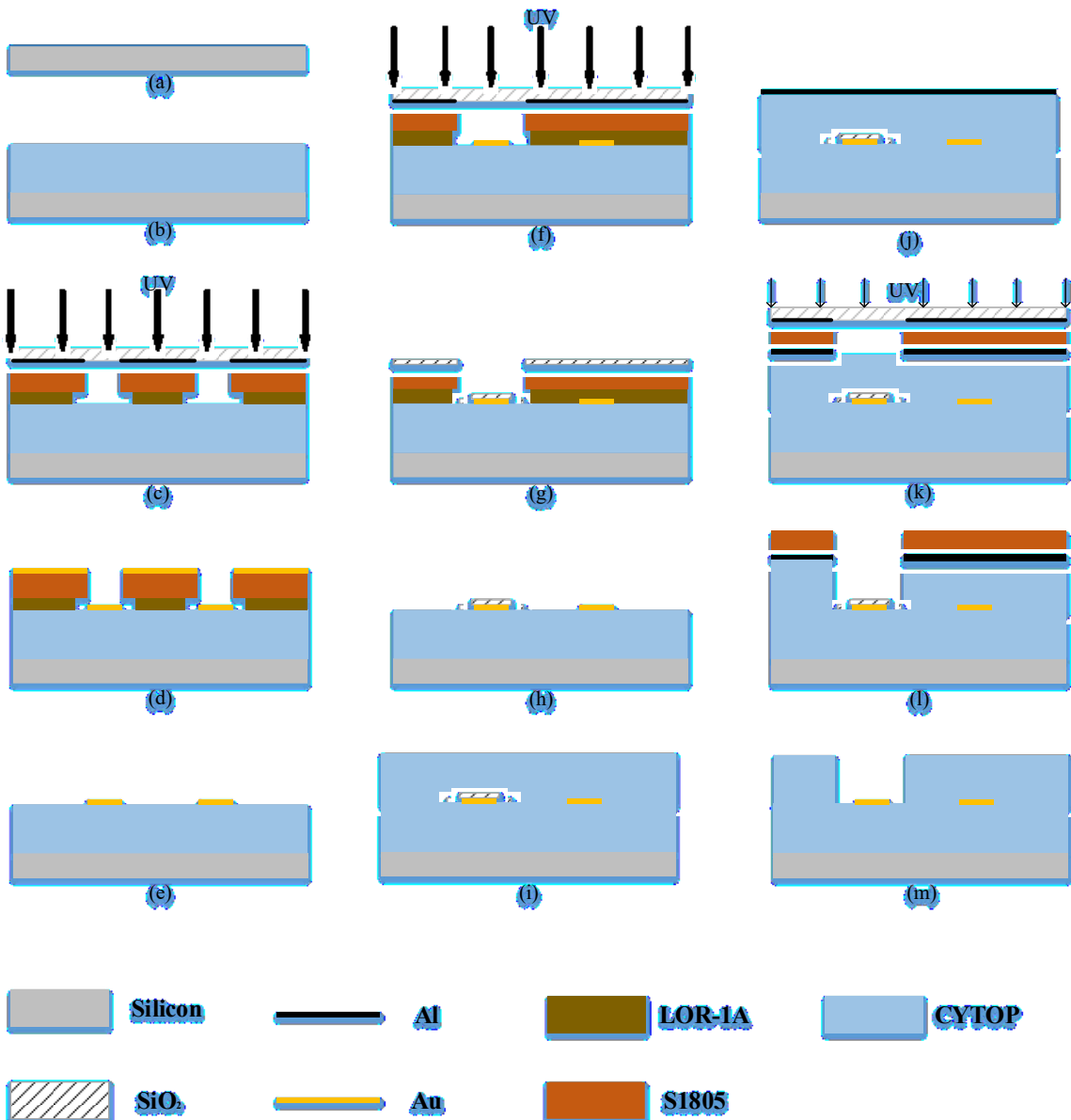


Figure 2.13 Process flow for fabricating the LRSPP device

(a) Surface silanization of substrate; (b) CYTOP coating; (c) Patterning of bi-layer photoresist to form waveguides feature; (d) Au deposition by thermal evaporation; (e) Lift-off to form Au waveguides; (f) Patterning of bi-layer photoresist to form etch stop layer feature; (g) SiO₂ deposition by E-beam evaporation; (h) Lift-off to form etch stop layer; (i) CYTOP coating; (j) Al deposition by E-beam evaporation; (k) Photoresist coating and patterning of photoresist and Al mask for formation of fluidic channels; (l) Reactive ion etching of fluidic channels; (m) Photoresist and Al mask removal.

3 Chapter: Fabrication of Surface Plasmon Biosensor in CYTOP

In this chapter, a fabrication process for LRSPP waveguides on CYTOP with incorporated micro-fluidic channels is presented in detail. The process described in this chapter can be divided into wafer preparation, lower CYTOP cladding, waveguide patterning, etch stop layer patterning, upper CYTOP cladding, and fluidic channel formation. There are two innovative process steps introduced. One is that an etch stop layer was patterned in the channel area to prevent waveguides in the channel from being over-etched. The other is that Al mask was patterned to replace the photoresist SPR-220 in order to eliminate the photoresist cracking which is believed to result from the soft bake step in patterning SPR-220. Some process modifications based on the previous research [40] [41] [42] [43] [44] are discussed in this chapter as well.

3.1 Wafer Selection and Preparation

The purpose of this step is to make wafers with a clean surface suitable for CYTOP coating. In this work, 4" silicon wafers were used as a device substrate only to provide a structural base that supports the sensing devices; the silicon does not enable any sensing function. Therefore, wafer doping did not influence performance of the final devices. To avoid excessive initial wafer curvature, new wafers were checked and selected by means of film stress measurement to ensure surface flatness. Wafers with low initial curvature measurement were chosen as eligible wafers for the upcoming fabrication steps. The selected wafers were then scribed with a tracking number on the backside so that they could be easily identified for troubleshooting if any fabrication issues arose during processing.

Twelve wafers were selected for the initial batch and began with surface cleaning. Wafers were dipped in Piranha solution for 10 minutes at 90°C to remove any organic surface contamination. The Piranha solution is a mixture of sulfuric acid and hydrogen peroxide with a ratio of 4:1. It cleans the wafer surface by removing almost all organic matter due to its strong oxidization characteristics, and also can hydroxylate the silicon surface by adding OH group, making the surface highly hydrophilic. The resulting ultraclean surface is a primary requirement for coating of (3-Aminopropyl)triethoxysilane (APTES) silane coupling agent in the following step. APTES is an aminosilane commonly used for covalent bonding of organic films to silicon. After piranha etch cleaning, the wafers were immersed in a 0.05% APTES solution for 10 minutes with agitation. Following this each wafer was rinsed in ethanol and blown dry in N₂, then baked on a hotplate for 20 minutes at 115°C in order to eliminate APTES residue and dehydrate the wafers. The APTES film is required to promote adhesion between CYTOP A-grade and a silicon substrate by providing alkoxysilane molecules that can be covalently bonded to carboxyl groups (-COOH) in the CYTOP A-grade.

The wafer preparation in this process was significantly modified from the previous work in [40] [41] [42] [43] [44] due to the use of CYTOP A-grade, which offered the best adhesion when used in conjunction with the APTES. Previous processes applied a diluted M-grade on the substrate as an adhesion layer, with subsequent S-grade layers used as a cladding dielectric material. Two different CYTOP grades were required, as S-grade possesses limited adhesion to a silicon substrate due to its polymer-end group function. More details on better adhesion for different types of CYTOP can be found in [46].

3.2 Lower CYTOP Cladding

At this first step of fabrication, a CYTOP stack with thickness of 8 μm was built on the silicon substrate by multiple spin coating. Process details for this lower CYTOP cladding are given in Table I. High purity N₂ was used to blow the surface clean prior to each coating of CYTOP, and to ensure it was free from particles that could build up residual stress, causing defects and cracking on the surface of the CYTOP cladding. Three layers of 9% CTX-809A CYTOP was applied by the conventional method of spin-coating with a 30 second spin at 1500rpm to attain approximately 8 μm in thickness. After each layer was coated, the wafer was allowed to rest at room temperature for 5 minutes followed by a soft-bake at 50°C for 10 minutes on a hotplate. The soft-bake step enabled removal of bubbles and some solvent. After the last layer was coated and soft-baked, the wafer was baked at 200°C for 2.5 hours by multiple ramping steps on the hotplate to completely evaporate the solvent in the resin and improve adhesion with the silicon substrate [47].

Table I Lower CYTOP Cladding Fabrication Process

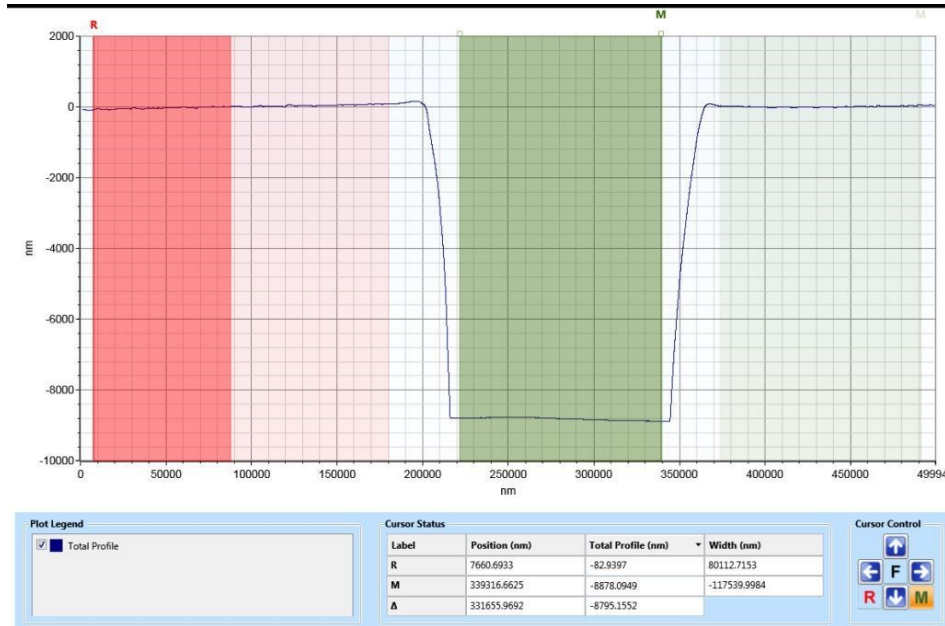
Step	Description	Details
1	Spin coat 9% CTX-809A CYTOP	550rpm for 10s to spread, followed by 1500rpm for 30s.
2	Soft-bake for degas	Rest at room temperature for 5 minutes, followed by a 50°C soft bake for 10 minutes on a hotplate.
3	Repeat steps 1 and 2	Three spins achieve more than 8µm thick layer.
4	Hard bake for CYTOP curing	Ramp at 150°C/hr from 50°C to 80°C, hold at 80°C for 1 hour, then ramp up to 200°C at 150°C/hr, hold at 200°C for 2.5 hours, then cool down to room temperature. All Baking completed on a hotplate

In order to optimize coating results, both static coating and dynamic coating were tried. Static coating is simply dispensing a small volume of coating material on the center of a static wafer before the wafer begins rotating. Dynamic coating is the process of dispensing liquid while the wafer is rotating at low speed. This coating technique is advantageous for coating materials with poor wetting ability, and it leads to reduced material waste when compared to static coating. The static approach required dispensing a larger volume of material to ensure full coverage of the substrate. Theoretically, dynamic coating is a better option especially for CYTOP, which is a highly viscous liquid. However, due to lack of an automated dispensing system on our equipment, we found that the dispensing position cannot be centered precisely by hand and this results in serious layer thickness variation. In the end, a static spin was chosen in our process as a compromise between higher CYTOP consumption and improved surface thickness uniformity.

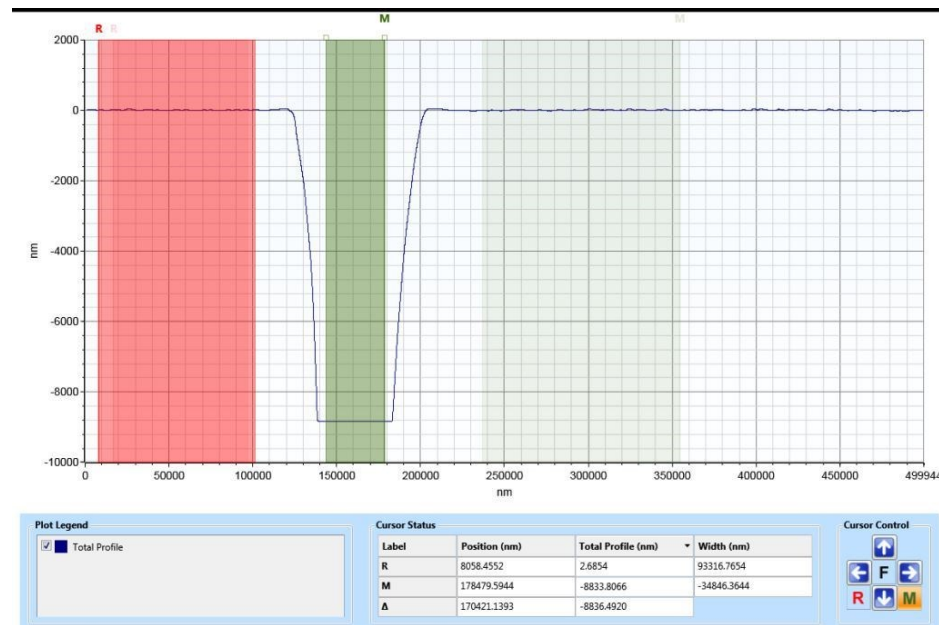
The lower CYTOP cladding preparation was adapted with moderate modifications from the previous work [40] [41] [42] [43] [44]. Specifically, there were two modifications involving baking temperature and time. In the first process modification, the soft-baking period shown at step 2 in Table I was shortened from 30 minutes to 10 minutes and a 5 minute long rest step at room temperature for degas was introduced. The soft-bake period was decreased by 20 minutes to promote improved adhesion with the next layer to be applied. In the manufacturer's documentation [46], it is noted that the peel strength becomes weak when a second layer is applied on top of a fully cured layer, and it is suggested that each layer should be baked at a low temperature between 50°C to 100°C and for a short period of 1 to 10 minutes long when spin-coating multiple layers of CYTOP.

Resting at room temperature for 5 minutes is recommended to reduce the bubbles generated from pouring CYTOP out of the bottle. In the second process modification, an additional 1 hour bake interval at 80°C was added in the hard-bake step as shown at step 4 in Table I. This action was taken to ensure that the solvent evaporated slowly. Otherwise the surface would become rough or uneven due to rapid release of trapped solvent at higher temperatures.

The thickness of the lower CYTOP cladding is an important parameter that needs to be at least 8 μ m so that LRSPP excitation can be confined in the CYTOP cladding. To measure the thickness, CYTOP cladding was patterned with a testing photo mask by lithography. The CYTOP was then etched in an O₂ plasma under the protection of a layer of MicroChem SPR-220, a thick photoresist used as an etch mask. The etching was conducted for 20 minutes to ensure the exposed CYTOP had been completely removed, exposing the silicon substrate underneath. A Tencor P-1 stylus profilometer was used to measure the step height at the edge of the etched feature. The measured results of the CYTOP cladding thickness are shown in Figure 3.1. The surface roughness is another significant factor to be examined because it will be transferred to the Au waveguides deposited on top, and will affect scattering loss in the Au waveguide. The surface roughness of CYTOP was measured by atomic force microscopy (AFM). The scanning surface profile with dimension of 1 μ m \times 1 μ m was imaged and the root mean square (RMS) value and average value of roughness were calculated and shown in Figure 3.2. It is noted that both the average value and RMS value of roughness are around 0.3nm and it is within the acceptable range (<1nm) according to previous studies [37].



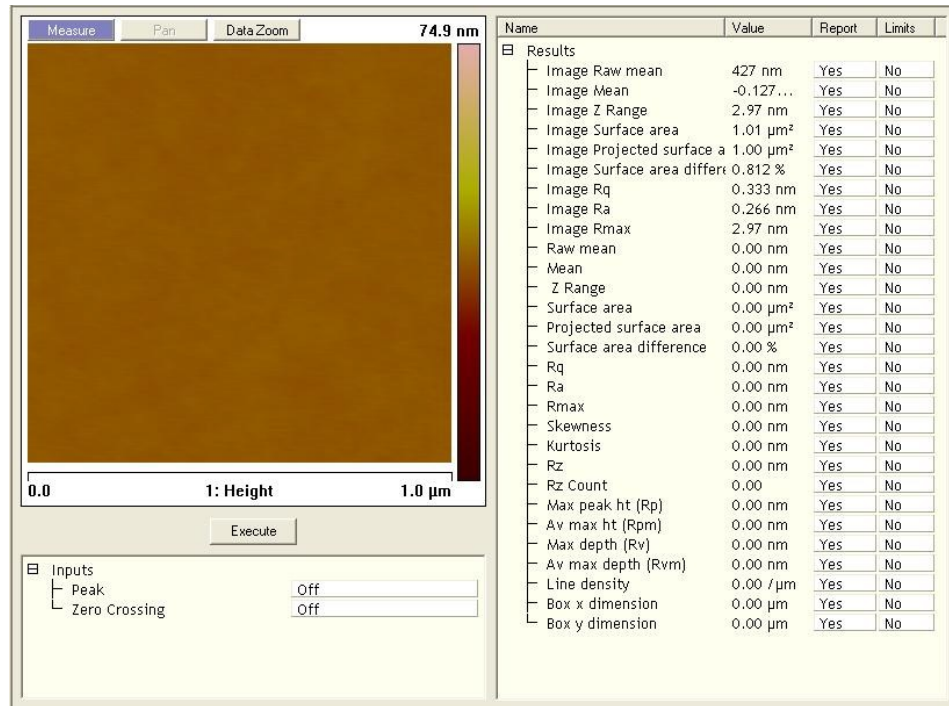
(a)



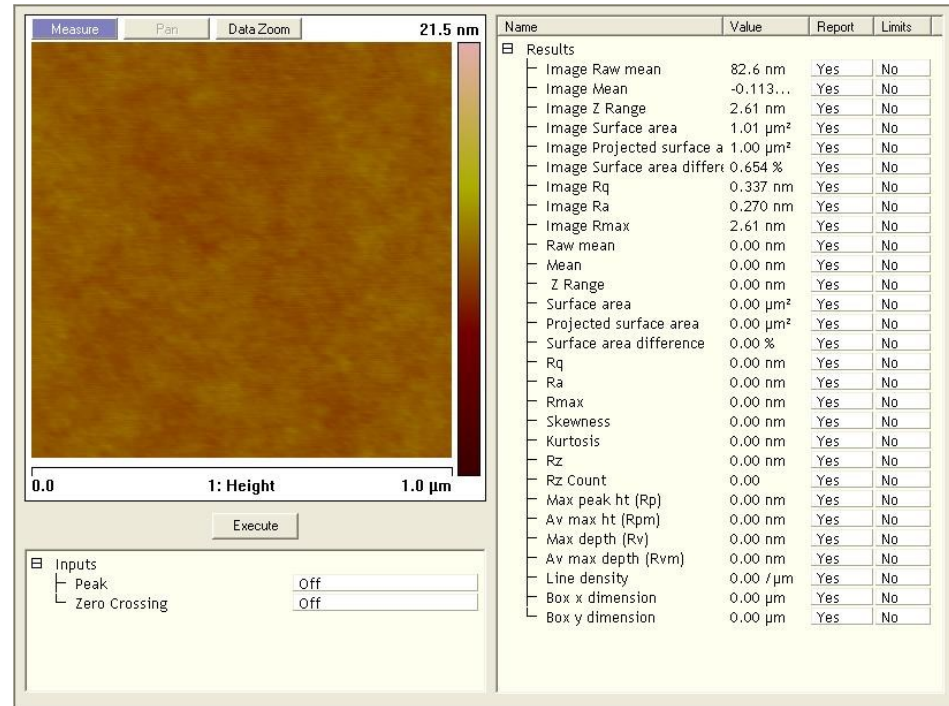
(b)

Figure 3.1 Thickness measurement of lower CYTOP cladding.

(a) (b) show the thickness of one channel of CYTOP in different positions of the same wafer. (a) shows the thickness is approximately $8.8\mu\text{m}$; (b) shows the thickness is approximately $8.8\mu\text{m}$. The thickness uniformity demonstrates that a uniformly $8 \mu\text{m}$ layer of CYTOP can be applied by the lower cladding process



(a)



(b)

Figure 3.2 AFM surface scanning results of lower CYTOP cladding.

(a)AFM surface scanning result of center of the wafer; (b) AFM surface scanning result of upper side of the wafer. The relevant parameters in the pictures are “image Rq” and “image Ra” which represent for roughness RMS value and roughness average value.

3.3 Au Waveguide Patterning

This chapter describes in detail the patterning of Au waveguides on top of a lower CYTOP cladding using bi-layer lithography, Au thermal evaporation and lift-off procedures. The process-sensitive parameters were optimized to determine the accurate width and thickness of Au waveguides as they are critical to the performance of the sensing device.

3.3.1 Bi-layer Lithography

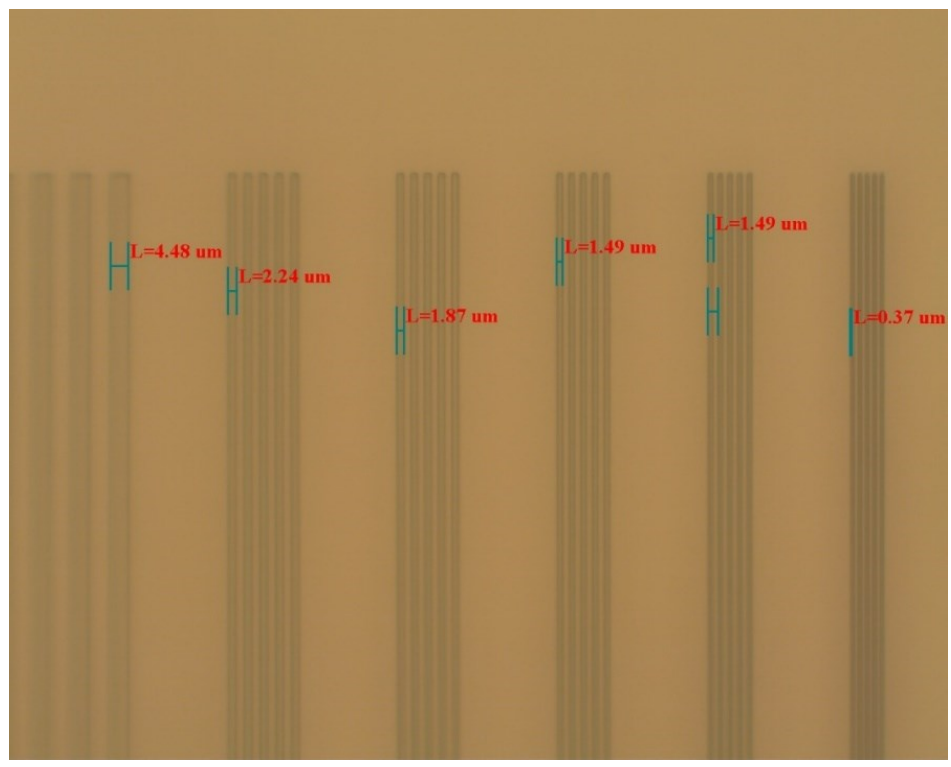
Bi-layer lithography is a microfabrication technique widely used to achieve submicron dimension features in thin metal films. A key step is the creation of an undercut structure through removal of a liftoff resist below a more robust photoresist top layer. Following metal deposition, the deposited film is patterned when the sacrificial layer is washed away in a solvent together with top photoresist and any metal deposited on it. Steps of the bi-layer lithography of Au waveguides is summarized in Table II. The complete process was performed in a class 100 clean room with temperature controlled between $22^{\circ}\text{C} \sim 25^{\circ}\text{C}$ and relative humidity controlled between $40\% \sim 43\%$. In this bi-layer lithography process, LOR-1A and S1805 (trademarks by MicroChem) were used as liftoff resist and photoresist respectively. S1805 is a positive photoresist that can be exposed with a UV source in the spectrum output range of 350nm to 450nm [48]. LOR-1A is not photo-sensitive to UV exposure but is susceptible to etching in a photoresist developer, where the etch rate is affected by both baking time and baking temperature [49]. The developer is MF-321(trademark by MicroChem), a 1.91% Tetramethylammounium hydroxide (TMAH) based solution which removes both exposed S1805 and LOR-1A.

Prior to spinning LOR-1A on the wafer, the surface was ashed by O₂ plasma in the MARCH JUNIPER II reactive-ion etching (RIE) system (operation condition: power: 70W, gas flow: 60sccm, and pressure: 430mTorr) for 30 seconds. From past experience, it is difficult for LOR-1A to spin evenly across the entire wafer without any surface treatment due to extreme hydrophobicity of fully cured CYTOP. This step was to increase hydrophilicity of the surface in order that LOR-1A can be evenly coated with a uniform coverage. After the wafer was given O₂ plasma treatment, a layer of LOR-1A was spin-coated with a spread at 1000rpm for 10 seconds followed by a spin at 4000rpm for 30 seconds, and was baked on a hotplate at 180°C for 3 minutes. According to the manufacturer's documentation [49], the etch rate of LOR-1A soft-baked under this thermal condition is approximately 3nm/s. A layer of S1805 was spin-coated with the same spin speed and time as LOR-1A, and was baked on a hotplate at 115°C for 3 minutes for solvent evaporation. Thickness of LOR-1A and S1805 were measured, giving results of 105nm and 500nm respectively [41]. These thickness values were acceptable considering the thickness of LOR-1A was more than 3 times thickness of the 35nm Au waveguides. Once the bi-layer was properly prepared, the wafer was UV-exposed by a Karl Suss MA6 mask aligner at H-line (405nm) spectrum and the positive photoresist, S1085, in the exposed area became soluble. To accurately define feature dimensions consistent with those on the photomask, especially for features on the order of the wavelength of H-line, the exposure dose is a critical parameter. In previous work [44], it was shown that optimal exposure dose depends on the thickness of lower cladding and a lower dose will be required with a thicker CYTOP stack. This effect is attributed to additional dose resulting from more substrate reflection when working with CYTOP layers. A dose of 114mJ/cm² was suggested for

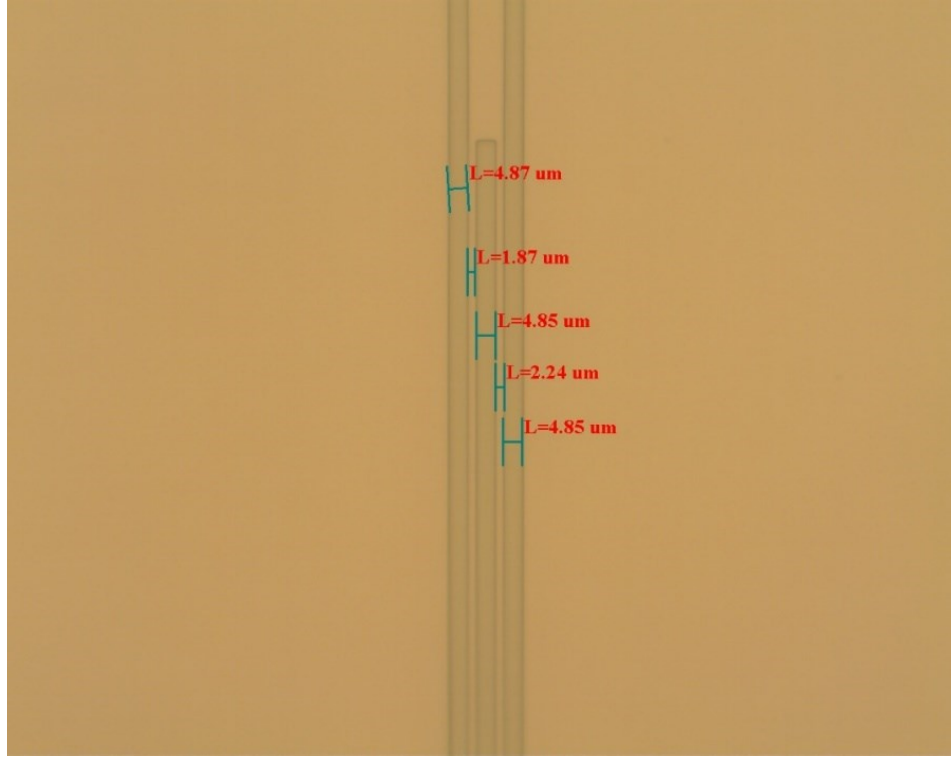
optimum resolution. After exposure, the wafer was developed in MF-321 for 50 seconds. The developing time needs to be carefully controlled to create the undercut in the bi-layer structure. Lithography results are illustrated in Figure 3.3. From the resolution test features, it is shown that the resolution achieved is better than $1\mu\text{m}$, which satisfies the waveguide critical dimension of $2\mu\text{m}$, measured at the gaps between the triple waveguides.

Table II Au Waveguides Bi-layer Lithography Fabrication Process

Step	Description	Details
1	RIE surface ashing	O_2 plasma etching for 30 seconds.
2	LOR-1A spin coating	Spread at 1000rpm for 10 seconds; Spin at 4000rpm for 30 seconds.
3	Prebake on a hotplate	Bake at 180°C for 3 minutes.
4	S1805 spin coating	Spread at 1000rpm for 10 seconds; Spin at 4000rpm for 30 seconds.
5	Prebake on a hotplate	Bake at 115°C for 3 minutes.
6	Exposure	H-line. Dose: 114mJ/cm^2 .
7	Developing	Developer: MF-321; Developing time: 50 seconds; Developing temperature: Room temperature.



(a)



(b)

Figure 3.3 Microscope images of Bi-layer lithography

(a) resolution indicator mark (b) triple waveguides

3.3.2 Au Waveguide Metallization

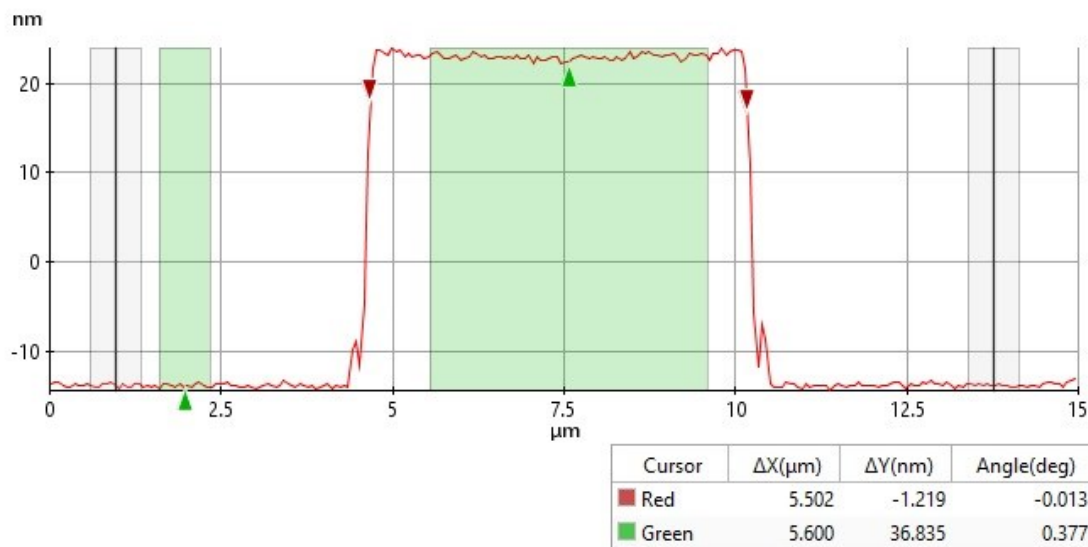
After the waveguide pattern was realized by bi-layer lithography and verified by optical inspection, a 35nm thick Au film was deposited by metal evaporation. The Balzers Model BA-510 metal film evaporation system was run under a very high vacuum pressure (typically the order of 10^{-7} Torr) to ensure better film quality. There are two methods available for metal evaporation: E-beam evaporation and thermal evaporation. In previous research [42], both methods were performed and analyzed. Compared with thermal evaporation, E-beam evaporation consumes more Au material and can produce an unstable deposition rate at the beginning of the deposition. For this reason, thermal evaporation was used for Au film deposition in this work. In Au film deposition, film deposition rate and tooling factor are two key parameters that need to be carefully chosen and monitored as they control roughness and thickness of the deposited thin film. The relationship between deposition rate and surface roughness of deposited material has been discussed in [50]. This work suggested an optimal deposition rate of 1Å/s for the Au thin film, determined by considering the film quality achieved at different deposition rates. The tooling factor is a parameter the deposition controller uses to monitor actual film thickness during deposition. It corrects the difference in material deposited on Quartz Crystal Monitor (QCM) and the substrate. The tooling factor is unique for independent deposition equipment, deposition material, and conditions. This means different tooling factors need to be set for particular processes. Several Au deposition trials under different tooling factors were performed and their roughness and thickness results were measured by AFM. By iterative calculation using

$$\text{New tooling factor} = (\text{actual thickness}/\text{desired thickness}) \times \text{tooling factor used} \quad (3)$$

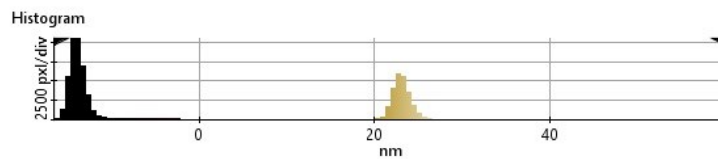
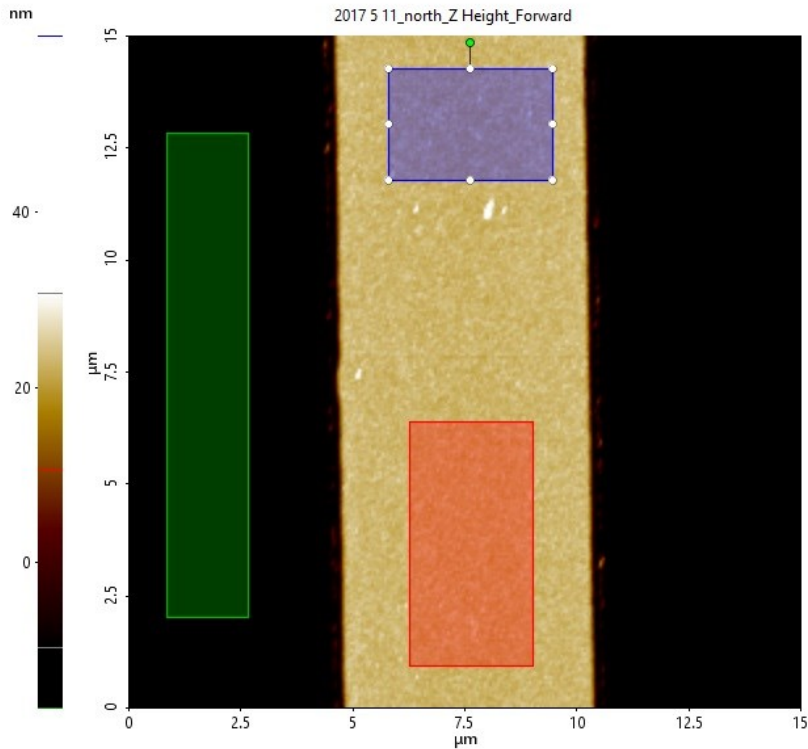
after each deposition trial and AFM measurement, the tooling factor was optimized in order to attain the best quality of Au film. Film specifications were: film roughness < 1nm and film thickness = $35\text{nm} \pm 2\text{nm}$. Figure 3.4 shows the AFM measurement of the Au film deposited using a tooling factor of 175, and demonstrates roughness and thickness within the acceptable range. Final deposition parameters included a rate of 1\AA/s and tooling factor of 175. After 35nm Au deposition, the wafer was immersed in remover PG (trademark by MicroChem), a photoresist stripper used to lift-off the unwanted material. After 30 minutes the bi-layer structure together with Au film coated on it was removed, leaving the Au waveguides. The remover PG was heated to 60°C so that LOR-1A was more quickly removed. In the previous work [40] [41] [42] [43] [44], 1165 (trademark by MicroChem) was used as a photoresist stripper. The 1165 must be heated to 80°C to enable an efficient lift-off process. The lower working temperature (60°C) of remover PG (trademark by MicroChem) is preferred as elevated temperatures can lead to deformation of waveguides. To ensure the wafer is clear of LOR-1A and S1805 residue, a second remover PG bath with ultrasonic agitation is used. More than 30 minutes of immersion may be required for the lift-off process since it can be slow for LOR-1A to peel off especially when it is covered by heavy metal like Au. The liftoff images of single waveguide, triple waveguides, T-junction, V-crotch are shown in Figure 3.5(a) ~ (d). The results shown are of good quality: the width of waveguides is in the acceptable range ($5\mu\text{m} \pm 0.5\mu\text{m}$); the edge of waveguides is square and clear; junctions are distinguishable. This demonstrated the process was conducted in a proper manner. The metallization process details are listed in Table III.

Table III Au Waveguides Metallization Fabrication Process

Step	Description	Details
1	Au deposition	Au thickness: 35nm Deposition rate: 1Å/s Tooling factor: 175
2	Lift-off	30 minutes in remover PG at 60°C; Ultrasonic agitation for 10 seconds; Repeat above steps until the bi-layer residue is removed.
3	Dehydration	Bake at 50°C on a hotplate for 48 hours.



(a)



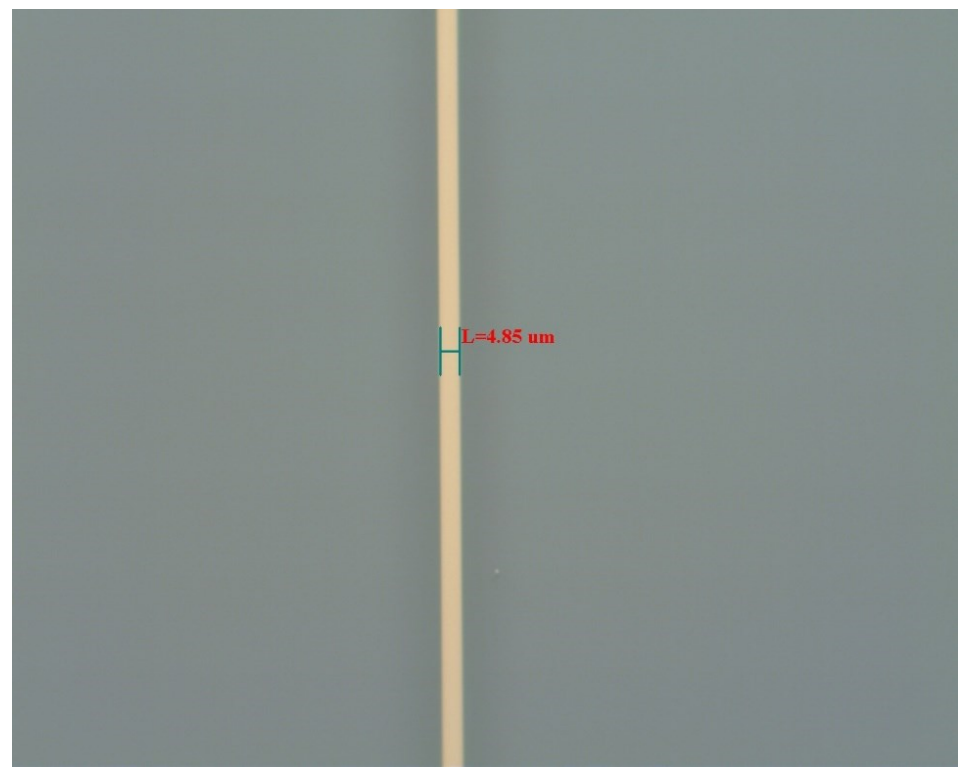
Statistics										
Region	Min(nm)	Max(nm)	Mid(nm)	Mean(nm)	Rpv(nm)	Rq(nm)	Ra(nm)	Rz(nm)	Rsk	Rku
Red	20.128	27.533	23.831	22.797	7.405	0.948	0.748	6.558	-0.443	3.396
Green	-16.532	-10.788	-13.660	-14.077	5.745	0.805	0.639	5.396	-0.426	3.181
Blue	20.238	28.960	24.599	22.923	8.721	0.979	0.771	7.238	-0.627	4.168
R-G	36.660	38.320	37.490	36.874	1.660	0.143	0.109	1.161	-0.017	0.216
R-B	-0.110	-1.427	-0.768	-0.126	-1.317	-0.031	-0.022	-0.681	0.185	-0.771
G-B	-36.770	-39.747	-38.259	-37.000	-2.977	-0.174	-0.132	-1.842	0.201	-0.987

(b)

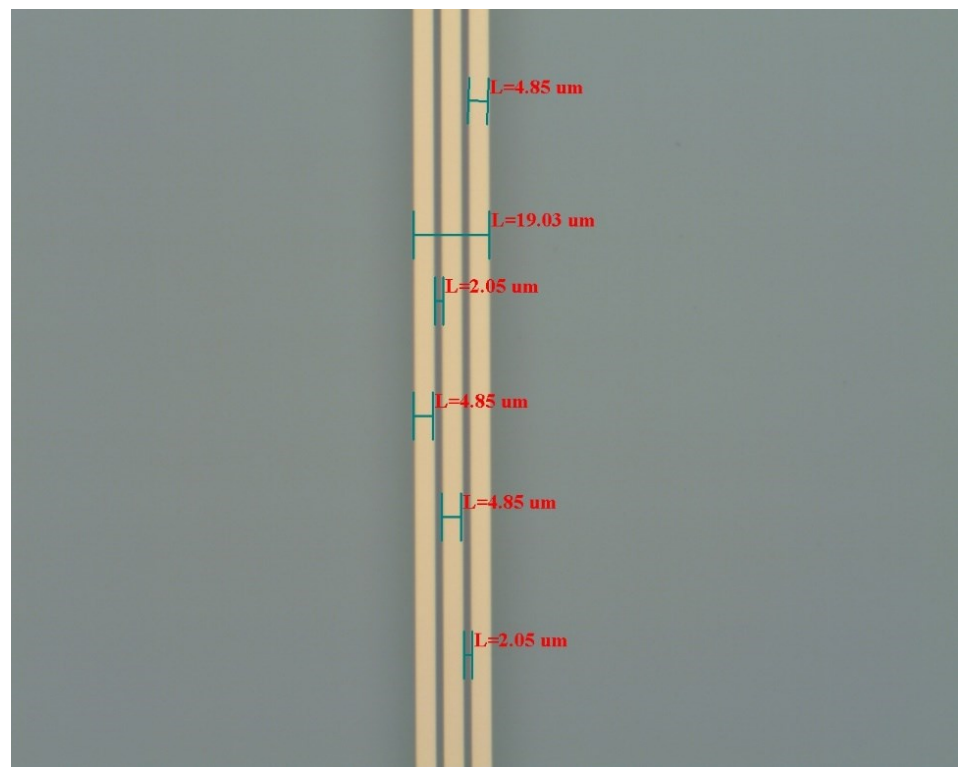
Figure 3.4 AFM measurement of roughness and thickness.

(a) Au waveguide thickness measurement: 36.835nm.

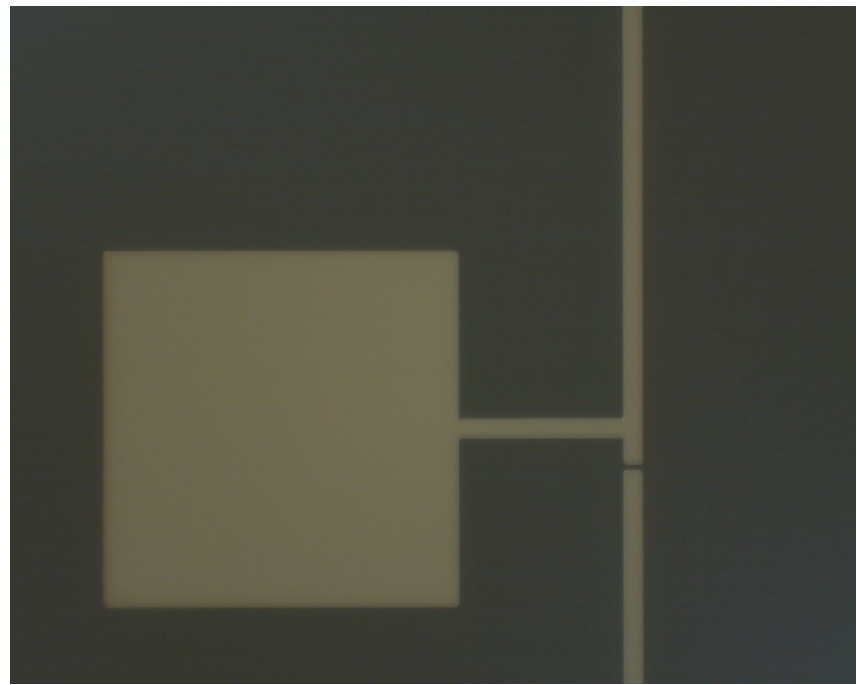
(b) Au waveguide roughness measurement: ~0.75nm on average (as shown in Ra)



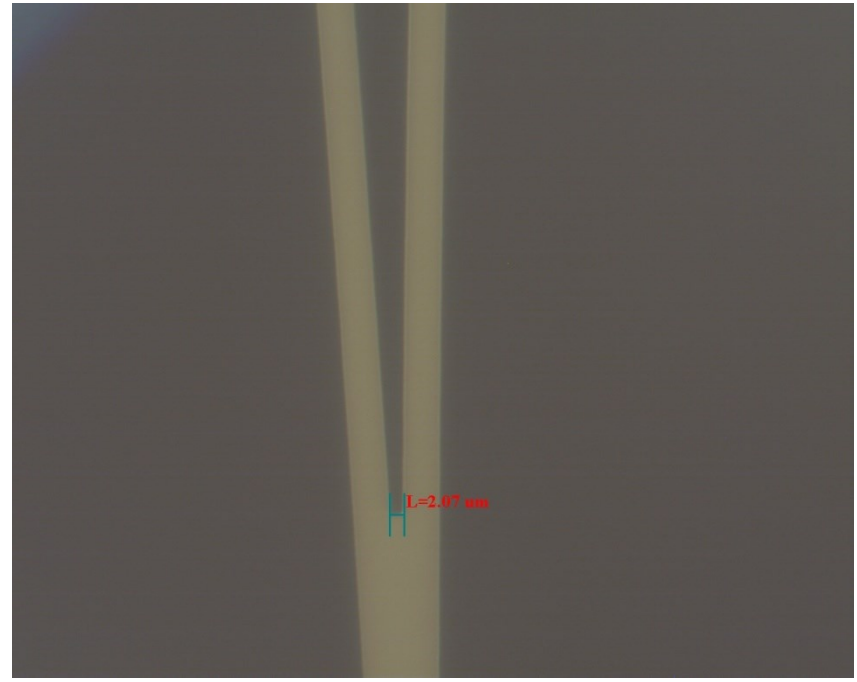
(a)



(b)



(c)



(d)

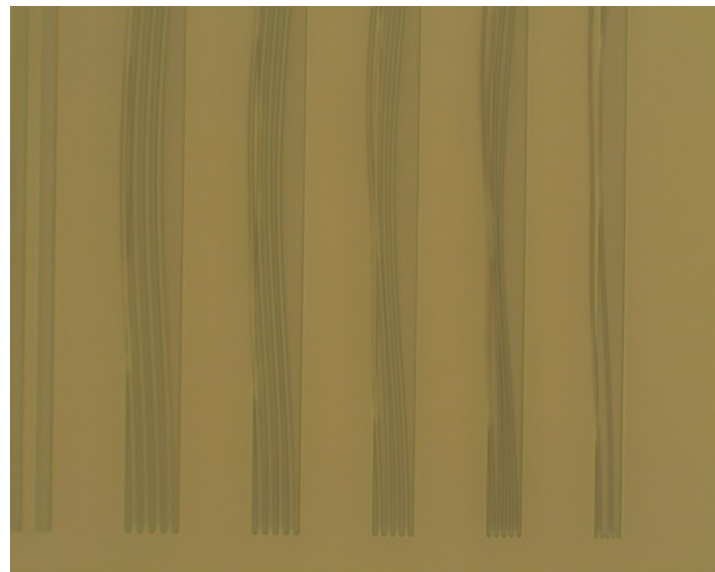
Figure 3.5 Microscope images of Au waveguide after lift-off process.

(a) single waveguide image (b) triple waveguide image (c) T-junction image (d) V-crotch image.

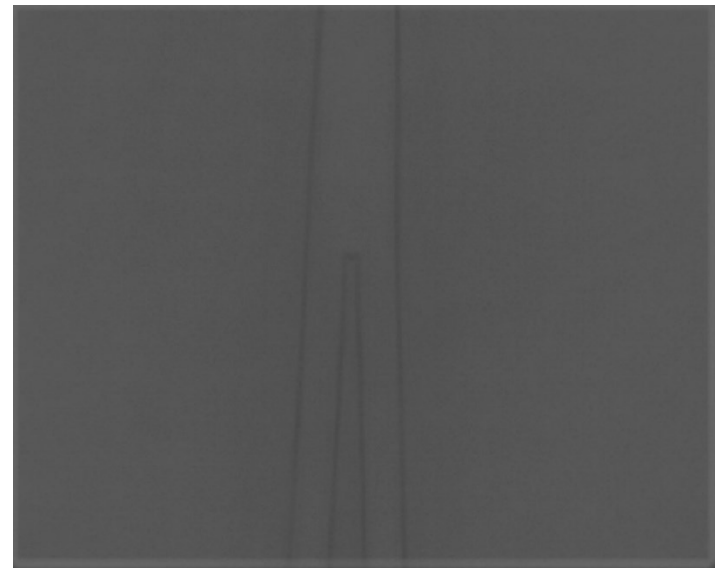
3.3.3 Issues and Discussions on the Process

It should be noted that the bi-layer lithography process and metallization process were adopted from the previous research [44]. The issues causing waveguide pattern failure arose at the bi-layer lithography process. Three factors determine the resolution of the bi-layer lithography: prebake of LOR-1A including baking time and temperature, exposure dose and developing time. As mentioned in section 3.3.1, LOR-1A soft-baked at 180°C for 3 minutes was etched at the rate of approximately 3nm/s in MF-321. In a previous test, lowering soft-bake temperature to 80°C and extending baking time to 1.5 hours were tried at the same time. This was done to maintain the baking temperature below the glass transition temperature (T_g) of CYTOP, which is 108°C, but to largely evaporate the solvent of LOR-1A. The resolution of developed features was tremendously reduced as shown in Figure 3.6(a) due to a uncontrollably faster etch rate of LOR-1A if it is baked at temperature lower than 170°C [49]. Exposure dose is another critical parameter to precisely define the dimension of Au waveguides, especially that of triple waveguides. The intuitive way to determine over-exposure is by inspecting the end point or the junction of the straight waveguides to see if they are square or round. Over-exposure could lead to a round edge at the end of the junction of waveguides as shown in Figure 3.6(b). A longer than 1 minute developing in MF-321 etched more LOR-1A than expected, and this caused waveguide patterns, especially triple waveguides, to collapse due to insufficient LOR-1A for supporting S1805 as shown in Figure 3.6(c). This leads to a significant decrease in waveguide resolution. In our laboratory, MF-321 was sometimes reused, and it degraded after several uses. In order to avoid over-developing of bi-layer features, the wafer was first inspected under the microscope to check the resolution of waveguides after a 50 second

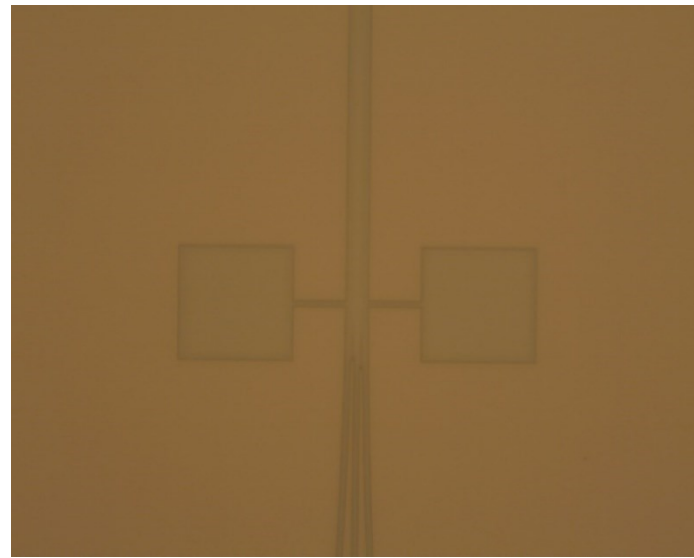
developing period, and inspection was repeated in 5 second developing steps until the required resolution of waveguides was achieved. The results can be affected by several factors such as room temperature and humidity, stability of equipment and expiration of material in use. Optimum parameters for bi-layer lithography must be monitored and adapted to varying processing conditions.



(a)



(b)



(c)

Figure 3.6 Undesirable lithography results

- (a) photoresist S1805 strips overlapped due to a uncontrollable fast etch rate of under-baked LOR-1A;**
- (b) round junction due to overexposure; (c) triple waveguides collapsed due to over development.**

3.4 Etch Stop Layer Patterning

3.4.1 Purpose of Introducing Etch Stop Layer

After Au waveguides were patterned on the surface of the lower CYTOP layer, the next step was depositing a thin SiO₂ film on top and patterning this film to protect areas that were etched through to open fluidic channels in the final step. This SiO₂ layer is a sacrificial layer without any bio-sensing function and it will be removed at the end of the process. The aim of the etch stop layer is to improve the accuracy and uniformity of the channel depth across the wafer. The optimum channel depth should be etched until the Au waveguides are fully exposed and no further etching should be allowed into the lower CYTOP layer. As shown in Figure 3.7(a), since the SiO₂ layer is not susceptible to O₂ plasma etching, the entire CYTOP above will be removed and then etching will be stopped at the SiO₂ layer. In the previous processes [40] [41] [42] [43] [44] with no etch stop layer, channel etching became complicated and time consuming. Channels were created by iteratively etching the wafer and adjusting the running time of the etcher, measuring the depth of the channel after each etching operation until Au waveguides were shown to be fully exposed. This approach makes it impossible to stop the etching on the 35nm Au waveguide. A CYTOP pedestal was inevitably formed below the Au waveguides by over-etching in order to ensure the entire Au waveguides were fully exposed as shown in Figure 3.7(b). The new process enables etching of uniform fluidic channels without pedestals, achieved across the whole wafer after the SiO₂ layer is removed, as shown in Figure 3.8. It was also found that the etching depth was not the same across different areas of the wafer due to etching rate non-uniformity caused by a non-uniform O₂ plasma. With the protection of the SiO₂ layer, the wafer can be over-etched, while the channel depth remains precise

and uniform across the whole wafer. In addition, the etch stop layer acts to protect the Au waveguides from being affected by subsequent process steps.

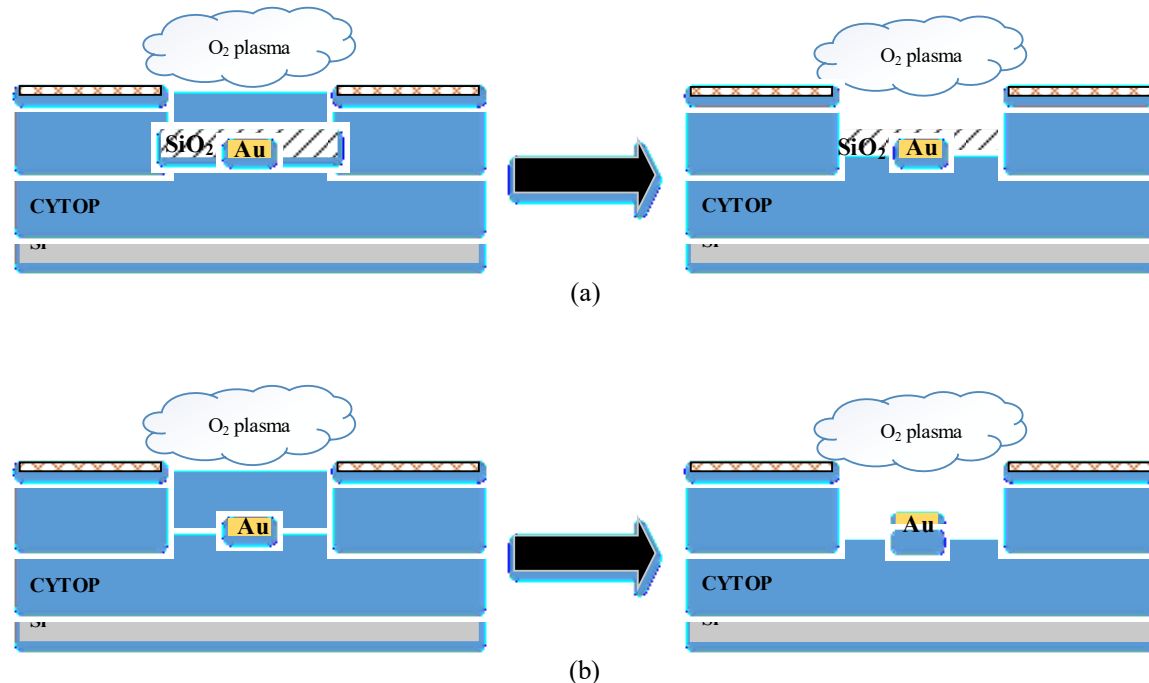


Figure 3.7 Illustrations of channel etching by O₂ plasma

(a) channel etching with SiO₂ etch stop layer (b) channel etching without SiO₂ etch stop layer

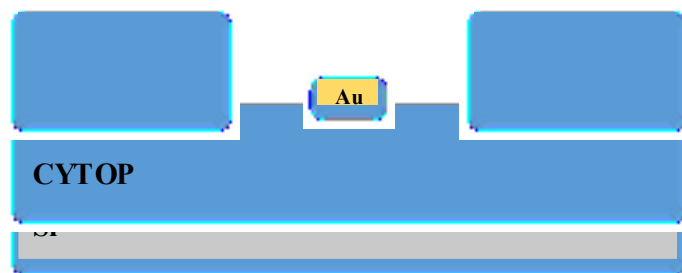
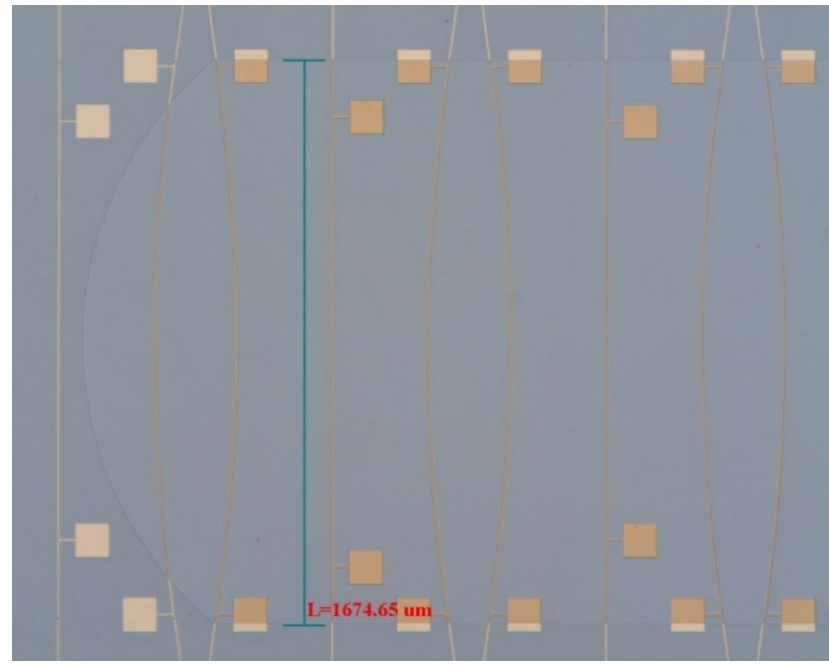


Figure 3.8 The profile of the etched channel after removal of etch stop layer

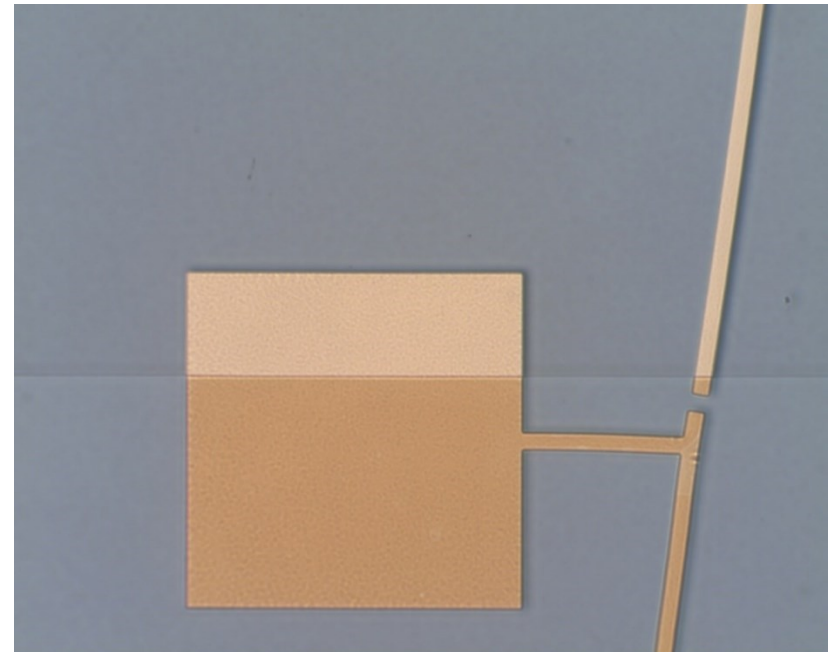
3.4.2 Process of Etch Stop Layer Patterning

Bi-layer lithography and SiO₂ E-beam evaporation combined with lift-off process were applied in sequence to pattern the SiO₂ etch stop layer as described in Table IV. These steps were completed with process parameters similar to those used for patterning Au waveguides, with some modifications at the baking step in order to avoid SiO₂ deformation. The equipment used in the process is the same as that used in Au waveguides patterning process. At the beginning of the process, a layer of LOR-1A was spin-coated at the spread speed of 1000rpm for 10 seconds followed by a spin at 4000rpm for 30 seconds and then it was soft-baked at 80°C for 1.5 hours. It is worth noting that it is necessary to ramp the wafer from room temperature to 80°C when heating, and ramp the wafer down to room temperature when cooling instead of putting the wafer directly on or off of a hotplate. This aims to prevent Au waveguides from deformation resulting from rapid temperature changes. Next, a layer of S1805 was spin-coated by the same spin speed and spin time as those of LOR-1A and it was soft-baked at 80°C for 1 hour with ramping up and down in a process similar to that used for the LOR-1A. After the preparation of the bi-layer, a dose of 117mJ/cm² at H-line was used to expose S1805 with the fluidic channel mask. The chosen dose is larger than that used to pattern Au waveguides discussed in section 3.3.1. This is because an over-exposure is expected to mitigate problems due to the potential misalignment in the channel alignment lithography, as will be discussed in section 3.6. The channel mask feature was imprinted into the LOR-1A and S1805 stack after a 50 second developing in MF-321.

After developing, a 75nm thick SiO₂ film was deposited by E-beam evaporation at the rate 1Å/s and tooling factor 175. The thickness of the film is twice that of Au film to ensure the etch stop layer is thick enough to effectively stop etching by the O₂ plasma. It is worth noting that the tooling factor used for SiO₂ deposition is the same as that used for Au deposition. Although it had been proved that the tooling factor 175 could work for an accurate deposition of Au, the thickness for SiO₂ deposition would be inaccurate by using the same tooling factor. The oscillation frequency of QCM will be affected by the material deposited on it. Since the mass of SiO₂ deposited on QCM is smaller than that of Au given the same depositing time, the frequency of the QCM will increase consequently, which results in a thicker SiO₂ film in the end. Different from Au waveguides, the roughness and thickness of SiO₂ film is not critical since it is not involved in sensing function but is a temporary layer that will be removed in the end. Therefore, no measurement of deposited SiO₂ film roughness and thickness was taken. Then, the wafer was immersed in remover PG for 30 minutes at 60°C to liftoff the bi-layer structure together with SiO₂, leaving the patterned etch stop layer. Figure 3.9 show some images captured by microscope after the SiO₂ etch stop layer was patterned. In contrast with the Au waveguides, there are no strict dimension and roughness requirements for the etch stop layer. A good assessment of the etch stop layer is the clear and distinguishable shape under microscope inspection.



(a)



(b)

Figure 3.9 Microscope images captured after etch stop layer process

Images show SiO₂ layer is covering on the top of the wafer. (a) 5X magnification of image showing SiO₂ layer in light field; (b) 50X magnification of image indicating the boundary of SiO₂ layer (lower side is SiO₂ layer).

Table IV Etch Stop Layer Fabrication Process

Step	Description	Details
1	LOR-1A spin coating	Spread at 1000rpm for 10 seconds; Spin at 4000rpm for 30 seconds.
2	Prebake on a hotplate	Ramp up to 80°C, hold for 90 minutes, ramp down to RT.
3	S1805 spin coating	Spread at 1000rpm for 10 seconds; Spin at 4000rpm for 30 seconds.
4	Prebake on a hotplate	Ramp up to 80°C, hold for 60 minutes, ramp down to RT.
5	Exposure	H-line Dose: 117mJ/cm ²
6	Developing	Developer: MF-321 Developing time: 50 seconds Developing temperature: Room temperature
7	SiO ₂ deposition	SiO ₂ thickness: 70nm Deposition rate: 1Å/s Tooling factor: 175
8	Liftoff	15 minutes in remover PG at 60°C; Ultrasonic action for 10 seconds; Repeat above steps until the bi-layer residue is removed.

3.4.3 Issues and Solutions in the Process

One concern is the temperature involved in this process. Unlike the bi-layer lithography for patterning Au waveguides that involves baking LOR-1A and S1805 at 180°C and 115°C respectively, baking at temperature above T_g to pattern the bi-layer feature for the etch stop layer was forbidden and could lead to Au waveguides deformation due to the difference in thermal expansion coefficient (TEC) between CYTOP and Au. Figure 3.10 shows a profilometer measurement of Au pad sitting next to waveguides on the CYTOP cladding after being baked at 180°C. It is observed that Au pad is raised by thermal expansion variation between CYTOP and Au. To avoid the deformation of Au waveguides, the temperature involved in the process must be lower than T_g . Another aspect is that an abrupt temperature change leads to failure of the SiO₂ thin film, making the film delaminate and fold, leading to a feature imprinted on the underlying CYTOP layer as shown in Figure 3.11. To avoid these problems in the current and following steps involving baking, the wafer must be slowly ramped to the desired temperature below T_g and slowly ramped down to room temperature letting both CYTOP and SiO₂ change in volume slowly. Although there is a resolution loss of bi-layer lithography due to a faster etch rate of LOR-1A baked at lower temperature, it is still acceptable as the resolution achieved by the modifications meets the requirement of 80μm critical dimension of channels. Figure 3.12 shows the result of this modified process.

Apart from the thermal issue, another issue occurred related to the patterning of the SiO₂ film. There are two methods to pattern the etch stop layers: wet etching and liftoff. For the wet etching method, a thin film of SiO₂ is first deposited, covered with photoresist and

patterned, then exposed SiO₂ is removed by buffered oxide etch (BOE). For the lift-off method, photoresist is first patterned into the desired features, and then SiO₂ is deposited over top, after which photoresist is removed taking with it unwanted materials. Both methods were tested on witness samples and the better method was verified based on the process performance. It was found that liftoff was preferred for patterning the SiO₂ layer. The reason is that thin SiO₂ film deposited by E-beam evaporation can be easily peeled off during buffered oxide etch (BOE) wet etching procedure and make features entirely unshaped as shown in Figure 3.13. This might be explained by the quality of SiO₂ film deposited by E-beam evaporation, which is quite low density and cannot stand the flush of chemical solution during wet etching. Although a denser SiO₂ layer can be deposited by means of LPCVD, the temperature of LPCVD is at least 150°C to 250°C, which is beyond T_g. CYTOP will undergo a transition to a soft and flexible state at this temperature, causing Au waveguides to deform. Given the patterning failure associated with the wet etching process, the SiO₂ etch stop layer is patterned by bi-layer lithography and liftoff process to increase the feature resolution.

In our trial, Al was once considered as an etch stop layer material as well as SiO₂ since it is resistant to O₂ plasma etching and easy to be patterned by alkaline based solution. Unfortunately the Al layer was unsuccessful as the surface was damaged as shown in Figure 3.14, which occurred during the upper CYTOP baking process where the temperature reached 100°C. This might be caused by the fact that the shape of Al is highly sensitive to high temperature due to its large TEC ($2.3 \times 10^{-5} \text{K}^{-1}$). Through many trials, it was found that the temperature cannot exceed 80°C otherwise the Al film will deform.



Figure 3.10 Profilometer measurement of an Au waveguide and an Au pad
The wafer was heated at 180°C for 3 minutes

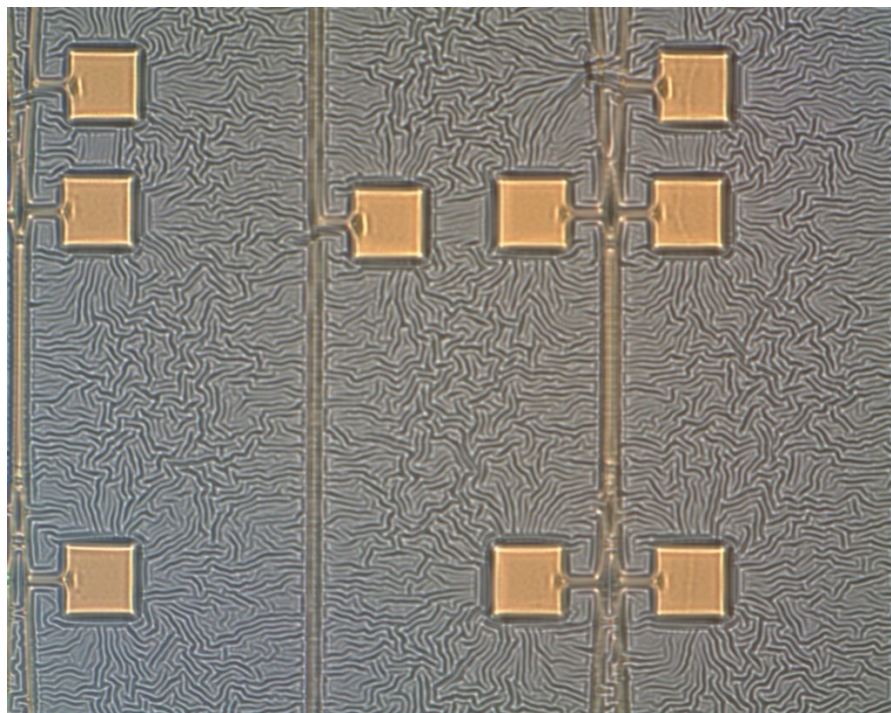
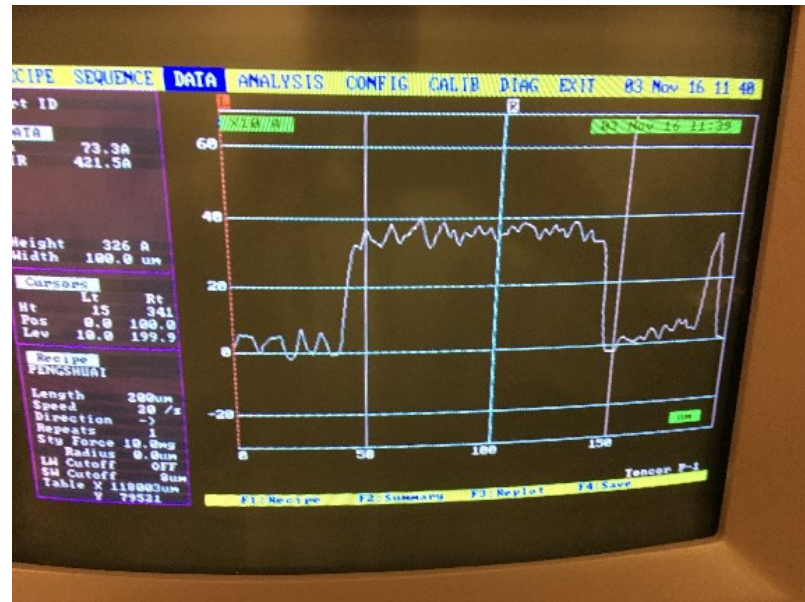
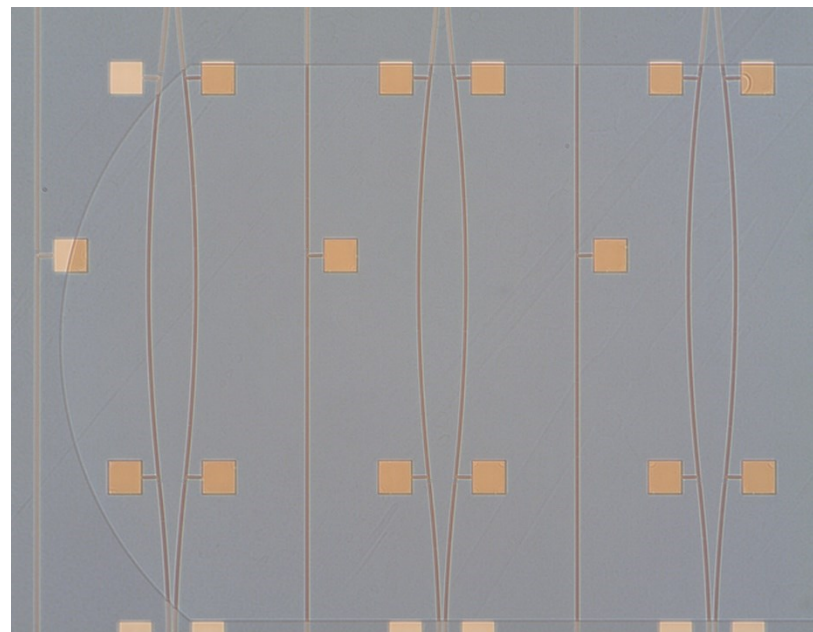


Figure 3.11 Microscope image of SiO₂ being twisted at sudden thermal change



(a)



(b)

Figure 3.12 Results obtained by modified baking step

(a) profilometer measurement of Au waveguide and Au Pad (b) Microscope image of Channel

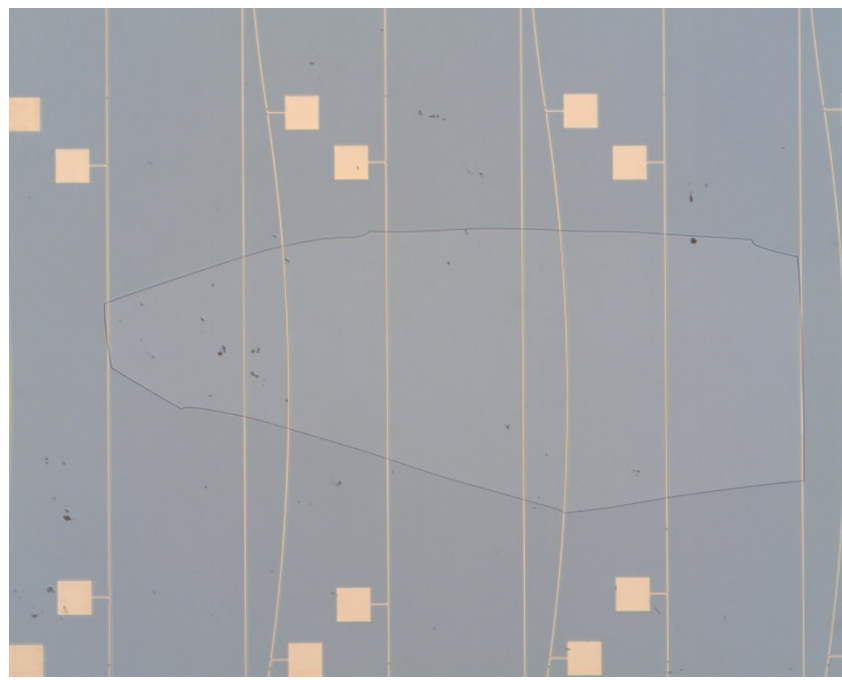


Figure 3.13 Microscope image of shattered SiO_2 pattern

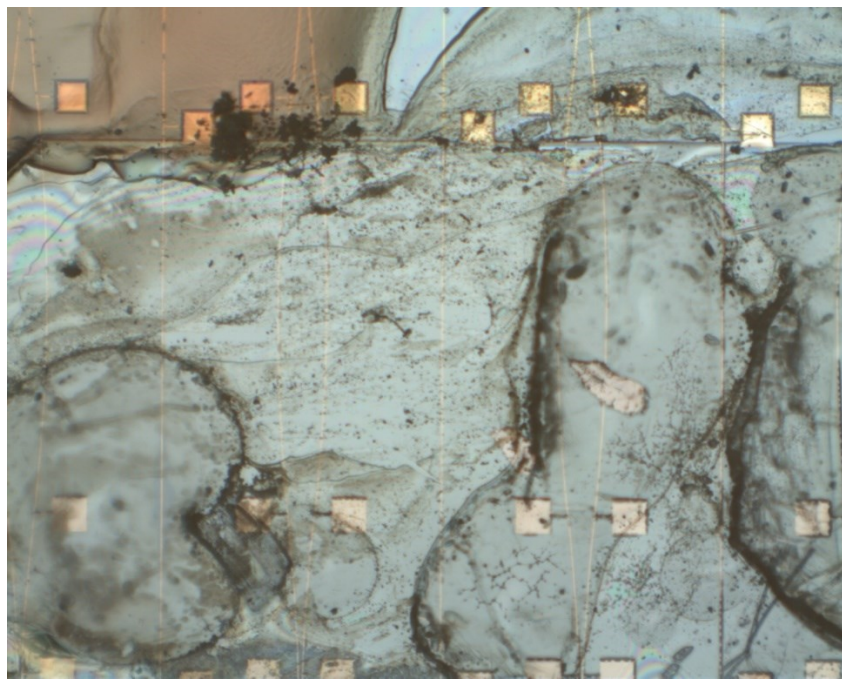


Figure 3.14 Microscope image of Al etch stop layer after heating above 100°C

3.5 Top CYTOP Cladding

3.5.1 Top Cladding Process

The top CYTOP cladding was applied to the wafer after the etch stop layer was patterned. The thickness of cladding must be more than $8\mu\text{m}$ to support the LRSPP mode. The top CYTOP cladding process was more complicated than lower CYTOP cladding for several reasons. First, cured CYTOP is susceptible to solvent penetration which means when top cladding layers are coated, the solvent will diffuse to lower cladding and accumulate below. When the wafer is soft-baked, the evaporation of solvent could burst and damage the Au waveguides. Second, baking CYTOP above T_g will cause deformation of Au waveguides. If CYTOP is heated above T_g , CYTOP will change into a rubbery and fluid state and thin Au waveguides will experience deformation since the TEC of Au ($1.4\times10^{-5}\text{K}^{-1}$) is smaller than that of CYTOP ($7.4\times10^{-5}\text{K}^{-1}$). In this situation, the temperature of baking top CYTOP cladding cannot exceed T_g , which means CYTOP cannot be fully cured and some solvent will remain in the body of the CYTOP cladding. The issues involved in this step have been discussed in detail and a solution was discussed in [41] [42] [43] [44]. The process outlined here was adopted from the previous work above and specific details will not be elaborated in this thesis. The steps were described in Table V. Figure 3.15 show microscope image of this process. The main idea to successfully coat top CYTOP cladding is spinning a super thin layer each time in order to reduce solvent volume and baking at 100°C to let solvent evaporate slowly.

Table V Upper CYTOP Cladding Fabrication Process

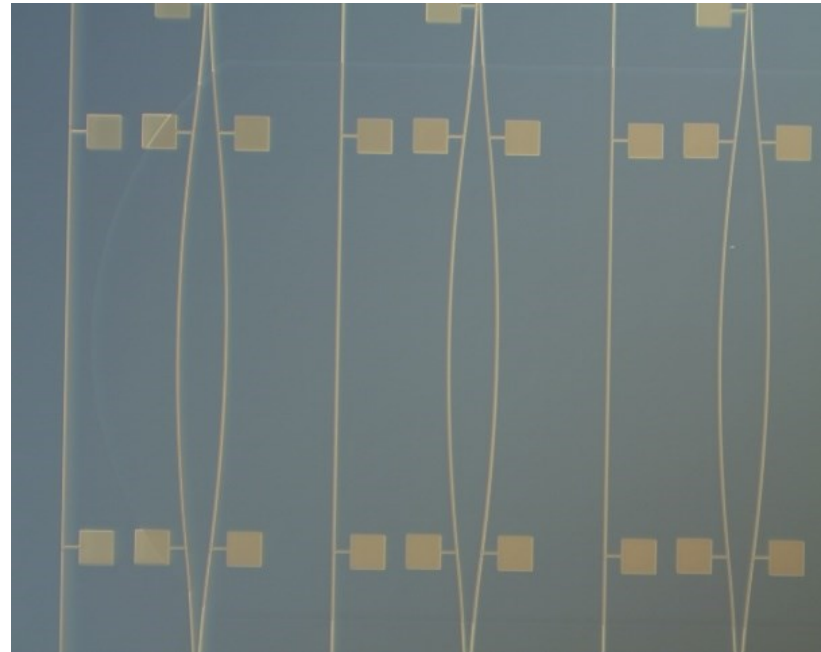
Step	Description	Details
1	Spin coat 9% CTX-809A CYTOP	550rpm for 10s to spread, followed by 3000rpm for 30s.
2	Soft-bake on a hotplate (1 st layer)	Bake at 50°C for 30 minutes; Ramp up to 100°C at 5°C/hr, then hold for 4 hours.
	Soft-bake on a hotplate (2 nd to 6 th)	Bake at 50°C for 30 minutes; Ramp up to 100°C at 25°C/hr, then hold for 4 hours.
3	Repeat steps 1 and 2	Three spins achieve more than 9µm thick layer.



(a)



(b)



(c)

Figure 3.15 Microscope images captured after upper CYTOP cladding process

(a) and (b) 50X magnification of images with Nomarski filter. The gap in the straight waveguide is to provide electrical isolation between waveguide segments [51]. **(c) 5X magnification of images with Nomarski filter.** The waveguides with a split and recombination structure is Mach-Zehnder Interferometer [52]. It is seen that waveguides are intact and preserved from being deformed.

3.5.2 Issues in the Previous Work

A critical issue in this process that remained unsolved following previous work [44] was that severe cracking happened after the first layer of top cladding was coated. This leads to a zero chip yield as mentioned in section 3.2. According to this work, the lower CYTOP cladding was constructed by a layer of M-grade material as an adhesion layer on the silicon substrate, followed by 3 layers of S-grade as dielectric medium and 1 layer of M-grade on top. Since S-grade has poor adhesion to Au, a layer of M-grade material was included to enhance adhesion to Au waveguides. However, severe cracking was found consistently after the first layer of S-grade top layer was coated and the cracking propagated downward to the lower cladding damaging the Au waveguides. Annealing above T_g , was investigated, however the cracking could not be removed. A potential solution comes from an experiment in which CYTOP solvent was dispensed onto the fully cured lower cladding containing S-grade and a thin layer of M-grade on top. This two type CYTOP combination was adopted in the work [44] and severe cracking was observed on the surface. However, when the same solvent was dispensed on the surface of exclusive S-grade stack baked at 200°C (this was the original way that built up CYTOP cladding in the work [40] [41] [42] [43]), no cracking was seen. It appeared that M-grade CYTOP is not stable on S-grade with a 200°C bake and we assume the possible reason is that large residual stress could build up inside the multi-grade stack while the CYTOP was baked at 200°C and this stress is beyond the CYTOP yield strength which is 40MPa [46].

3.5.3 CYTOP Stress Measurement

A stress measurement of CYTOP layer was performed using the Film Stress Measurement (FSM) tool to evaluate the influence of the stress resulting from the baking steps of CYTOP multilayers. During the test, two layers of CYTOP were spin-coated and fully cured by using the steps described in section 3.2. The inner stress of the two layer CYTOP was then measured. Then CYTOP solvent was dropped directly on the surface of the CYTOP to observe if any cracking issues arose. Four combinations of CYTOP stack which are 9% S-grade + 9% S-grade, 9% M-grade + 9% M-grade, 9% A-grade + 9% A-grade, 9% S-grade + 9% M-grade were tested in order to get a comprehensive evaluation about film stress of CYTOP combinations in the real multilayer coating application. Each combination was tested on two wafers in order to make the result more persuasive. The results are shown in Table VI and it can be seen that none are beyond the yield strength (40MPa).

Table VI CYTOP Stress Measurement Results

CYTOP Combination	Wafer ID	Stress (MPa)
9%A + 9%A	Sample 1	14.12
	Sample 2	17.16
9%M + 9%M	Sample 3	20.29
	Sample 4	27.18
9%S + 9%S	Sample 5	23.63
	Sample 6	26.03
9%S + 9%M	Sample 7	11.59
	Sample 8	13.93

Figure 3.16 (a) ~ (d) show microscope images of these four types of CYTOP combination. From the figures, it is shown that no cracking issues were found on the surface of CYTOP of same type stack or multiple type stack. The results are reasonable since the stress of all CYTOP combinations is less than its yield strength, making crack formation unlikely. However, the stress that is obtained during the baking steps is still large. This renders the CYTOP susceptible to cracking issues later in the process since the stress can easily build up and exceed the CYTOP yield strength by adding more CYTOP or conducting long baking repetitively. The cracking issues involved in [44] were believed to be caused by larger stress from multiple types of CYTOP stacking each other as mentioned in the section 3.5.2. The results shown indicate that stress could not be over the yield strength by combining different types of CYTOP directly. Other factors need to be considered such as concentration of CYTOP. In general, cracking issues await further studies.



(a)



(b)



(c)



(d)

Figure 3.16 Microscope image of CYTOP combination surface

(a) 9%A +9%A CYTOP combination; (b) 9%M +9%M CYTOP combination; (c) 9%S +9%S CYTOP combination; (d) 9%S +9%M CYTOP combination. From the images, all show no cracking

3.6 Fluidic Channel Patterning

Fluidic channels were defined and etched after the CYTOP cladding was complete. The channels expose the gold waveguides and allow for subsequent functionalization for bio-sensing applications. To define the fluidic channel feature, a modified channel lithography with Al hard mask was adopted to solve the cracking issues from photoresist SPR-220 (Dow) discussed in [43]. To etch fluidic channels, a RIE system using an O₂ plasma was used to provide anisotropic etching of CYTOP. With the help of the etch stop layer, the etching step is simpler and more efficient compared to the etching work discussed in [40] [41] [42] [43] [44].

3.6.1 Issues in the Previous Work

In the previous work [40] [41] [42] [43] [44], photoresist SPR-220 was chosen to be the channel etching mask. The ability to coat more than 10μm thickness in a single-coat process makes it suitable for masking during O₂ plasma CYTOP etching. However, when this type of thick photoresist was deposited, it was susceptible to cracks during the baking steps described in the work above. The reason might be that an inner stress was built up in the thick photoresist film during an improper baking step. Notably, these cracks were imprinted into the underlying CYTOP cladding during the etching process. Cracking in the photoresist and CYTOP cladding has been observed in [43]. Another issue with SPR-220 is that its baking temperature is 115°C, which is higher than T_g of CYTOP and can cause deformation of Au waveguides inside the CYTOP cladding due to their TEC variation.

3.6.2 Purpose of Al Etching Mask Lithography

By introducing an Al etch mask technique to replace SPR-220, a crack-free etching mask can be realized so that CYTOP cladding underneath will be clean and intact during O₂ plasma etching. Al film is naturally resistant to plasma etching and easily patterned at 80°C, making it a good choice for etching mask.

3.6.3 Process of Al Etching Mask Lithography

The first step was depositing 20nm Al on top of the wafer by E-beam evaporation with a tooling factor and etch rate being 175 and 1Å/s respectively. As aluminum is acting as a mask layer, its roughness is not critical and its thickness should be enough to shield the O₂ plasma from etching the covered CYTOP. As discussed in 3.4.2, the tooling factor used for Al deposition is the same as that used for Au deposition. The actual thickness for Al deposition would be thicker than the indication from the monitor by using the same tooling factor. Since the mass of Al deposited on QCM is smaller than that of Au given the same depositing time, the frequency of the QCM will increase consequently, which results in a thicker Al film in the end. In a test, 20nm was qualified for protecting the CYTOP underneath from etching. Next, a layer of HMDS was coated on the Al film with a spin speed of 4000rpm for 30 seconds followed by soft-bake at 80°C for 45 minutes. The function of HMDS was to improve the adhesion between Al and photoresist above. Then, a layer of S1805 was spin-coated next to the HMDS layer with a same spin speed of 4000rpm for 30 seconds followed by a soft-bake at 80°C for 1 hour. It is necessary to note that instead of placing the wafer directly onto the hotplate at 80°C, ramping from room temperature to 80°C with a moderate rate of 100°C/hour must be taken during soft-baking

HMDS and S1805. It is also imperative to ramp down from 80°C to room temperature before taking the wafer off the hotplate. This is due to the thin Al film's sensitivity to rapid thermal change that leads to Al deformation as discussed in section 3.4.3. Figure 3.17 shows Al deformation due to fast ramping on a hotplate. After the preparation with photoresist, the wafer was exposed by fluidic channel mask alignment with the etch stop layer pattern at a dose of 98mJ/cm². This step requires careful manipulation since aluminum is not transparent, making accurate alignment challenging. To develop the photoresist and Al, the wafer was immersed in MF-321 for approximately 3 minutes. This is an advantage of using Al for the etching mask as Al and S1805 can both be developed by MF-321 and therefore no other chemical solution was necessary. The process steps are listed in Table VII. Figure 3.18 shows a channels lithography profile with optimum resolution after S1805 and Al were developed.

Table VII Al Etching Mask Lithography Process

Step	Description	Details
1	Depositing Al by E-beam	SiO ₂ thickness: 20nm Deposition rate: 1Å/s; Tooling factor: 175
2	HMDS spin coating	Spread at 1000 rpm for 10 seconds, Spin at 4000 rpm for 30 seconds.
3	Prebake	Ramp up to 80°C at 100°C/hour, hold for 45 minutes, ramp down to RT.
4	S1805 spin coating	Spin at 4000 rpm for 30 seconds;
5	Prebake	Ramp up to 80°C at 100°C/hour, hold for 60 minutes, ramp down to RT.
6	Exposure	H-line Dose: 98mJ/cm ² .
7	Developing	Developer: MF-321; Developing time: 3 minutes; Developing temperature: Room temperature.

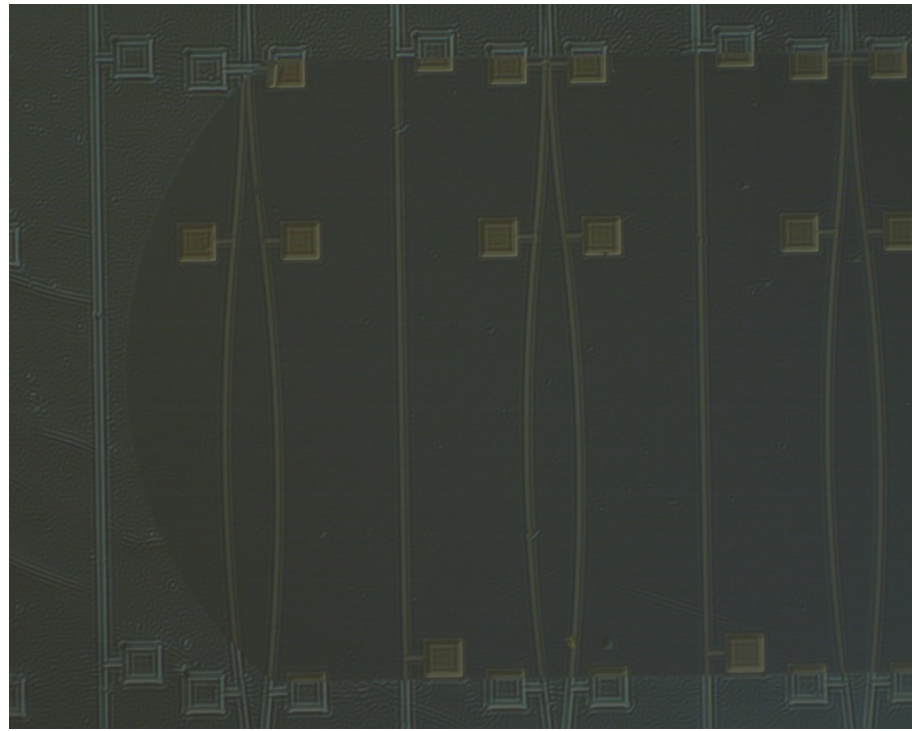


Figure 3.17 Microscope image of Al mask deformation

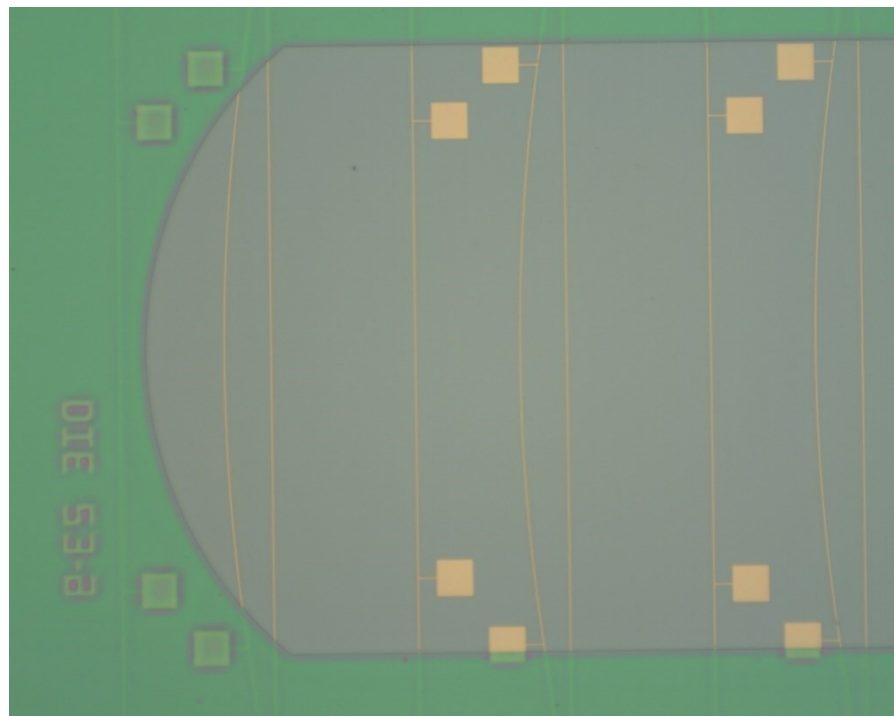


Figure 3.18 Microscope image after Al mask developing

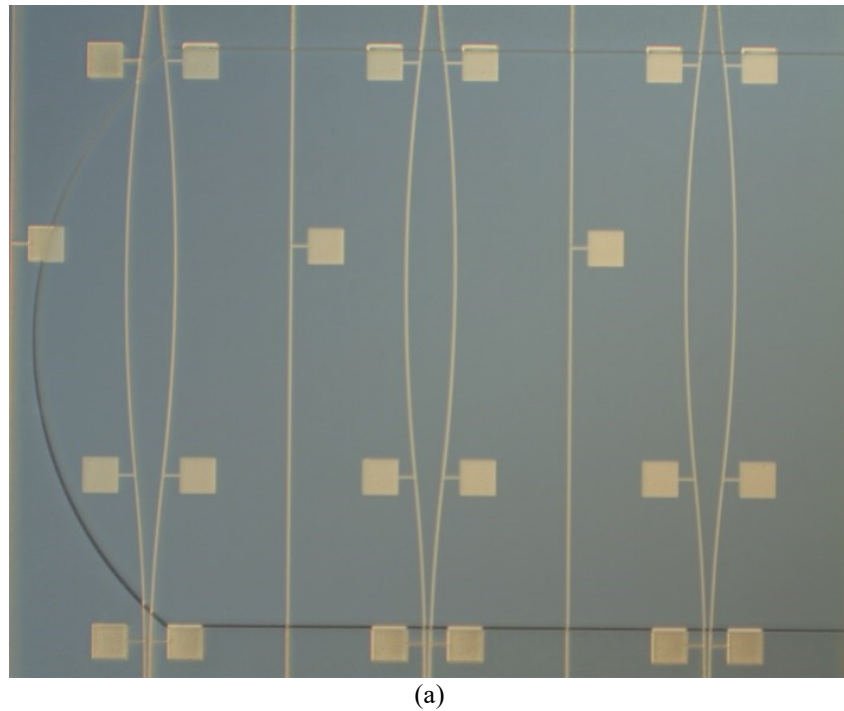
3.6.4 Channel Etching Process and Results Evaluation

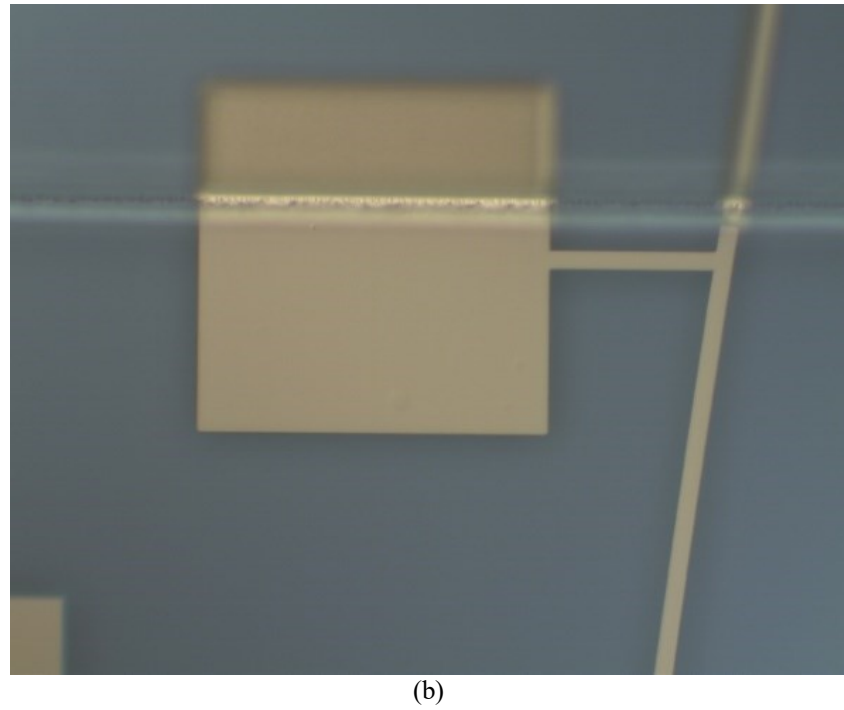
The final step in this fabrication was creating fluidic channels to deliver the test solution to the exposed Au waveguides. This was achieved by O₂ plasma RIE etching the CYTOP through the Al mask. RIE also provided an anisotropic etch such that the channel sidewall maintains a perpendicular profile to the surface. With the etch stop layer in place, there was no etching time limit in case of over-etch. In this work, three runs of 5 minutes, each followed by etch depth measurement, were required to get the entire channel etched. The etching system condition was set as: power: 200W, O₂ pressure: 430mTorr, O₂ flow rate: 60sccm. Table VIII lists the etching depth measurement made by profilometer after each 5 minutes of plasma etching. From the table, we can see O₂ plasma etching was stopped by the etch stop layer within 15 minutes of the third etching and no over-etch was shown. Since the exact time of channel etching to simply expose the Au waveguides without etching extra CYTOP is not required under the protection of the etch stop layer, a rough estimation of 15 minutes was considered as the time required to fully etch the channel without any additional O₂ consumption.

Table VIII Channel Etching Depth Measurement

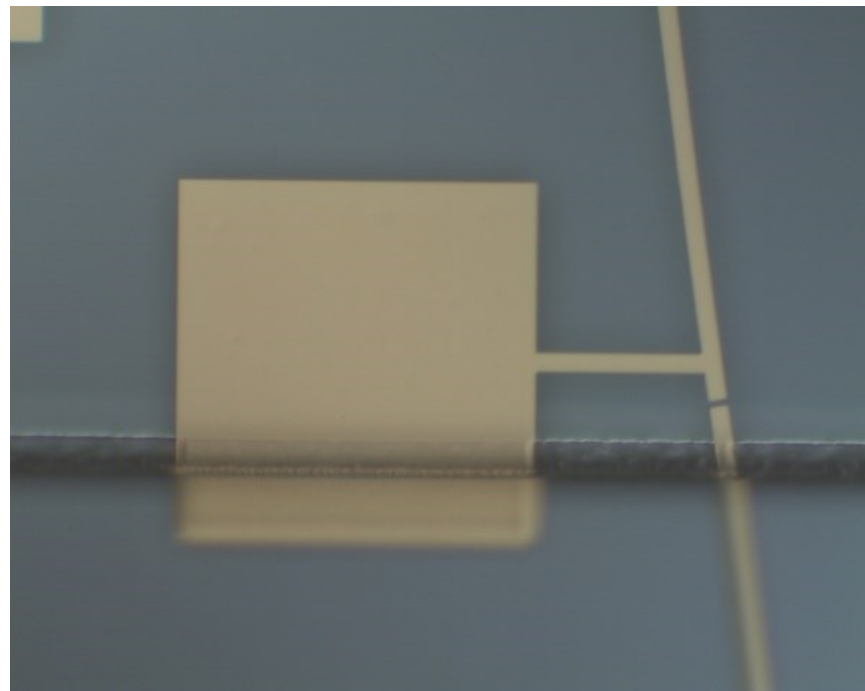
Time	Etching depth			
	Wafer-1	Wafer -2	Wafer-3	Wafer-4
5 minutes	6.27 μm	6.27 μm	5.55 μm	6.56 μm
10 minutes	11.61 μm	12.41 μm	11.28 μm	12.82 μm
15 minutes	13.6 μm	13.72 μm	13.5 μm	13.54 μm

After channel etching was finished, the wafer was immersed in MF321 for 3 minutes to remove the Al mask. It was next immersed in buffered oxide etch (BOE) to remove the SiO₂ etch stop layer, and finally it was dipped in 1165 (MicroChem) at 60°C for 30 minutes to clean any photoresist residue and particles. Figure 3.19(a) ~ (c) shows the image after channels have been etched with Al and SiO₂ removal. It should be pointed out that the edge of the fluidic channels was misaligned due to the challenge of aligning a wafer covered by a thin Al layer with a photo-mask. A substitution of SiO₂ as channel mask was considered to solve the misalignment issue caused by the opaqueness of Al. However, the patterning of SiO₂ by using BOE to wet etch photoresist-patterned SiO₂ was unsuccessful. The SiO₂ layer was completely etched away. The reason might be from the fact that SiO₂ wet etching is isotropic and the SiO₂ layer is only 70nm thin. The layer was etched vertically and horizontally at the same time during etching, leading to the whole layer etched away.





(b)



(c)

Figure 3.19 Microscope images after channel etching and etch stop layer removal

(a) 5X magnification of image showing channel profile; (b) 50X magnification of image showing the upper boundary of a channel; (c) 50X magnification of image showing the lower boundary of a channel. The edge of the channel is rough because of lithography misalignment.

The wafer was then put into the vacuum oven for 7 days baking at 90°C to drive out the solvent residual in the top CYTOP cladding. After this, the wafer was coated with dicing mask: SPR-220 and baked for 30 minutes at 80°C prior to dicing. The wafer was diced by a dicing saw spinning at a high speed. The dicing mask acts as a protective layer for exposed waveguides and prevents damage during dicing. Without the dicing mask, the waveguides in channels could be contaminated and destroyed by the wafer debris coming from the dicing process. Once the wafer had been diced into chips, those chips needed to be cleaned before further quality check and optical measurements were done. The method used to clean these chips is: first immerse the chip in a hexane solution and apply ultrasonic vibration for 5 minutes to clean out any contamination residuals from the facets. This solution will not strip the SPR-220 covering the top surface of the chip, which can protect the waveguides from being destroyed during an ultrasonic bath. Second, chips were placed into acetone and IPA for 10 minutes each to remove the SPR-220 photoresist. Next, the chips were cleaned in DI water and dried by a high purity N₂ blow. Then the chips were selected for AFM measurement of thickness and roughness of Au waveguides, and CYTOP roughness in the channel. Finally the channel depth was measured by the profilometer.

The AFM scans illustrate the thickness and roughness of an Au waveguide from one random selected chip as shown in Figure 3.20 and Figure 3.21. From Figure 3.20, it is shown that the average roughness of the Au waveguide is approximately 1nm, which is in the acceptable range. From Figure 3.21, it is shown that the thickness of the Au waveguide is approximately 35nm which is the desired thickness. This also indicates that the etch stop layer works to function as a barrier from CYTOP being over-etched by O₂ plasma etching

since there is no over-etch found under the Au waveguide. The Figure 3.22 shows that the average roughness of the CYTOP in the channel measured by AFM is approximately 0.6nm. This is a promising improvement compared to the previous work [42] in which the roughness of CYTOP in the channel was reported approximately 40nm. The reason is that the etch stop layer covers the channel, thereby preventing the O₂ plasma etching from roughing the CYTOP surface. The channel depth was measured by profilometer as shown in Figure 3.23. The measurement gives a depth of 13μm indicating that 7 layers of CYTOP at 3000rpm contribute enough thick CYTOP for upper cladding.

The comparison of results gained by the process in this thesis and previous process [42] has been listed in Table IX showing the improved qualification by the process. There are two issues found in the image, captured by scanning electron microscope (SEM), as shown in Figure 3.24. The first is that there is a trench along the edge of channel. This is caused by the misalignment during the channel mask lithography which leads to the non-coverage of the edge of channels by SiO₂ layer, making it vulnerable to O₂ plasma etching. The second is that the side wall of the etched channel is rough, which could cause the sample solution deposition in the bio-sensing test application. The reason could be the improper parameter settlement of the etching tool and is still being investigated. These two issues remain to be solved in future research. The facets of the diced chips were observed under microscope as shown in Figure 3.25. It is shown that a clear straight waveguide interface is embedded in the clad of CYTOP.

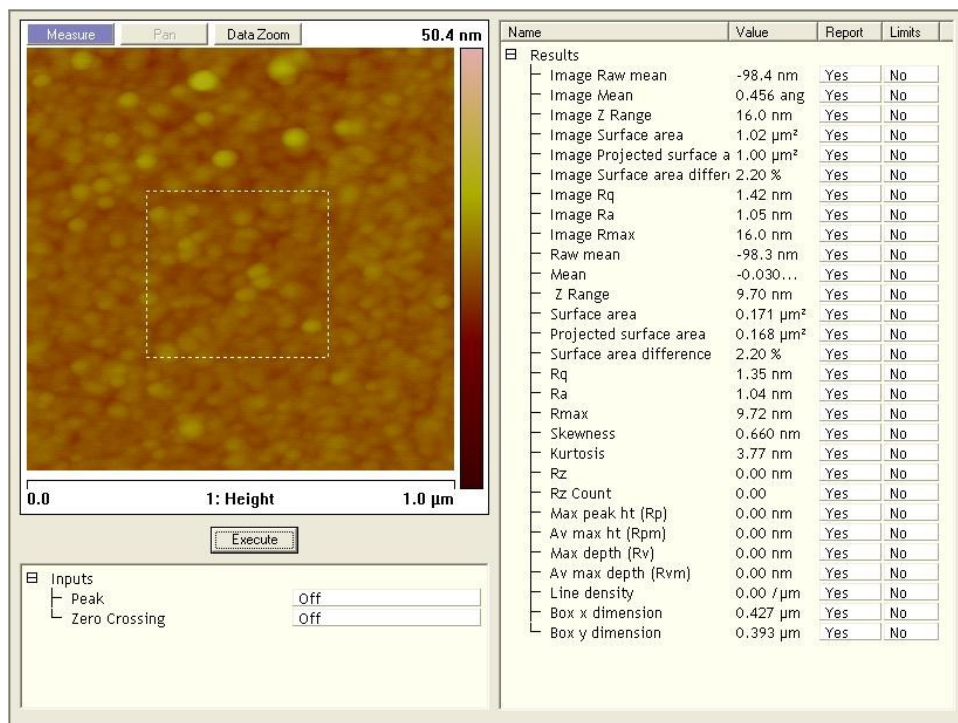


Figure 3.20 The AFM scanning results of one Au waveguide.

The average roughness of the Au waveguide is indicated by the “Ra” value, and the RMS value for the roughness of the Au waveguide is indicated by the “Rq” value.

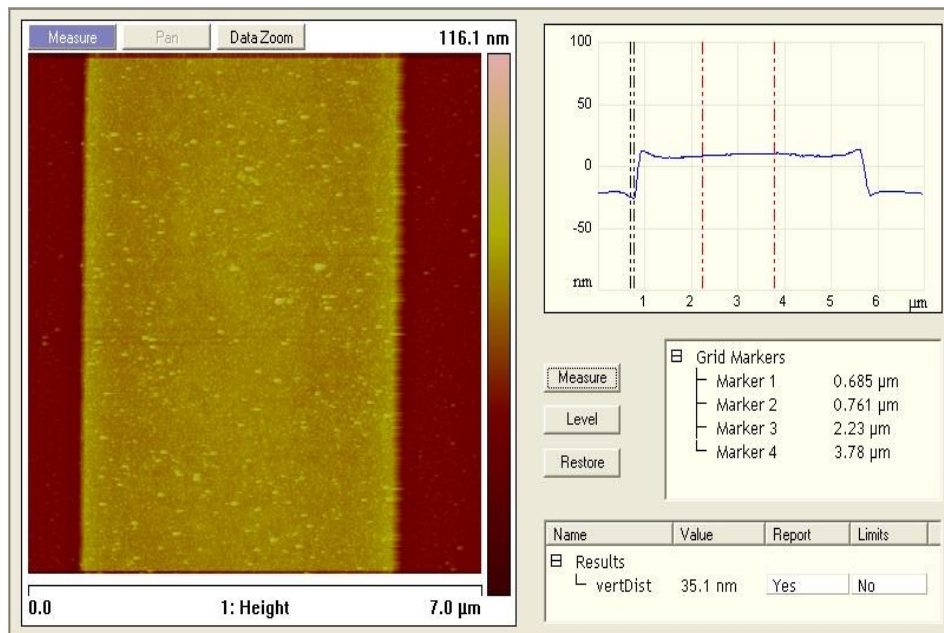


Figure 3.21 The thickness measurement of one Au waveguide by AFM.

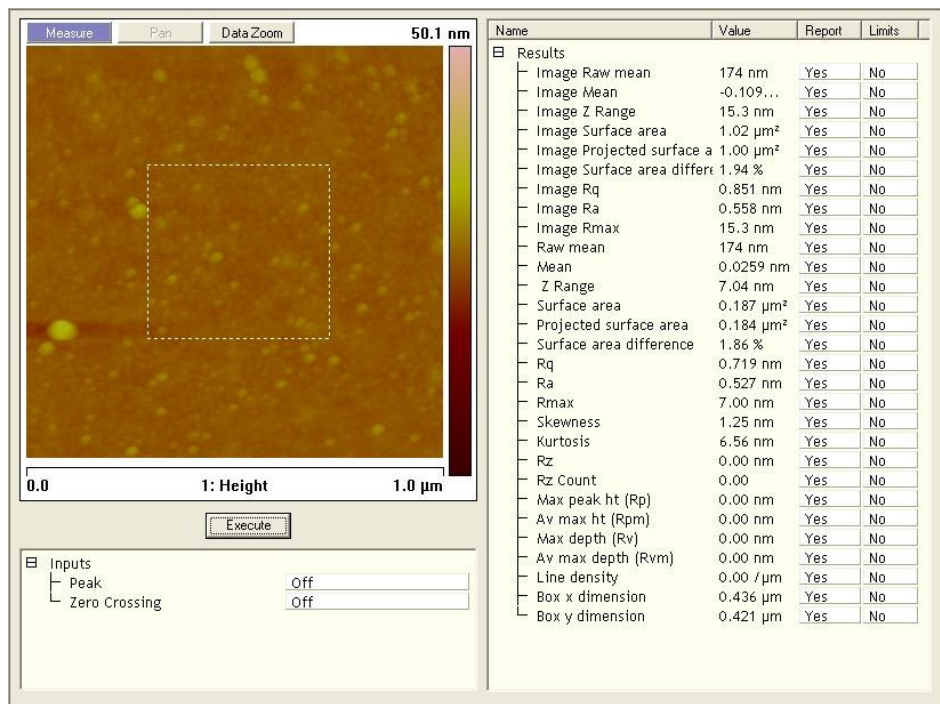


Figure 3.22 The AFM scanning results of CYTOP in a channel

The average roughness of the CYTOP is indicated by the “Ra” value, and the RMS value for the roughness of the CYTOP is indicated by the “Rq” value.

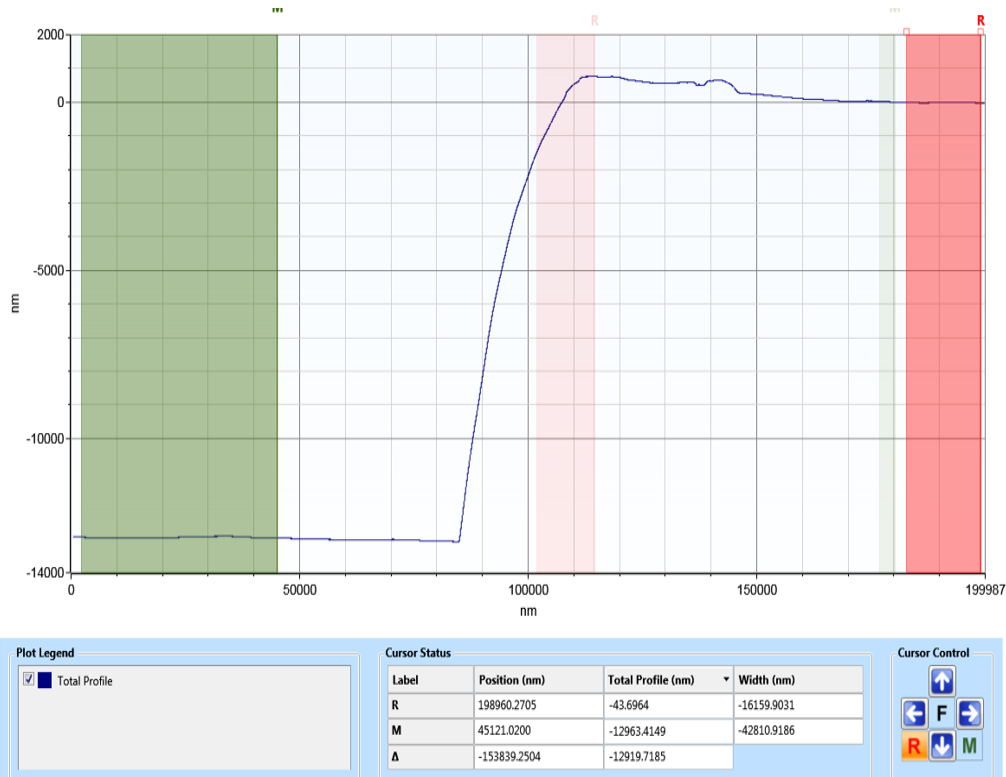


Figure 3.23 The depth of a channel measured from the right edge by profilometer Dektak

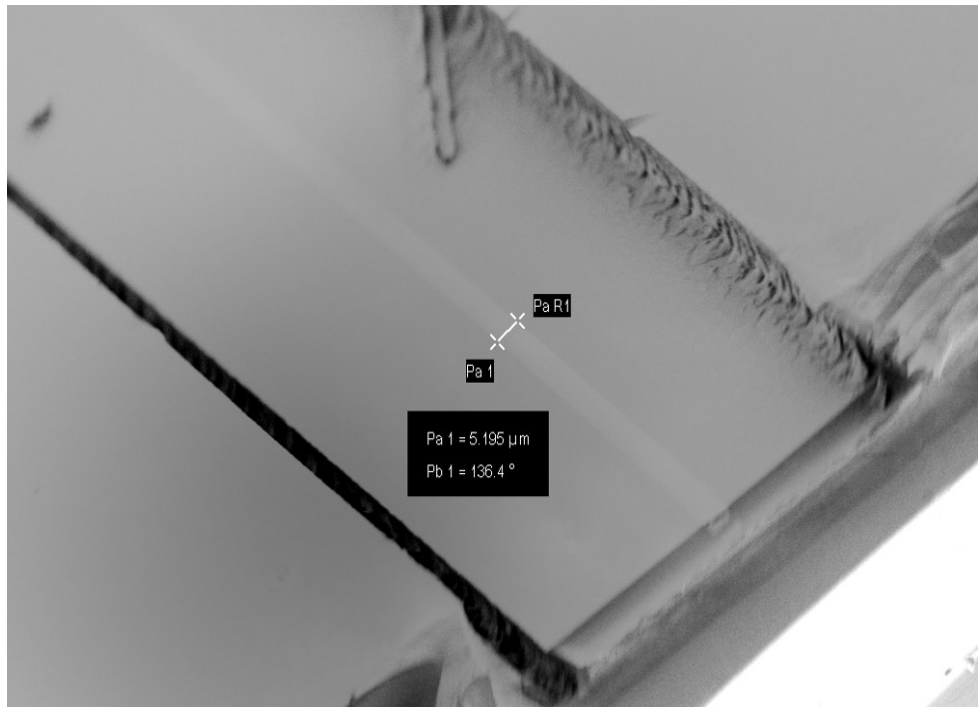


Figure 3.24 The SEM image of the cleaved channel

P_a 1 indicates the width of the waveguide showing around 5 μm , **P_b1** means the chips was titled by 136.4° while inspection



Figure 3.25 The Microscope image of the chip facets showing a waveguide cross-section

Table IX The Process Qualification Comparison

Measurement result	Process in the thesis	Process from [42]
Au waveguide roughness	1 nm average	5 nm average
Waveguide over-etch	No	Above100nm over-etch in average
CYTOP roughness	0.5 nm average	18 ~ 40 nm average

3.7 Optical measurements and discussion

The device fabricated in this thesis was optically tested by measuring the power output of waveguides using the assembled fluidic system as shown in Figure 3.26. The measurement was conducted by Alex Krupin from University of Ottawa. The system consists of a Plexiglas fluidic jig with two holes. This allows biotesting fluid to flow in and out, and an O-ring matched in the dimensions to the channels to seal the channel, which prevents the liquid from leaking out. An Al metal base is used to support the chip during the biosensing step. The input fiber used for the LRSPP excitation is a polarization-maintaining (PM) fiber with a core diameter of $7\mu\text{m}$. An optical signal of 1310nm in wavelength was provided by the light source, a laser diode, and carried by the input PM optical fiber to the system. The system was positioned on two multi-axis positioning stages to align the fiber to the waveguide. A $25\times$ objective lens that defines the optical axis of the output portion of the setup was permanently fixed to the table to magnify and collimate the optical output coming from the device under test. The background light was removed by an aperture and the output beam was split into two portions: one was sent to an infrared camera to visually monitor the testing procedure and observe changes in output during an experiment; the other was captured by a power meter and analyzed by Labview for data acquisition. The fluid for test was supplied by a syringe pump through Pico tubing that connected to the fluidic holes of the Plexiglas jig. The complete setup is pictured in Figure 3.27.

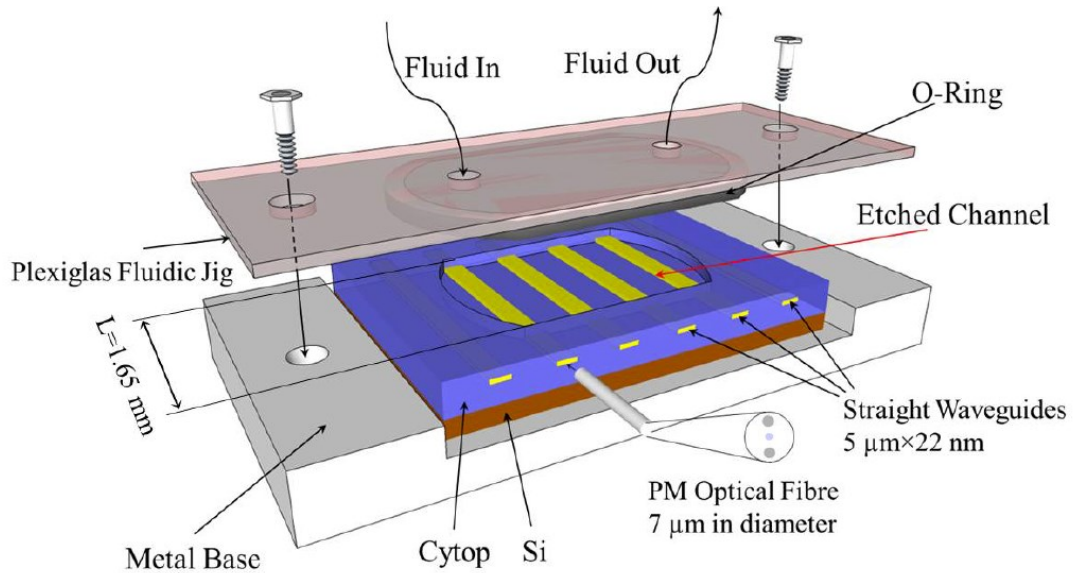


Figure 3.26 Assembled testing fluidic settlement

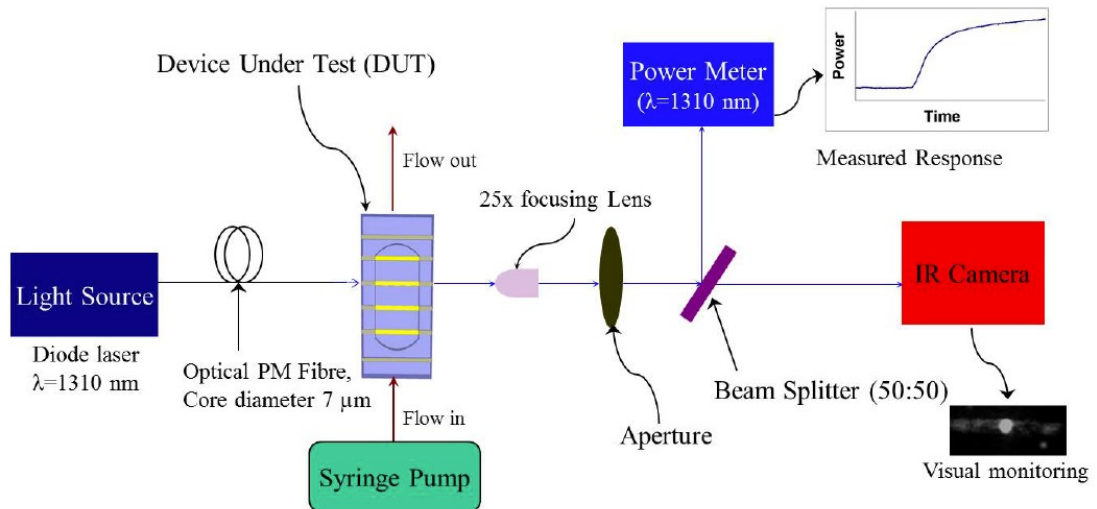


Figure 3.27 Biosensing test system setup

In the cutback experiment, LRSPPs were excited on the waveguide that were fully embedded in the CYTOP by the light source of 1310nm in wavelength. The attenuation, which is power lost per unit length of the waveguide (dB/mm), was determined by measuring the total power output of the fully cladded waveguide and subtracting the input power. The measurement was taken by using the photodetector. No phase sensitive detection or modulation was used in our measurement of straight waveguides. Three sizes of chips based on chips length: 3.2mm, 3.5mm and 4.8mm were tested in order to obtain the cutback curve. Figure 3.28 shows the mode image of the LRSPPs obtained from the device. The cutback curve is shown as Figure 3.29. From the image, a function was generated from the curve, the slope of which yields the attenuation in 5.03dB/mm while the y-axis intercept yields the total coupling losses which is subsequently divided by 2 giving the couple loss per facet in 3.3dB. The value of the attenuation yields lower than the theoretical model predicted which is approximately 7dB/mm [39]. This is presumably due to the rough facet or remaining CYTOP solvent in the upper cladding layer.

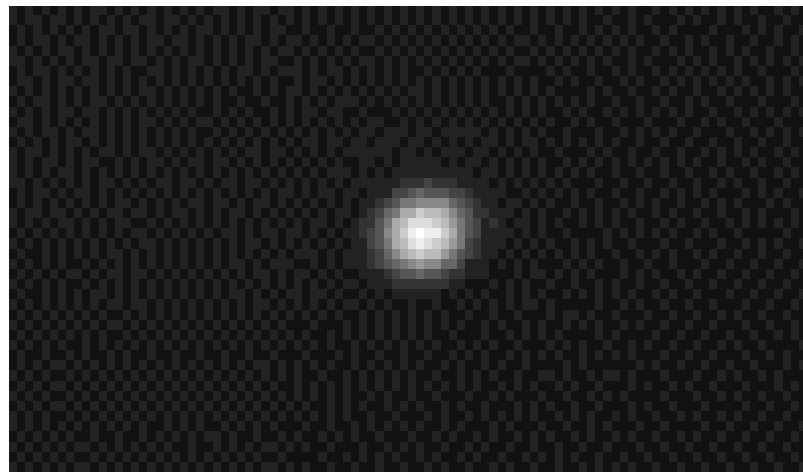


Figure 3.28 Mode image of the LRSPPs excited from the device.

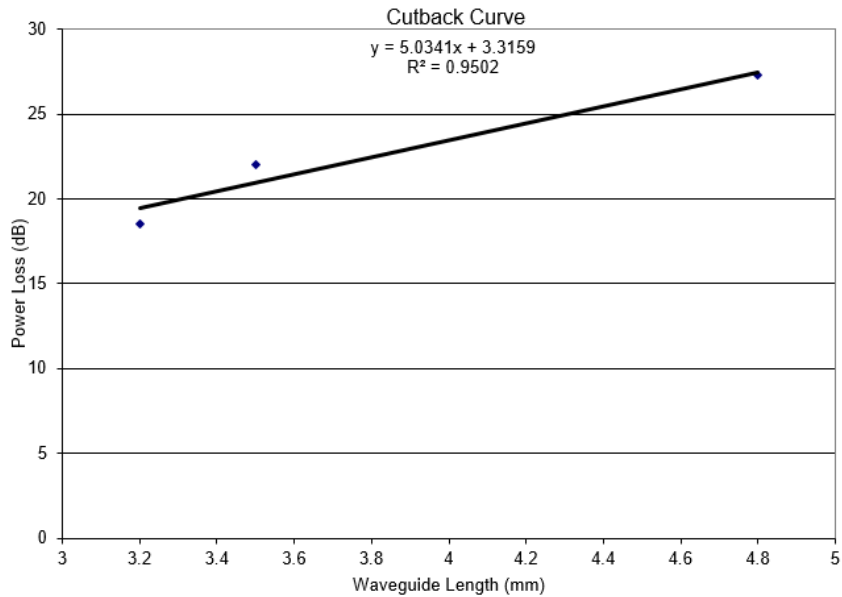


Figure 3.29 Cutback curve obtained from the device

After the cutback testing experiment, another two tests were executed (measurements were completed by Alex Krupin, University of Ottawa) to verify biosensing capability of the devices. The first one is detection of Bovine Serum Albumin (BSA), a protein of 2~4nm in size that can bind on the surface of Au. BSA has a strong non-specific absorption to metals such as Au. It can form a monolayer in approximate 2nm thickness without needs of functionalizing Au waveguides. In this experiment, A UV light was shed on the waveguides before the chip was assembled to the system, to clean the Au waveguides surface from any contaminates for a better absorption. The experiment starts with the injection of a mixed buffer solution of phosphate buffered saline (PBS) and glycerol (Gly) into the flow channels at a flow rate of 20 μ l/min in the first 10 minutes. PBS is a biologically compatible fluid and Gly is used for modifying the refractive index of the solution. The concentration of Gly is precisely controlled to receive a PBS/Gly solution with the refractive index of 1.338 that closely matches that of CYTOP A-grade. Next a

combination of PBS/Gly and BSA was injected into the flow channel at a flow rate of 20 μ l/min for the next 10 minutes. The concentration of BSA in PBS/Gly solution is 1mg/ml in this case. In the final 10 minutes, PBS/Gly solution was re-introduced into the flow channel to flush out extra BSA from the channel, leaving only a monolayer of BSA on the Au waveguide. In this experiment, it took 10 minutes in each step to establish a baseline trend. Figure 3.30 shows a sensing result of the experiment. From the diagrams, it is seen that a baseline is established when PBS/Gly solution was introduced in the device at the beginning. A shift in the output power can be observed as the BSA and PBS/Gly mixture was injected in the channel. As the pure PBS/Gly solution was re-injected into the channel, a monolayer of BSA on Au waveguides was removed and output power was increased due to the decrease in the concentration of BSA. The change in output power due to a monolayer of BSA on the Au waveguide is approximately 0.10dB obtained from the result and this response is consistent with other devices when working with the same CYTOP-matching buffers. It is worth noting that there is signal noise in each step baseline. This noise is believed to be caused only by the mechanical matter, such as stages and screws of the testing system. It is approximately 2~3 times larger than the inherent noise of the optical fiber, laser and laser controller in the system. Currently more sufficient way is waiting to be found to reduce this noise. Although a sensitive biosensing work can be achieved merely under the appearance of the noise, its accuracy can be affected by the drifts going up and down with time in each step, which should be flat in theory, as shown in Figure 3.30. It is observed that the drifts appear when the jig is screwed on the top of the upper CYTOP, which is not fully cured, to seal the channel, making top CYTOP start to compress and to press on the waveguide underneath. It also lead to waveguides deformation or break. Those

drifts are particularly found in the chips that have a gold thickness less than 30nm while the chips with a thicker gold such as 35nm show a less drifting issue.

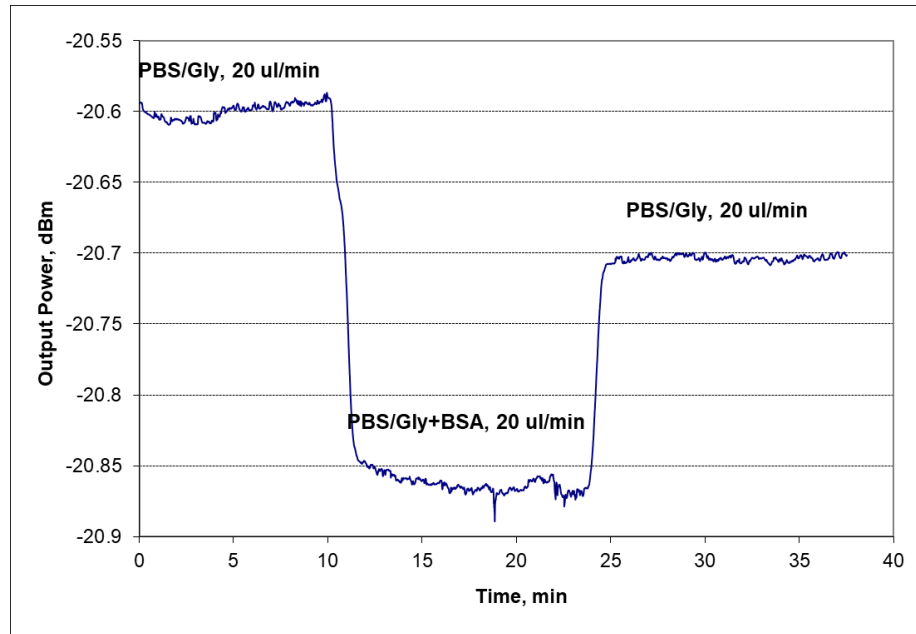


Figure 3.30 BSA detection results obtained from the device

Another experiment is the bulk solution sensitivity test. PBS/Gly was used as the testing solution. By precisely controlling the concentration of Gly, mixture solutions with different refractive index: 1.334, 1.336, 1.338, 1.340, and 1.342 can be obtained. The experiment started with injecting PBS/Gly solution with refractive index of 1.334 for 6 minutes. After 6 minutes, PBS/Gly solutions, with refractive index increased by 0.002, were injected every 6 minutes. The output mode images were captured by camera and output power data was recorded by Labview. Figure 3.31 shows the result of the whole experiment. From the diagrams, it is observed that the output power starts to increase as the refractive index of the solution increases to 1.336 and then continues to decrease as the refractive index of the solution enlarge beyond 1.336. The peak of the power indicates the refractive index

matches that of CYTOP, meaning the refractive index of the CYTOP A-grade is between 1.336 and 1.338. It can also be noted that there is an obvious jump between 1.338 and 1.340 indicating that the sensitivity of the biosensing bulk test is much higher and the device is sensitive to bulk as expected. It is also worth noting that there was strong background interference that could affect the accuracy of the biosensing test results. The reasons causing this issue might be similar to those experienced in the BSA detection experiment: poor facet interface, unetched SiO₂ layer and soft-baked CYTOP with solvent residue.

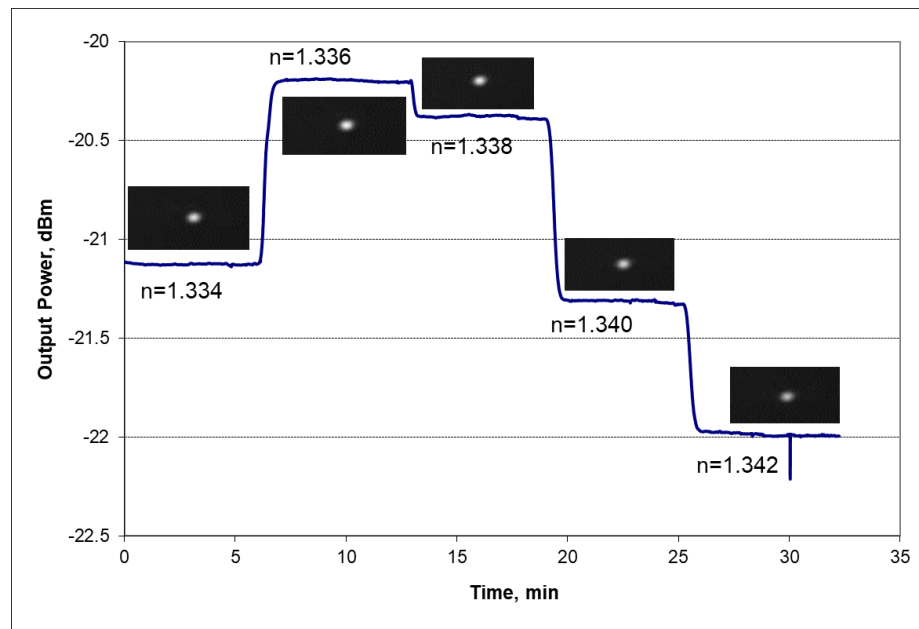


Figure 3.31 Bulk sensing test results from the device

4 Chapter: Glass Lid Seal by CYTOP Bonding

This chapter describes the bonding process between glass wafer and silicon wafer that enables a glass lid to cover and seal channels of the device. The purpose of the glass lid on the channels is to isolate them from being in contact with the outside environment and to avoid contamination of the biochemical sample and formation of bubbles, which can be generated by using the current test setup and lead to incorrect signal output. The complete device with a glass lid can be integrated with other components to fulfill a complete system. In the work [53] [54] [55] [56] [57], different kinds of polymer bonding were discussed in detail to achieve a successful polymer bonding structure. Prior to this thesis research, no bonding work on the level of product wafer which contains Au waveguides has been realized. The bonding work on the level of test wafers which merely have channels on the substrate has been done to develop the bonding process. All steps involving bonding process are in the development stage and thus no final process recipe can be concluded. This chapter will describe the trial bonding work that has been completed on 4 dummy wafers. The step details will be elaborated upon and results will be illustrated and discussed with microscope figures.

4.1 Bonding trial 1

The first bonding trial is bonding an unpatterned glass wafer to a patterned silicon wafer. The silicon substrate was coated with 3 layers of CYTOP A-grade by the steps given in section 3.2. These layers of CYTOP were baked at 200°C to ensure the solvent can be fully evaporated. Next, the silicon wafer was patterned with the fluidic channel mask by RIE etching protected by the Al mask. The glass wafer was coated with 1 layer of CYTOP A-

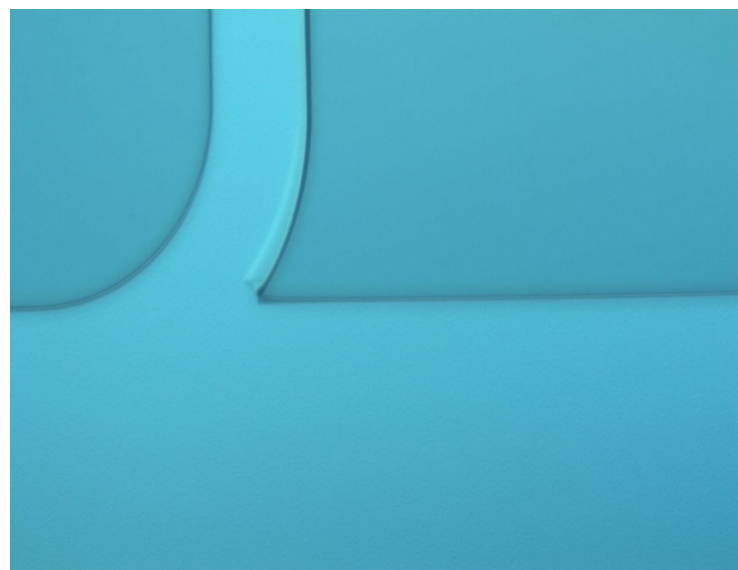
grade without any patterning on it. The glass wafer and silicon wafer were cleaned by acetone and IPA, and then rinsed by DI water and dried by N₂ blow. These steps were done to make both wafer surfaces clean to eliminate related effects that could lead to a bonding failure. After cleaning the wafers, both wafers were loaded in the chamber of the bonding machine known as AML. The silicon wafer was put on the lower platen which can be controlled to move in x-y direction and to rotate in clockwise or counterclockwise by a motor. The glass wafer was fixed on the upper platen by a spring clamp without any possibility to move. After both wafers were loaded into the chamber, the chamber was purged with N₂ to clean the entire bonding environment and wafers. Next the chamber was vacuumed to lower pressure in the order of 10⁻⁵ mbar, and the wafers were then slowly put into contact and a force of 2kN was applied before starting to heat both wafers. Both wafers were ramped up to 120°C at a rate of 5°C/min. The sequence that applying force first and then heating is believed to be important and cannot be switched over. The theory behind this is to use the thermal expansion of CYTOP during heating both wafer in contact to help CYTOP migrating into each other for a strong bond. The bonding was performed for more than 10 hours with the force and temperature turned on. The detailed steps are listed in Table X.

Table X The Bonding Process of the First Trial

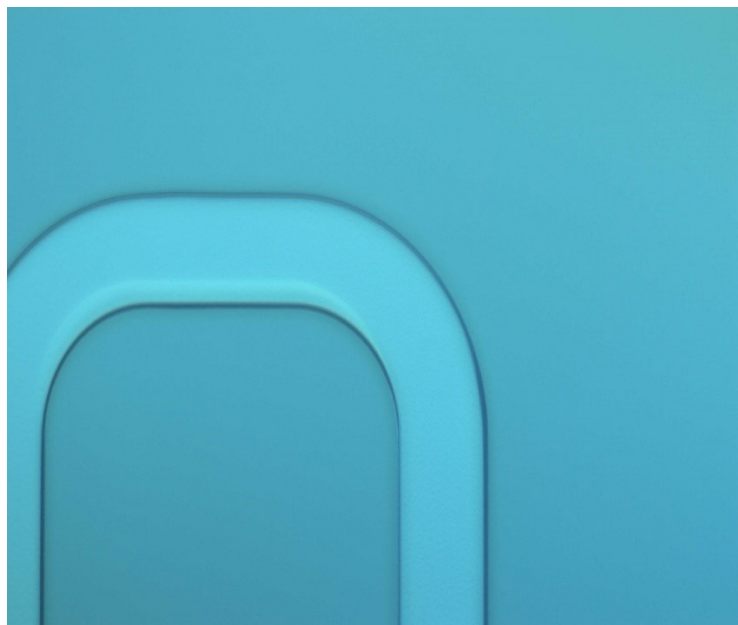
Step	Description	Details
1	Chamber Purging	This is automatically controlled by machine to clean the chamber of the machine.
2	Chamber vacuum	The chamber is vacuumed to 10^{-5} mbar before bonding.
3	Force application	2kN is applied manually; Pressure: 0.25MPa.
4	Controlled Heat Addition	Lower platen temperature: 120°C; Upper platen temperature: 120°C; Ramping rate: 5°C/min
5	Bonding Duration	14 hours
6	Cooling after Bonding	Ramping down to room temperature in the chamber.

The bonded wafer was observed under the microscope and the top view pictures of the wafer were shown in Figure 4.1. From the figures, it is seen that the edge of the channel has deformed indicating that CYTOP was softened and melted during bonding which is believed to be caused by the higher bonding temperature above T_g and higher bonding pressure. The wafer was diced in the dicing machine along the cross section of the channels to demonstrate the workability of the bonded channels. The wafer did not break or separate during the dicing procedure which means the strength of bonded CYTOP is sufficiently large to sustain the wafer pair. After the wafer was diced, a small volume of IPA was injected in the cross section the chip, which involves cross section of the channels, to

inspect the IPA flow condition. Figure 4.2 shows the static condition picture of IPA flow. It is found that IPA flowed inside the channel only and there were no IPA leakages into bonded CYTOP. This indicates that the channel is sealed and there is no bonding break between silicon wafer and glass wafer. Figure 4.3 shows the SEM image of the cross section of one channel. From the diagram, a clear channel opening can be found. The deformation of the channel can also be seen since the bonded CYTOP thickness is about $10\mu\text{m}$ less than the total thickness of the CYTOP coated on both wafers, which is $8\mu\text{m}$, $3.5\mu\text{m}$, respectively. However, the cross section surface is rough and this is likely caused by a rough dicing saw during the dicing procedure.



(a)



(b)

Figure 4.1 Microscope images of top view of bonded wafer

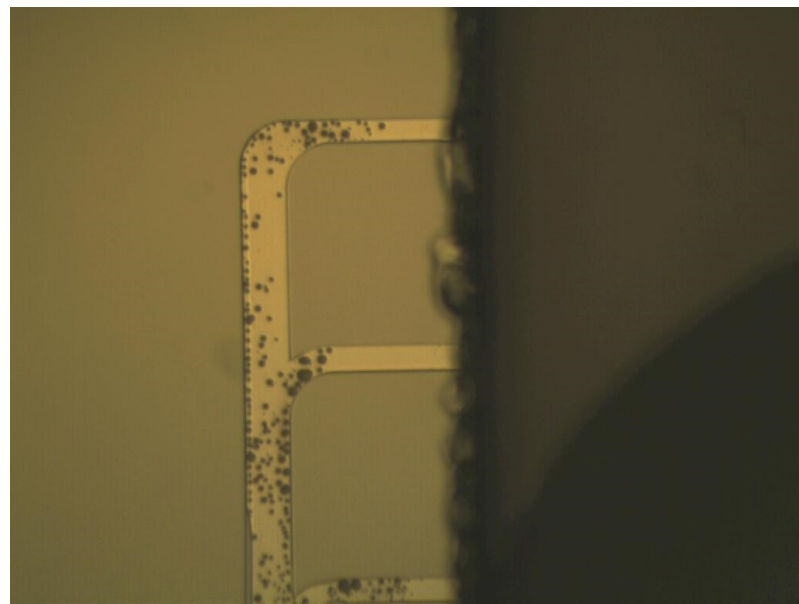


Figure 4.2 Microscope image of IPA flowing inside the channel without leakage

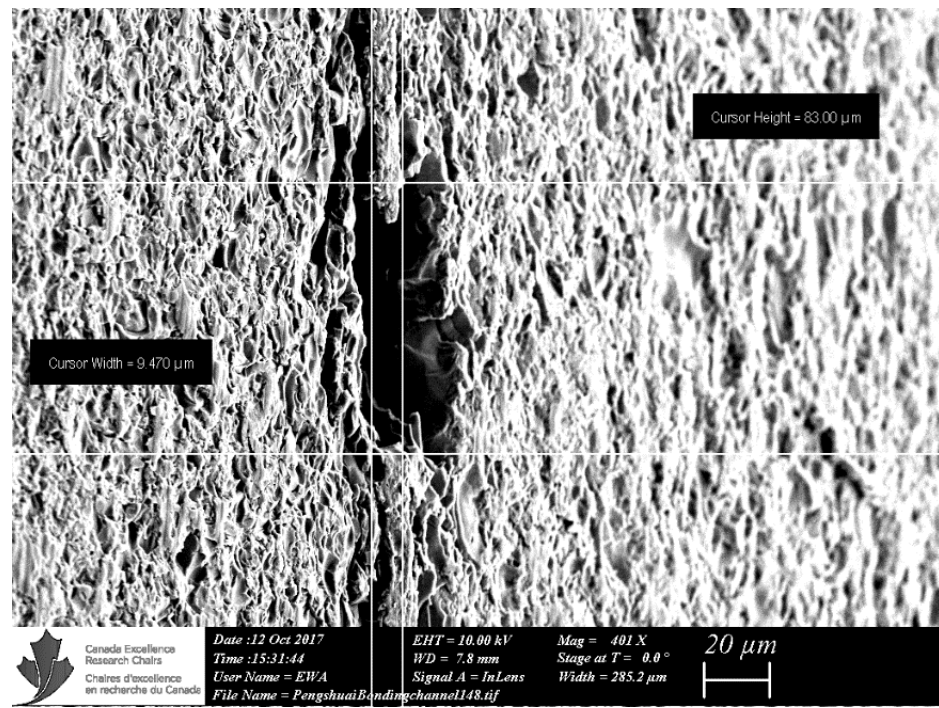


Figure 4.3 SEM image of the cross section of a channel opening

It shows the dimension of the channel with 83μm in width and ~10μm in total thickness

4.2 Bonding trial 2

The second bonding trial is bonding an unpatterned glass wafer to a patterned silicon wafer. The silicon substrate was coated with 3 layers of CYTOP A-grade by the steps given in the section 3.2. These layers of CYTOP were baked at 200°C to ensure the solvent can be fully evaporated. Next the silicon wafer was patterned with the fluidic channel mask by RIE etching protected by Al mask. The glass wafer was coated with 1 layer of CYTOP A-grade without any patterning on it. The steps were consistent with the first bonding trial except that the pressure was set to 1.5kN lower. This was done to reduce the CYTOP deformation effect that was brought by higher pressure during the bonding procedure and the lower platen temperature was set to 100°C in order to eliminate the fact that the Au waveguides could deform at a higher temperature above T_g. The step details are listed in Table XI. The bonded wafer was next diced in the dicing machine along the cross section of the channels and was polished after being dicing without any break and separation. After the wafer was diced and polished, a small volume of IPA was injected in the cross section the chip, which involves cross section of the channels, to inspect the IPA flow condition. Figure 4.4 shows the static condition picture of IPA flow. It is found that IPA flowed inside the channel only and there were no IPA leakages into bonded CYTOP. This indicates that the channel is sealed and there is no bonding break between silicon wafer and glass wafer.

Table XI The Bonding Process of the Second Trial

Step	Description	Details
1	Chamber Purging	This is automatically maneuvered by machine to clean the chamber of the machine.
2	Chamber vacuum	The chamber is vacuumed to 10^{-5} mbar before bonding.
3	Force application	1.5kN is applied manually; Pressure: 0.19MPa.
4	Controlled Heat Addition	Lower platen temperature: 100°C; Upper platen temperature: 120°C; Ramping rate: 5°C/min
5	Bonding Duration	2 hours
6	Cooling after Bonding	Ramping down to room temperature in the chamber.

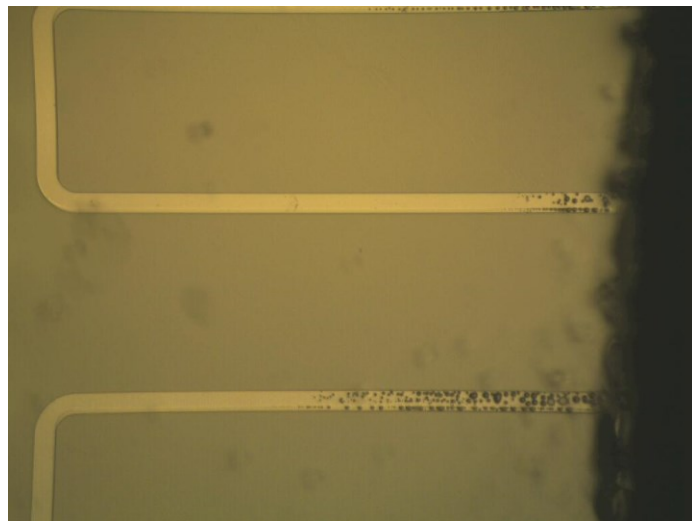


Figure 4.4 Microscope image of IPA flowing inside the channel without leakage

4.3 Bonding trial 3

The third bonding trial is align-bonding a patterned glass wafer to a silicon wafer with the same patterned feature. The silicon substrate was coated with 3 layers of CYTOP A-grade by the steps given in the section 3.2. These layers of CYTOP were baked at 200°C to ensure the solvent can be fully evaporated. Next the silicon wafer was patterned with the fluidic channel mask by RIE etching protected by Al mask. The glass wafer was coated with 3 layer of CYTOP A-grade, patterned by the same method as silicon wafer in the mirrored channel mask that matches the channels on the silicon wafer. The steps were consistent with the second bonding trial except that the upper platen temperature was set to 110°C to see if the bonding works at a lower temperature in order to minimize the high temperature issue occurring on lower platen which could lead to Au waveguides deformation. The step details are listed in Table XII.

Table XII The Bonding Process of the Third Trail

Step	Description	Details
1	Chamber Purging	This is automatically maneuvered by machine to clean the chamber of the machine.
2	Chamber vacuum	The chamber is vacuumed to 10^{-5} mbar before bonding.
3	Wafer Alignment	The trade off accuracy of alignment is $\sim 10\mu\text{m}$.
4	Force application	1.5kN is applied manually; Pressure: 0.19MPa.
5	Controlled Heat Addition	Lower platen temperature: 100°C; Upper platen temperature: 110°C; Ramping rate: 5°C/min
6	Bonding Duration	14 hours
7	Cooling after Bonding	Ramping down to room temperature in the chamber.

The bonded wafer was inspected under the microscope after the bonding process was finished. Figure 4.5 shows the microscope image of the top view of bonded wafer. From the image, it was seen that there is misalignment of the channel between the silicon substrate and glass lid. The color along the channel feature indicates that two wafers are not bonded and channels are not sealed. The misalignment dimension is approximately $20\mu\text{m}$ observed from Figure 4.6. Since this pair was not successfully bonded, no further dicing procedure pursued.

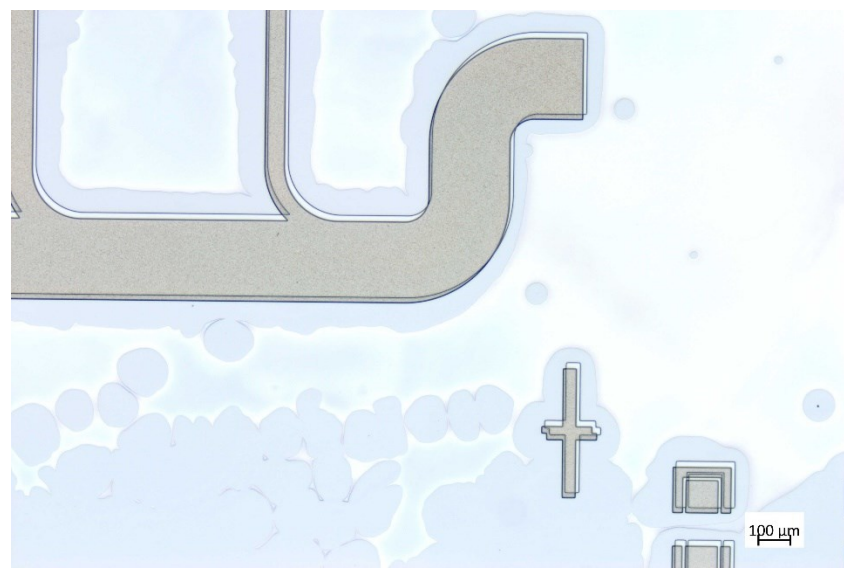


Figure 4.5 Microscope images of top view of the third bonded wafer

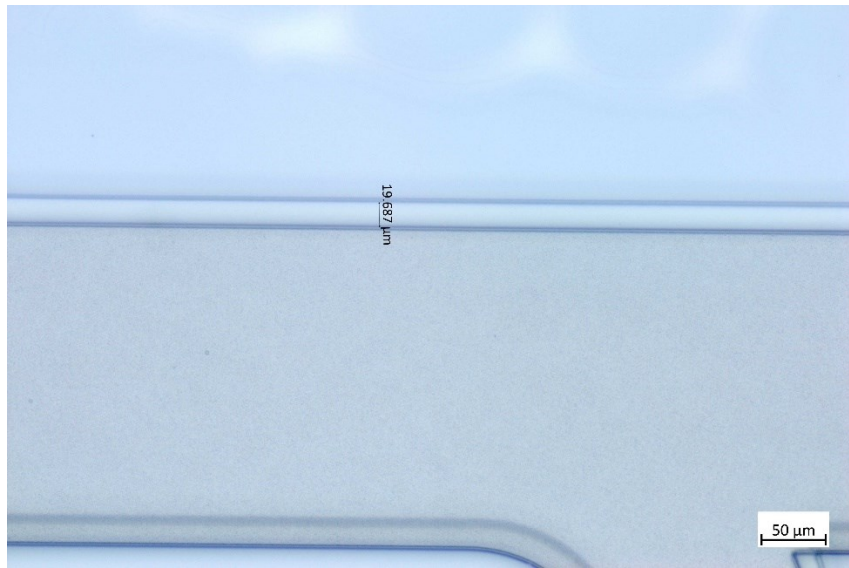


Figure 4.6 Misalignment indication by microscope of the third wafer pair

4.4 Bonding trail 4

The fourth bonding trial is align-bonding a patterned glass wafer to a silicon wafer with the same patterned feature. The silicon substrate was coated with 3 layers of CYTOP A-grade by the steps cited in section 3.2. These layers of CYTOP were baked at 200°C to ensure the solvent can be fully evaporated. The silicon wafer was next patterned with the fluidic channel mask by RIE etching protected by Al mask. The glass wafer was coated with 3 layers of CYTOP A-grade, patterned by the same method as silicon wafer in the mirrored channel mask that matches the channels on the silicon wafer. The steps were identical to those of the second bonding trial. The step details are listed in Table XIII.

The bonded wafer was inspected under the microscope after the bonding process was finished. Figure 4.7 shows the microscope image of the top view of bonded wafer. From the image, it was seen that there are misalignment of the channel between the silicon substrate and glass lid. However, the bonding is successfully achieved with no color indicating the channel is sealed by the bonding procedure at 120°C. One assumption causing the misalignment issue is that the force applied on the wafer is a slightly higher. As the bonding temperature of the glass lid is 120°C above T_g , the CYTOP on the glass lid would deform under a certain amount of pressure, leading to a movement of the glass lid during bonding. Although the silicon wafer maintain the temperature below T_g , the thermal transfer from glass lid to the CYTOP on silicon would increase its temperature, potentially beyond T_g , which could deteriorate the misalignment. The following trails would be focused on lowering the pressure of the bonding wafers to determine if this can improve the misalignment issue. Next, the wafer was diced in the dicing machine without any break

or separation, which means the bonding process of this trial works. A small volume of IPA was dropped on the edge of the dicing section to observe if channels were sealed properly.

Figure 4.8 shows the IPA was flowing inside the channels without any leakage, demonstrating that the channels were sealed.

Table XIII The Bonding Process of the Fourth Trial

Step	Description	Details
1	Chamber Purging	This is automatically maneuvered by machine to clean the chamber of the machine.
2	Chamber vacuum	The chamber is vacuumed to 10^{-5} mbar before bonding.
3	Wafer Alignment	The trade off accuracy of alignment is $\sim 10\mu\text{m}$.
4	Force application	1.5kN is applied manually; Pressure: 0.19MPa.
5	Controlled Heat Addition	Lower platen temperature: 100°C; Upper platen temperature: 120°C; Ramping rate: 5°C/min
6	Bonding Duration	14 hours
7	Cooling after Bonding	Ramping down to room temperature in the chamber.

In this chapter, four bonding trials were tested. Among those trials, CYTOP A-grade to CYTOP A-grade bonding were conducted under various temperature and pressure conditions. A successful CYTOP A-grade bonding was achieved in the condition that the bonding temperature is 120°C at least on the glass wafer and the bonding pressure is approximately 0.19MPa. A bonding failure was found when the bonding temperature is 110°C on the glass wafer, indicating that achieving a certain level of temperature is important in a successful bonding process. Channel deformation was found on those four trials due to the potentially higher pressure. The bonding results with the better view achieved among those trials was the one with bonding temperature at 120°C applied on both silicon and glass wafer. The potential damage to the waveguides that bonded at temperature above T_g still remains unknown and heating both wafers with waveguides to 120°C is worth trying to test if these waveguides can survive at this level of the temperature. In the next experiment, process trials with lower pressure needs to be pursued to maintain the channel profile completely and bonding trials with waveguides at higher temperature should be tested as well to achieve more accurate bonding results. It is worth noting that another bonding option that requires all channels to be patterned only on the glass wafer will be considered. In this bonding method, the glass lid with patterned channels will bond to silicon wafer with only waveguides and lower cladding CYTOP. Since no upper cladding will be applied and patterned on the silicon wafer, there is no requirement for alignment before wafer bonding.



Figure 4.7 Microscope images of top view of the forth wafer pair



Figure 4.8 Microscope image of IPA flowing inside the channel without leakage

5 Chapter: Conclusions and Future Work

This thesis continues to pursue accomplishing an integrated LRSPP waveguide biosensor based on the previous work [40] [41] [42] [43] [44]. The contributions made in this thesis include channel etching modification for the accurate thickness of Au waveguides by introducing SiO₂ etch stop layer process. Additionally, this thesis explored the elimination of the cracking issue resulting from SPR-220 baking procedure by patterning Al as an etching mask to replace SPR-220. This thesis also pursued a feasible bonding process to encapsulate the fluidic channels required to reduce bubbles and to detect the analyte in an isolated testing environment. Lastly, a CYTOP A-grade was applied as a substitution of M-grade and S-grade used in the previous work to improve the adhesion between Au and CYTOP.

The physical and optical measurement of the devices fabricated following the process described in the thesis were evaluated with some improvement but remaining issues need to be solved. The thickness of Au waveguides is uniformly accurate around the entire wafer and roughness of Au waveguides in the channel is much smaller due to the presence of etch stop layer. The cracking issue caused by thermal treatment of SPR-220 vanished because of introducing Al as a hard channel mask that can be thermally compatible with CYTOP during the process. The application of Al leads to no cracking appearing in the post channel etching mask patterning process. The remaining issue in the Al mask process is that the naturally opaque characteristic of Al makes the underneath pattern almost invisible. This leads to a misalignment of the channel feature with etch stop layer causing over-etching trench and side protrusion on both edges of the channels. Through the biochemical testing

measurement, a clear LRSPP mode image was captured, indicating the successful excitation of LRSPP can be achieved through the fabricated device. The BSA testing and bulk protein testing were conducted under the application of the device. The results show the function of the device is achievable and repeatable. The remaining issue is the noise background involving the testing output making it less stable which may be for multiple reasons. One reason might be caused by the SiO₂ residue remaining beneath the side protrusion of the channels as a result of misalignment between channel and SiO₂ etch stop layer. The physical measurement and IPA test were successfully accomplished on the bonded wafer pairs, which means the fluidic channels were sealed by the current bonding process. The optical performance shows a 5.03dB/mm attenuation loss in the Au straight waveguide and a 0.10dB response of a monolayer of BSA protein on the Au straight waveguide. These results indicate the chips that were fabricated by the process present in the thesis are able to work as a biosensor.

Future efforts should focus on the improvement of Al channel mask process to eliminate the misalignment issue. One possible solution is to use lift-off process to pattern the Al mask instead of wet etching process. The advantage of the lift-off process is that the bi-layer stack is transparent, making the precise alignment between channels and etch stop layer feasible. A more detailed step needs to be explored. Another focus is on the improvement of a bonding process which would achieve bonding successfully at a relative lower temperature and pressure, thereby allowing sealing without any deformation of fluidic channels.

References

- [1] O. Krupin, W. R. Wong, F. R. M. Adikan and a. P. Berini., "Detection of Small Molecules Using Long-Range Surface Plasmon Polariton Waveguides," *IEEE Journal of Selected Topics in Quantum Electronics*, vol. 23, no. 2, pp. 1-10, 2017.
- [2] J. C. Cooper and E. A. H. Hall., "The nature of biosensor technology," *Journal of biomedical engineering*, vol. 10, no. 3, pp. 210-219, 1988.
- [3] O. Krupin, W. R. Wong, P. Béland, F. R. M. Adikan and a. P. Berini., "Long-range surface plasmon-polariton waveguide biosensors for disease detection.," *Journal of lightwave technology*, vol. 34, no. 20, pp. 4673-4681, 2016.
- [4] G. G. Nenninger, P. Tobiška, J. Homola and S. S. & Yee, "Long-range surface plasmons for high-resolution surface plasmon resonance sensors.," *Sensors and Actuators B: Chemical*, vol. 74, no. 1, pp. 145-151, 2001.
- [5] A. Lioumpas, G. Ntouni and a. K. S. Nikita., "Sensing Principles for Biomedical Telemetry," in *Handbook of Biomedical Telemetry*, 2014, pp. 56-75.
- [6] M. N. Velasco-Garcia, "Optical biosensors for probing at the cellular level: a review of recent progress and future prospects.," *Seminars in cell & developmental biology.*, vol. 20, no. 1, pp. 27-33, 2009.
- [7] A. P. Leung, M. Shankar and a. R. Mutharasan., "A review of fiber-optic biosensors," *Sensors and Actuators B: Chemical*, vol. 125, no. 2, pp. 688-703, 2007.
- [8] K. R. Rogers, "Recent advances in biosensor techniques for environmental

- monitoring," *Analytica Chimica Acta*, vol. 568, no. 1, pp. 222-231, 2006.
- [9] B. Sepulveda, J. S. D. Rio, M. Moreno, F. J. Blanco, K. Mayor, C. Domínguez and a. L. M. Lechuga., "Optical biosensor microsystems based on the integration of highly sensitive Mach–Zehnder interferometer devices., " *Journal of Optics A: Pure and Applied Optics*, vol. 8, no. 7, p. S561, 2006.
- [10] M. T. Vo-Dinh and a. Brian, "Fluorescence Spectroscopy for Biomedical Diagnostics," in *Biomedical Photonics Handbook*, CRC Press, 2003, pp. 485-542.
- [11] V. Passaro, F. Dell'Olio, B. Casamassima and F. & De Leonardis, "Guided-wave optical biosensors., " *Sensors*, vol. 7, no. 4, pp. 508-536, 2007.
- [12] V. D. Jangampet, R. Dixit, D. Klotzkin and I. Papautsky, "Simultaneous, Single-Detector Fluorescence Detection of Multiple Fluorescent Dyes," in *SENSORS, 2010 IEEE*, 2010.
- [13] G. Gauglitz, "Direct optical sensors: principles and selected applications., " *Analytical and bioanalytical chemistry*, vol. 381, no. 1, pp. 141-155, 2005.
- [14] W. E. Moerner and a. D. P. Fromm., "Methods of single-molecule fluorescence spectroscopy and microscopy," *Review of Scientific instruments*, vol. 74, no. 8, pp. 3597-3619, 2003.
- [15] X. Fan, I. M. White, S. I. Shopova, H. Zhu, J. D. Suter and Y. & Sun, "Sensitive optical biosensors for unlabeled targets: A review., " *analytica chimica acta*, vol. 620, no. 1, pp. 8-26, 2008.
- [16] F. B. Prieto, A. Sepulveda, A. L. Calle, Carlos Domínguez, Antonio Abad, A. Montoya and a. L. M. Lechuga., "An integrated optical interferometric nanodevice

based on silicon technology for biosensor applications., " *Nanotechnology*, vol. 14, no. 8, p. 907, 2003.

- [17] K. O. Hill, Y. Fujii, D. C. Johnson and B. S. & Kawasaki, "Photosensitivity in optical fiber waveguides: Application to reflection filter fabrication., " *Applied physics letters*, vol. 32, no. 10, pp. 647-649, 1978.
- [18] R. Horváth, H. C. Pedersen, N. Skivesen, D. Selmeczi and N. B. & Larsen, "Optical waveguide sensor for on-line monitoring of bacteria., " *Optics letters*, vol. 28, no. 14, pp. 1233-1235, 2003.
- [19] H. Lu, Z. Cao, H. Li and Q. & Shen, "Study of ultrahigh-order modes in a symmetrical metal-cladding optical waveguide., " *Applied physics letters*, vol. 85, no. 20, pp. 4579-4581, 2004.
- [20] R. Wood, "On a remarkable case of uneven distribution of light in a diffraction grating spectrum," *Philosophical Magazine*, vol. 4, pp. 396-402, 1902.
- [21] Kretschmann, Erwin and a. H. Raether., "Radiative decay of non radiative surface plasmons excited by light., " *Zeitschrift für Naturforschung A*, vol. 23, no. 12, pp. 2135-1236, 1968.
- [22] A. Otto, "Excitation of nonradiative surface plasma waves in silver by the method of frustrated total reflection., " *Zeitschrift für Physik*, vol. 216, no. 4, pp. 398-410, 1968.
- [23] W. L. Barnes, A. Dereux and T. W. Ebbesen, "Surface plasmon subwavelength optics., " *nature*, vol. 424, no. 6950, p. p.824, 2003.
- [24] S. A. Maier, "Chpater 2: Surface plasmon polaritons at metal/insulator interfaces,"

- in *Plasmonics: Fundamentals and Applications*, Springer, 2007, pp. 21-37.
- [25] J. Homola, "Present and future of surface plasmon resonance biosensors.," *Analytical and bioanalytical chemistry*, vol. 377, no. 3, pp. 528-539, 2003.
- [26] J. Homola, S. S. Yee and a. G. Gauglitz., "Surface plasmon resonance sensors: review," *Sensors and Actuators B: Chemical*, vol. 54, no. 1, pp. 3-15, 1999.
- [27] J. Homola, "Surface plasmon resonance sensors for detection of chemical and biological species.," *Chemical reviews*, vol. 108, no. 2, pp. 462-493, 2008.
- [28] X. D. Hoa, A. G. Kirk and a. M. Tabrizian., "Towards integrated and sensitive surface plasmon resonance biosensors: a review of recent progress.," *Biosensors and Bioelectronics*, vol. 23, no. 2, pp. 151-160, 2007.
- [29] P. I. Nikitin, A. A. Beloglazov, V. E. Kochergin, M. V. Valeiko and T. I. & Ksenevich, "Surface plasmon resonance interferometry for biological and chemical sensing.," *Sensors and Actuators B: Chemical*, vol. 54, no. 1, pp. 43-50, 1999.
- [30] D. Sarid, "Long-range surface-plasma waves on very thin metal films," *Physical Review Letters*, vol. 47, no. 26, p. 1927, 1981.
- [31] J. C. Quail, J. G. Rako and a. H. J. Simon., "Long-range surface-plasmon modes in silver and aluminum films.," *Optics letters*, vol. 8, no. 7, pp. 377-379, 1983.
- [32] Dostálek, Jakub, A. Kasry and W. Knoll., "Long range surface plasmons for observation of biomolecular binding events at metallic surfaces.," *Plasmonics*, vol. 2, no. 3, pp. 97-106, 2007.
- [33] P. Berini, "Long-range surface plasmon polaritons.," *Advances in optics and photonics*, vol. 1, no. 3, pp. 484-588, 2009.

- [34] A. W. Wark, H. J. Lee and a. R. M. Corn., "Long-range surface plasmon resonance imaging for bioaffinity sensors., " *Analytical Chemistry*, vol. 77, no. 13, pp. 3904-3907, 2005.
- [35] P. Berini, "Plasmon-polariton waves guided by thin lossy metal films of finite width: Bound modes of symmetric structures., " *Physical Review B*, vol. 61, no. 15, p. 10484, 2000.
- [36] R. Charbonneau, P. Berini, E. Berolo and E. Lisicka-Skrzak, "Experimental observation of plasmon-polariton waves supported by a thin metal film of finite width., " *Optics letters*, vol. 25, no. 11, pp. 844-846, 2000.
- [37] P. Berini, R. Charbonneau, N. Lahoud and G. & Mattiussi, "Characterization of long-range surface-plasmon-polariton waveguides., " *Journal of Applied Physics*, vol. 98, no. 4, p. 043109, 2005.
- [38] T. Nikolajsen, K. Leosson and a. S. I. Bozhevolnyi., "In-line extinction modulator based on long-range surface plasmon polaritons., " *Optics Communications*, vol. 244, no. 1, pp. 455-459, 2005.
- [39] R. Daviau, E. Lisicka-Skrzak, R. N. Tait and P. Berini, "Broadside excitation of surface plasmon waveguides on Cytop., " *Applied Physics Letters*, vol. 94, no. 9, p. 091114, 2009.
- [40] R. Daviau, "Fabrication of surface plasmon waveguides on Cytop., " *Diss. University of Ottawa (Canada)*, 2009.
- [41] C. Chiu, "Fabrication of surface plasmon waveguide devices in CYTOP with microfluidic channels., " *Diss. University of Ottawa (Canada)*, 2010.

- [42] H. Asiri, "Fabrication of surface plasmon biosensors in cytop.," *Diss. University of Ottawa (Canada)*, 2012.
- [43] S. Hassan, "Microfabrication of Plasmonic Device: PPBG Biosensor in Cytop, Reflection Itensity Modulator and Atomically Flat Nanohole Array.," *Diss. Université d'Ottawa/University of Ottawa*, 2015.
- [44] H. J. Northfield, "Fabrication of Long Range Surface Plasmon Polariton Bragg Waveguide Biosensors on Cytop and Multilayer Substrates.,," *Diss. Carleton University*, 2015.
- [45] K. Leosson and a. B. Agnarsson., "Integrated biophotonics with CYTOP.," *Micromachines*, vol. 3, no. 1, pp. 114-125, 2012.
- [46] AGC., "CYTOP Catalog - Bellex International Corporation," 2017. [Online].
- [47] AGC., "CYTOP: Curing Conditions," [Online].
- [48] MicroChem, "S1800 Series - MicroChem," [Online].
- [49] MicroChem, "LOR and PMGI Resists - MicroChem," [Online].
- [50] C. ÖZGEN, "GROWTH OF GOLD FILMS ON QUARTZ SURFACES FOR QUARTZ CRYSTAL MICROBALANCE APPLICATION.," *Diss. MIDDLE EAST TECHNICAL UNIVERSITY*, 2010.
- [51] H. Fan, "Passive and Thermo-Optic Characterization of Long-Range Surface Plasmon-Polariton Structures in CYTOP," *Thesis University of Ottawa*, 2011.
- [52] H. Fan, "Thermo-Optic and Refractometric Performance of Long-Range Surface Plasmon Multiple-Output Mach-Zehnder Interferometers," *Diss. Université d'Ottawa/University of Ottawa*, 2016.

- [53] V. Patil and C. B. O'Neal., "Adhesive Strength Characterization of CYTOP™: Low Temperature Wafer-Level Packaging.,," in *American Society of Mechanical Engineers*, 2006.
- [54] K. Ren, W. Dai, J. Zhou, J. Su and H. Wu, "Whole-Teflon microfluidic chips.,," *Proceedings of the National Academy of Sciences*, vol. 108, no. 20, pp. 8162-8166, 2011.
- [55] C.-W. Tsao and D. L. DeVoe, "Bonding of thermoplastic polymer microfluidics.,," *Microfluidics and Nanofluidics*, vol. 6, no. 1, pp. 1-16, 2009.
- [56] J. S. Varsanik and J. J. Bernstein., "Voltage-assisted polymer wafer bonding.,," *Journal of Micromechanics and Microengineering*, vol. 22, no. 2, p. 025004, 2012.
- [57] K. W. Oh, A. Han, S. Bhansali and C. H., "A low-temperature bonding technique using spin-on fluorocarbon polymers to assemble microsystems.,," *Journal of Micromechanics and Microengineering*, vol. 12, no. 2, p. 187, 2002.